



## 저작자표시-비영리-변경금지 2.0 대한민국

이용자는 아래의 조건을 따르는 경우에 한하여 자유롭게

- 이 저작물을 복제, 배포, 전송, 전시, 공연 및 방송할 수 있습니다.

다음과 같은 조건을 따라야 합니다:



저작자표시. 귀하는 원저작자를 표시하여야 합니다.



비영리. 귀하는 이 저작물을 영리 목적으로 이용할 수 없습니다.



변경금지. 귀하는 이 저작물을 개작, 변형 또는 가공할 수 없습니다.

- 귀하는, 이 저작물의 재이용이나 배포의 경우, 이 저작물에 적용된 이용허락조건을 명확하게 나타내어야 합니다.
- 저작권자로부터 별도의 허가를 받으면 이러한 조건들은 적용되지 않습니다.

저작권법에 따른 이용자의 권리는 위의 내용에 의하여 영향을 받지 않습니다.

이것은 [이용허락규약\(Legal Code\)](#)을 이해하기 쉽게 요약한 것입니다.

[Disclaimer](#)

이학박사 학위논문

**Interfacial Engineering on the  
Lattice and Electronic Structure of  
Perovskite Oxide Thin Films**

페로브스카이트 산화물 박막의 격자 및  
전자 구조에 대한 계면 제어

2021 년 2 월

서울대학교 대학원

물리천문학부

이 한 결

# **Interfacial Engineering on the Lattice and Electronic Structure of Perovskite Oxide Thin Films**

Han Gyeol Lee

Supervised by

Professor Tae Won Noh

A Dissertation Submitted to the Faculty of Seoul National  
University in Partial Fulfillment of the Requirements for the  
Degree of Doctor of Philosophy

February 2021

*Department of Physics and Astronomy*

*Graduate School*

*Seoul National University*

**Interfacial Engineering on the Lattice and Electronic  
Structure of Perovskite Oxide Thin Films**

페로브스카이트 산화물 박막의  
격자 및 전자 구조에 대한 계면 제어

지도교수 노 태 원


이 논문을 이학박사학위논문으로 제출함  
2020 년 12 월

서울대학교 대학원  
물리·천문학부  
이 한 결

이한결의 박사학위논문을 인준함  
2020 년 12 월

위 원 장 \_\_\_\_\_ 차 국 린 (인) 

부 위 원 장 \_\_\_\_\_ 노 태 원 (인) 

위 원 \_\_\_\_\_ 김 창 영 (인) 

위 원 \_\_\_\_\_ 양 범 정 (인) 

위 원 \_\_\_\_\_ 장 서 형 (인) 

---

# Contents

<b>List of Figures</b>	3
<b>Abstract</b>	10
<b>Chapter 1. Introduction</b>	12
1.1 Perovskite oxides	
1.2 Interfacial engineering of ultra-thin films	
1.3 Outline of Thesis	
<b>Chapter 2. Experimental Methods</b>	17
2.1 Pulsed laser deposition	
2.2 Structure and surface characterization	
2.3 Transport measurement	
2.4 Spectroscopic measurement	
<b>Chapter 3. Results and Discussion I: Buffer Layer</b>	22
3.1 Introduction: BaBiO <sub>3</sub>	
3.2 Bilayer buffer template	
3.3 Anisotropic suppression of breathing distortion	
3.4 Conclusion	

<b>Chapter 4. Results and Discussion II: Surface</b>	<b>34</b>
4.1 Introduction: SrRuO <sub>3</sub>	
4.1.1 Physical properties of SrRuO <sub>3</sub>	
4.1.2 Surface termination engineering of SrRuO <sub>3</sub> thin film	
4.2 Water-leaching technique and surface termination conversion	
4.3 Surface metal-insulator transition	
4.4 Conclusion	
<b>Chapter 5. Results and Discussion III: Capping Layer</b>	<b>48</b>
5.1 Introduction: Anomalous Hall effect of SrRuO <sub>3</sub>	
5.1.1 ‘Intrinsic’ anomalous Hall effect	
5.1.2 Origin of anomalous Hall effect in SrRuO <sub>3</sub>	
5.1.3 Recent controversies related to topological Hall effect	
5.2 Tunable inhomogeneity induced by the capping layer	
5.3 Conclusion	
<b>Chapter 6. Summary and Concluding Remarks</b>	<b>63</b>
<b>Bibliography</b>	<b>65</b>
<b>Appendix</b>	<b>78</b>
<b>Curriculum Vitae &amp; List of Publication</b>	<b>94</b>
<b>국문 초록 (Korean Abstract)</b>	<b>97</b>
<b>감사의 글 (Acknowledgements)</b>	<b>99</b>

---

# List of Figures

**Fig. 1-1** Schematic diagram of octahedral crystal field splitting of perovskite oxides.

**Fig. 1-2** **a.** Schematic illustration of the octahedral symmetry propagation. The cubic symmetry of the substrate propagates into the film material suppressing the octahedral rotation. Adapted from J. M. Rondinelli *et al* (2012). **b.** Schematics of epitaxial strain engineering. The film is under the in-plane biaxial compressive (tensile) strain from the substrate with the smaller (larger) lattice constant. Adapted from D. G. Schlom *et al* (2014).

**Fig. 2-1** Schematic illustration of the pulsed laser deposition technique.

**Fig. 3-1** **a.** Schematic illustration of oxygen octahedral breathing distortion. **b.** Schematic density of state (DOS) diagram of BaBiO<sub>3</sub> due to breathing distortion. The 2 eV gap opening occurs at the Fermi level ( $E_F$ ).

**Fig. 3-2** X-ray diffraction (XRD) rocking curve for (002) diffraction of BaCeO<sub>3</sub> (BCO) layers on **a.** the SrTiO<sub>3</sub> (STO) substrate and **d.** the BaZrO<sub>3</sub> (BZO)-arbitrating layer. Red and blue dashed lines are a Gaussian component and background component of raw data. Arrows indicate full-width at half maximum values of fitting curves. The pseudo-cubic notation was used for indexing all reflections. Atomic force microscopy (AFM) topographic images of the BCO layers on **b.** the STO substrate and **e.** the BZO arbitrating layer. A line profile along the white line in **b** (**e**) was plotted in **c** (**f**). Adapted from H. G. Lee *et al* (2016).

**Fig. 3-3** **a.** High-resolution transmission electron microscopy (HRTEM) image of the double-layer buffer structure on the STO substrate. **b.** and **c.** Fourier-filtered images of the red squares in **a**, using the (100) location. The white circles indicate the positions of misfit dislocations, and the white lines indicate the interfaces between layers. Adapted from H. G. Lee *et al* (2016).

**Fig. 3-4** Schematic sample structures of **a.** BBO/STO, **d.** BBO/BCO/STO, and **g.** BBO/BCO/BZO/STO. **b.**, **e.**, and **h.** Reciprocal space maps (RSMs) around STO (103) diffraction measured from **a**, **d**, and **g**, respectively. The black lines are cubic relaxation lines from STO (103). **c.**, **f.**, and **i.** XRD rocking curves at BBO (002) diffraction from **a**, **d**, and **g**, respectively. Red and blue dashed lines are a Gaussian component and background component of raw data. Arrows indicate full-width at half maximum values of rocking curves. The pseudo-cubic notation was used for indexing all reflections. Adapted from H. G. Lee *et al* (2016).

**Fig. 3-5** **a.** Raman responses of fully strained BBO with the variation of film thickness when the sample is exposed to 633-nm laser irradiation. The first and second harmonics at  $565\text{ cm}^{-1}$  and  $1,130\text{ cm}^{-1}$  are excited due to the oxygen octahedral breathing phonon modes of BBO. **b.** Optical conductivity spectra of BBO films with variation in film thickness. The absorption maximum at 2.05 eV comes from direct optical transitions across the charge-density-wave gap in BBO. **c.** Summary of the evolution of Raman intensity values at  $565\text{ cm}^{-1}$  and optical conductivity values at 2.05 eV as a function of BBO film thickness. Both values show discontinuity near 6–8 u.c. as highlighted in red. Solid lines are guides for the eye. Adapted from H. G. Lee *et al* (2018).



- Fig. 3-6** **a.** Calculated oxygen displacement in each unit cell of BBO with different lattice planes. The BCO sublayer is in the yellow background. At the BBO/BCO interface (gray-colored) and the BBO surface (blue-colored), the oxygen up-down mode in BaO slabs is broken while the change in the oxygen expanding-shrinking mode in BiO<sub>2</sub> slabs is negligible. **b.** The oxygen displacement deviation from the ideal breathing mode. The value 0 represents the ideal breathing pattern. **c.** The schematics of 10-u.c.-thick BBO on BCO sublayer. The octahedral structure of BBO with distinct three regions was displayed with an exaggerated scale. Adapted from H. G. Lee *et al* (2018).
- Fig. 4-1** Schematics of termination engineering. **a.** At AO-terminated film, BO<sub>6</sub> octahedral crystal field split the *B* 4*d* band into *t*<sub>2g</sub> and *e*<sub>g</sub> subbands. The partially-filled *t*<sub>2g</sub> band results in finite density-of-states (DOS) near the Fermi level (*E*<sub>F</sub>), signifying robust metallicity. **b.** At the BO<sub>2</sub>-terminated film surface, on the contrary, the loss of apex oxygen breaks the BO<sub>6</sub> octahedral symmetry. It further splits the *t*<sub>2g</sub> and *e*<sub>g</sub> bands. Adapted from H. G. Lee *et al* (2020).
- Fig. 4-2** SRO surface termination conversion triggered by water-leaching. **a-j.** Atomic force microscopy topographic height images (**a-e**), and corresponding phase images (**f-j**) of the SRO thin film acquired after different water-leaching durations (*t*<sub>w</sub>). All the scale bars correspond to 300 nm. **k.** Schematics of surface termination evolution during water-leaching. The topmost SrO layer is gradually dissolved during water leaching. **i.** Coaxial impact-collision ion scattering spectroscopy measurements on the as-grown (blue) and water-leached (red) SRO(001) surfaces. The experimental spectra (dotted lines) can be well fitted (solid lines) via two Gaussian peaks. Adapted from H. G. Lee *et al* (2020).

**Fig. 4-3** Electrical transport and magnetic characterizations of SRO ultrathin films. **a-h.** Temperature-dependent longitudinal resistivity (**a-d**) and magnetization (**e-h**) ( $\rho_{xx}$ - $T$  and  $M$ - $T$ ) curves of the SrO- (blue curves) and RuO<sub>2</sub>- (red curves) terminated SRO films with various  $N_{\text{Ru}}$ . The  $M$ - $T$  curves are measured with an out-of-plane magnetic field ( $H$ ) of 100 Oe. **i-l.**  $H$ -dependent anomalous Hall resistivity ( $\rho_{\text{AHE}} - H$ ) curves measured at 10 K from the SrO- and RuO<sub>2</sub>-terminated SRO films with various  $N_{\text{Ru}}$ . All of the ordinary Hall components have been subtracted for clarity. The  $H$  scanning directions are indicated by solid arrows. Adapted from H. G. Lee *et al* (2020).

**Fig. 4-4** Evolution of electrical transport and magnetic properties with  $t_{\text{SRO}}$  and surface termination. **a-d.**  $t_{\text{SRO}}$ -dependent sheet resistivity ( $\rho_{\text{sheet}}$ ) (**a**), sheet carrier density ( $n_{\text{sheet}}$ ) (**b**), magnetization (**c**), and Curie temperature ( $T_{\text{C}}$ ) (**d**) of the SRO thin films. The  $\rho_{\text{sheet}}$ ,  $n_{\text{sheet}}$ , and  $M$  values were measured at 10 K. All curves exhibit a step-like feature, signifying that the metallicity and magnetism of RuO<sub>2</sub>- terminated samples consisting of  $N_{\text{Ru}}$  RuO<sub>2</sub> layers are similar to those of SrO-terminated samples consisting of  $N_{\text{Ru}}-1$  RuO<sub>2</sub> layers. **e-f.** Scanning tunneling spectroscopies of the SrO- (**e**) and RuO<sub>2</sub>- (**f**) terminated samples. The solid lines are bias-dependent differential conductance ( $dI/dV$ - $V$ ) curves averaged from 14 curves measured at flat and clean surface regions. The colored backgrounds indicate the standard deviations. The insets of **e** and **f** are schematic atomic structures of SRO films with SrO- and RuO<sub>2</sub>-terminated surfaces, respectively. The electrical conductivity of the topmost SRO monolayer with RuO<sub>2</sub>-termination decays significantly. Adapted from H. G. Lee *et al* (2020).

**Fig. 4-5** Electronic structure and 4d orbital occupancy in SRO ultrathin film. **a.** Orbital-resolved DOS projected along with the RuO<sub>2</sub> layer underneath the SrO layer. **b.** Orbital-resolved DOS projected along with the RuO<sub>2</sub>-terminated surface layer. The gap size is ~0.25 eV. Insets of **(a)** and **(b)** illustrate the low-spin and high-spin configurations in the bulk-like and surface RuO<sub>2</sub> layers, respectively. **c.** X-ray linear dichroism (XLD) at the Ru *L*<sub>2</sub> edge measured from the SrO- and RuO<sub>2</sub>-terminated SRO films (*N*<sub>Ru</sub> = 5). *I*<sub>||</sub> and *I*<sub>⊥</sub> are X-ray absorption spectroscopy intensities with linear light polarization parallel (*E*<sub>||</sub>) and perpendicular (*E*<sub>⊥</sub>) to the (001) surface. The schematic inset shows how the  $d_{x^2-y^2}^2$  (top) and  $d_{3z^2-r^2}^2$  (bottom) orbitals couple with the incident linear-polarized X-ray. The light-color (deep-color) indicates the unoccupied (occupied) orbitals. Adapted from H. G. Lee *et al* (2020).

**Fig. 5-1** **a.** Schematic band diagram of the SRO thin film. Different color of the curves denotes spin-majority and minority bands. Each circle is the band crossing points, which gives non-zero Berry curvature. **b.** Band shift from the magnetization changes. The gap between spin-majority and minority bands become larger with increasing magnetization. Positions of crossing points are also shifting. **c.** Band shift with respect to the Fermi level

**Fig. 5-2** **a.** Schematic illustration of the magnetic Skyrmion (Bloch type). Arrows denote the direction of spins. **b.** Evolution of solid angle with varying the external magnetic field. The solid angle of spin emerges at the sudden magnitude of the field with the Dzialoszynski-Moriya interaction. When the external field keeps increasing, the solid angle is suppressed due to the spin alignment.

**Fig. 5-3** **a.** The AHE curve of 5 u.c. SRO film (green) and the THE curve from the possible magnetic Skyrmion (orange). **b.** AHE curves which have an opposite sign with each other. The positive (red) AHE comes from the 4 u.c. SRO film while the negative (blue) AHE curve comes from the 5 u.c. SRO film. **c.** The resultant AHE curve with the hump structure comes from either **a** or **b**. Adapted from L. Wang *et al* (2020).

**Fig. 5-4** **a (c).** Schematic sample structure of 5-unit-cell (u.c.) SrRuO<sub>3</sub> (SRO) films grown on the SrTiO<sub>3</sub>(001) (STO) substrate without (with) 10 u.c. of LaAlO<sub>3</sub> (LAO) capping layer. **b (d).** Surface topographic images of **a (c)**, respectively, obtained by atomic force microscope. **e.** Anomalous Hall resistivity-magnetic field ( $\rho_{\text{AHE}}-H$ ) curves of 5 and 4 u.c.-SRO films without capping layer measured at 10K. All the linear terms from the ordinary Hall effect were subtracted. Arrows denote field sweep direction. **f-h.**  $\rho_{\text{AHE}}-H$  curves of LAO capped SRO films. The growth condition and thickness of SRO layers were fixed while the growth pressure of the LAO layer was varied from 5mTorr to 0.5mTorr.

**Fig. 5-5** **a.** Magnetization-temperature ( $M-T$ ) curves of 5 and 4 u.c.-SRO films without capping layer. Open circles are experimental data and solid lines are fitting curves. **b-d.**  $M-T$  curves of LAO capped SRO films. The growth condition and thickness of SRO layers were fixed while the growth pressure of the LAO layer was varied from 5mTorr to 0.5mTorr. The blue (red) fitting curve of LAO capped SRO film shows Curie temperature ( $T_C$ ) of ~115K (~90K), similar to that of 5 (4) u.c.-SRO film without LAO capping layer. **e-h.** first derivatives of a-d. Arrows denote  $T_C$ . Since the  $T_C$  of empirical fitting function is onset value, there are ~10K of difference between peak position in first derivatives and  $T_C$ .

- Fig. 5-6** **a, b.** Fitted  $\rho_{\text{AHE}}-H$  curves of LAO capped SRO samples with growth pressure for LAO layer of 5 and 1 mTorr. Gray lines are experimental curves and red and blue curves are negative and positive fitting curves. Green lines are summations of fitting curves. **c.** Temperature dependence of normalized  $\rho_{\text{AHE}}$  values extracted from the fitting. The closed circles come from 4 and 5 u.c. SRO films without the LAO capping layer. The open symbols are LAO capped SRO. The red (blue) denotes the negative (positive) component from the fitting.
- Fig. 5-7** A control experiment with total pressure variation during the growth of the LAO capping layer. **a.**  $\rho_{\text{AHE}}-H$  curves of LAO/SRO heterostructure grown at relatively high pressure. The total pressures ( $P_{\text{Total}}$ ) are 100 and 50 mTorr, while the partial pressures of Ar and O<sub>2</sub> are varied. **b-e.**  $\rho_{\text{AHE}}-H$  curves with varying the  $P_{\text{Total}}$  from 15 mTorr to 0.5 mTorr. The O<sub>2</sub> partial pressure is fixed as 0.5mTorr, while Ar partial pressure is only varied. Gray lines are experimental curves and red and blue curves are negative and positive fitting curves. Green lines are summations of fitting curves.
- Fig. 5-8** Schematics of the kinetic process during the growth of the LAO capping layer on the SRO films. At high-pressure conditions, the kinetic energy of evaporated plume is suppressed, while low-pressure conditions degraded SRO films with high kinetic energy. The degraded regions in SRO film exhibit 4 u.c.-like behavior resulting hump signal in the  $\rho_{\text{AHE}}-H$  curve.

---

# Abstract

Perovskite oxides have exotic functionalities such as ferroelectricity, magnetism, metal-insulator transition, and superconductivity. Those properties are coupled with their specific crystallographic character based on their oxygen octahedral structure. The interplay between the *B*-site cation and the oxygen is related to the size, shape, and rotation of the  $BO_6$  octahedra. An effective way to control the oxygen octahedra of perovskite oxides is thin-film engineering. With a thin film approach, an interfacial coupling can be utilized as a tuning knob of oxygen octahedra. In this dissertation, we address the important factors for interfacial engineering and the way of manipulating them.

First, we investigated the proper buffer template for the commensurate epitaxial growth of large-latticed perovskite;  $BaBiO_3$  ( $a = 4.374 \text{ \AA}$ ), which is a charge-density-wave insulator from its intrinsic octahedral breathing distortion. Using a  $BaZrO_3/BaCeO_3$  bilayer buffer template, we overcame the misfit dislocation accumulation problem and realized a fully commensurate epitaxial  $BaBiO_3$  film for the first time. Most of the misfit dislocations are accommodates in the  $BaZrO_3$  arbitrating layer while the  $BaCeO_3$  layer provides a clean interface for growing  $BaBiO_3$  thin films. Using this system, we provide a more accurate critical thickness of the octahedral breathing distortion due to the fundamental symmetry breaking of octahedra at the surface and the heterointerface.

Second, the effect of surface termination was examined. It is well known that the termination of the ultra-thin film determines the alternating polarity of perovskite oxides. We found the surface termination also plays an important role in the octahedral symmetry even without the alternating polarity. To examine it, we developed a water-leaching technique to convert the surface termination of SrRuO<sub>3</sub> films from SrO to RuO<sub>2</sub>. With this method, the surface-metal insulator transition of SrRuO<sub>3</sub> films was observed. Our findings show the clear relationship between the octahedral crystal field and the surface termination, which governs orbital occupancy and associated electronic structure dramatically.

At last, we explored the effect of the LaAlO<sub>3</sub> capping layer on the SrRuO<sub>3</sub> films. The anomalous Hall effect of SrRuO<sub>3</sub> is known to be sensitive to the various physical parameters, while its mechanism can be diverse, and thus, it is still under debate. Recently, the inhomogeneity induced two-channel anomalous Hall effect has attracted much attention, but the systematic approach of it has seldom been addressed. Here, we found that the capping layer can induce artificially tunable inhomogeneity into the SrRuO<sub>3</sub> film by the kinetic process. The induced inhomogeneity would give effective thickness variation of the film, resulting in a two-channel anomalous Hall effect.

**Keywords:** Perovskite oxides, Thin film, Interfacial engineering, Buffer layer, Surface termination, Capping layer, BaBiO<sub>3</sub>, SrRuO<sub>3</sub>, Octahedral distortion, Metal-insulator transition, Anomalous Hall effect.

**Student number:** 2015-20349

---

# Chapter 1

## Introduction

*A physicist is an atom's way of knowing about atoms.*

- Geroge Wald-

### 1.1 Perovskite oxides

Perovskite oxides have attracted much attention with their versatile physical properties such as ferroelectricity, magnetism, metal-insulator transition, and superconductivity [1–3]. Therefore, the understanding and controlling of those functionalities have become mainstream of condensed matter physics and real-world application.

Perovskite oxides are defined by their simple pseudo-cubic crystallographic structure and stoichiometry ( $ABO_3$ ;  $A$  = alkali and rare-earth,  $B$  = transition metal,  $O$  = oxygen). The strong bonding between  $B$ -site cation and oxygens forms corner-sharing  $BO_6$  octahedron. As shown in **Fig. 1-1**, The six-coordinated  $B$ -site cation and oxygen ligands form octahedral crystal field splitting of energy level. Within the cubic symmetry,  $e_g$  and  $t_{2g}$  degenerated orbital levels are formed [4]. However, a slight distortion of oxygen octahedra results in

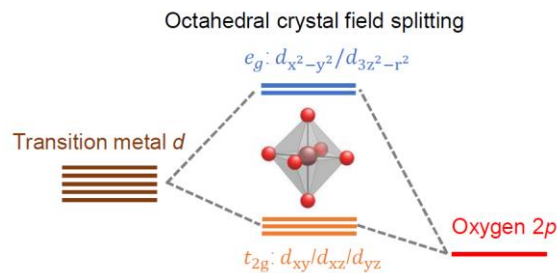


**Fig. 1-1** Schematic diagram of octahedral crystal field splitting of perovskite oxides.



the further splitting of degeneracy. Besides, the shape, size, and rotation of  $BO_6$  octahedra determine  $B$ -O bond length, charge and orbital ordering, and associated symmetries [5]. Therefore, oxygen octahedral engineering of perovskite oxides is a key to understand their functionalities.

The transition metal oxides typically have a strong electron-electron ( $e$ - $e$ ) correlation due to  $d$ -orbital electrons. In perovskite oxides, this Coulomb interaction between electrons affects exchange interaction [6]. Therefore, in order to explain the magnetism and conduction of this material, a strong correlation should be considered. Intriguingly, since the exchange interaction can be mediated by oxygen ligands, oxygen octahedron also plays an important role in the  $e$ - $e$  correlation physics of perovskite oxides [7].

## **1.2 Interfacial engineering of ultra-thin films**

An effective way to control the oxygen octahedra of perovskite oxides is thin-film engineering [5,8–10]. Due to their simple structural similarity, perovskite oxides can be a building block of the artificial heterostructure. The corner-sharing nature of oxygen octahedra makes their structural symmetry propagate into different layers [**Fig. 1-2a**]. As an example, on the higher structural symmetry substrate (*e.g.* cubic  $SrTiO_3$ ), the film with lower structural symmetry (*e.g.* orthorhombic  $SrRuO_3$ ) shows the tendency to have a tetragonal structure near the interface [11]. However, this structural symmetry propagation only holds for a few unit cells from the interface. Far from the interface, the film recovers its bulk structure with the relaxation. Therefore, we should consider the proper length scale

for interfacial engineering.

Not only the symmetry propagation but also the strain induced by the substrate is a crucial factor for interfacial engineering [**Fig. 1-2b**]. The in-plane biaxial strain is imposed when there is a misfit lattice between the substrate and the film. Under the strain, we could dramatically tune the functionalities of oxides, which do not exist in the bulk material [12–14]. Biaxial strain breaks the cubic symmetry of oxygen octahedra and affects their crystal field, Brillouin zone shape, and electronic band structure. However, there is a mechanical limit of applied elastic strain by thin film epitaxy. Most oxides are brittle and will crack if

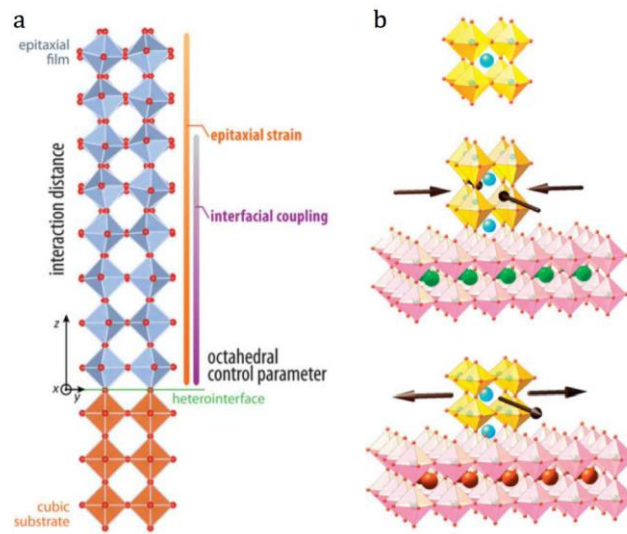


**Fig. 1-2 a.** Schematic illustration of the octahedral symmetry propagation. The cubic symmetry of the substrate propagates into the film material suppressing the octahedral rotation. Adapted from J. M. Rondinelli *et al* (2012) [5]. **b.** Schematics of epitaxial strain engineering. The film is under the in-plane biaxial compressive (tensile) strain from the substrate with the smaller (larger) lattice constant. Adapted from D. G. Schlom *et al* (2014) [13].

the applied strain exceeds a few percent [13]. If the lattice mismatch between the substrate and film is too large, the film material relaxes rapidly by the formation of misfit dislocations, which result in quality degradation like huge mosaicity. To overcome a large lattice mismatch, usage of the proper buffer layer would be helpful.

In an ultra-thin regime, the role of the interface becomes more important. Since the volume ratio of the interfacial region is increasing when the film becomes thinner, the property contribution from the interface becomes dominant. At the interface and the surface (also can be considered as a vacuum-film interface), the translation and inversion symmetry of bulk crystal unit cells are broken. Therefore, the interface and the surface of a film always show different physical properties compared with bulk. Since the physics of ultra-thin film is governed by the interface, engineering it is the effective tuning knob of functional oxides.

### **1.3 Outline of Thesis**

In this dissertation, the discussion regarding “**what is important for the interfacial engineering of perovskite oxides and how to control it**” will be provided. After explaining the main experimental methods in **chapter 2**, the result from three topics will be discussed in **chapters 3, 4, and 5**. Each topic is a buffer layer, surface, and capping layer, respectively.

In the **buffer layer** chapter, the bilayer buffer template to grow commensurate epitaxial  $\text{BaBiO}_3$  films and associated suppression of breathing distortion is discussed.  $\text{BaZrO}_3/\text{BaCeO}_3$  bilayer buffer template is designed to overcome the large lattice mismatch

between the substrate and the BaBiO<sub>3</sub> film. Using this template, we found the fundamental critical thickness of octahedral breathing distortion in BaBiO<sub>3</sub> film.

In the **surface** chapter, the water-leaching method to convert surface termination of SrRuO<sub>3</sub> films and associated surface metal-insulator transition is investigated. Using the different solubility of atomic layers, we converted the surface termination of the SrRuO<sub>3</sub> film for the first time. The detailed mechanism regarding surface crystal field splitting is investigated using various experimental methods.

In the **capping layer** chapter, control of inhomogeneity in SrRuO<sub>3</sub> films and related anomalous Hall effect is reported. The kinetic effect of the capping layer is analyzed. By controlling the growth pressure of the capping layer, we utilized it as a tuning knob of the kinetic process and solved the problem regarding the two-channel anomalous Hall effect, which has been a recent controversy.

As a last, the answer to the first question - what is important for the interfacial engineering of perovskite oxides and how to control it - will be provided as a summary in the conclusion chapter.

---

# Chapter 2

## Experimental Methods

*A method is more important than a discovery,  
since the right method will lead to new and even more important discoveries.*

- Lev Landau -

### 2.1 Pulsed laser deposition

All the films used for this research are fabricated using the pulsed laser deposition (PLD) technique [1]. PLD method is the deposition of a thin film on a substrate by using the ablation of a pulsed laser to the bulk target material [**Fig. 2-1**]. When the laser ablates a target, the evaporation from a target forms a plume that reaches the substrate and crystallizes into a thin film. During the growth, the substrate is annealed, and oxygen flows inside the chamber to help the crystalline and oxidization process.

The quality of the thin film made by the PLD method is known to be higher than the conventional sputtering method and comparable with the molecular beam epitaxy method. One advantage of PLD is the rapid growth optimization for various materials. Another advantage of PLD is diverse growth parameters such as laser fluence, substrate temperature, oxygen partial pressure, target to substrate distance, and target stoichiometry. The wide range of growth parameters provides the flexibility of the film deposition. However, those parameters are entangled with each other and sometimes become a hardship of PLD growth. Therefore, the systematic control of growth parameters is important for the PLD method.

As shown in **Fig. 2-1**, The PLD system used for this research consists of a KrF excimer laser (COHERENT, USA;  $\lambda = 248$  nm) and a vacuum chamber (PASCAL co., Japan; Base pressure  $< 10^{-8}$  Torr). The excimer laser beam is focused on the target surface using the combination of laser optics. The chamber contains a target carousel that helps the *in-situ* exchange of targets for heterostructure growth. The target rotates during the growth for the uniform ablation. During the growth, the substrate is annealed by an infrared laser. The temperature of the substrate is controlled by manipulating the current supplied to the infrared laser. The most advantage of this PLD system is the *in-situ* reflection high-energy electron diffraction (RHEED) system. It monitors the electron diffraction from the substrate and film during the deposition. By analyzing the diffraction pattern and its intensity, the lattice structure, surface reconstruction, and growth dynamics of the thin film can be monitored.

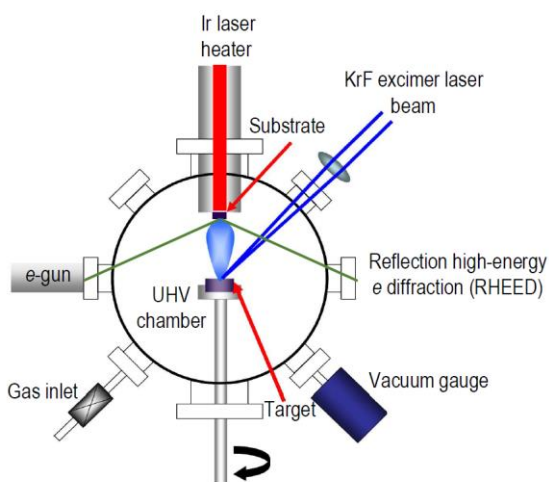


**Fig. 2-1** Schematic illustration of the pulsed laser deposition technique.

## **2.2 Structure and surface characterization**

The lattice structure of the thin film is characterized by high-resolution X-ray diffraction (XRD) [2]. The XRD machine (Bruker-D8; Bruker, Germany) for this research is designed to perform the thin film analysis with a 4-circle goniometer and high-intensity rotating anode. Using a CuK- $\alpha$  X-ray ( $\lambda = 0.15406$  nm), the out-of-plane constant of a thin film is easily obtained through Bragg's law. As a reference, a substrate peak position is used. Measuring in-plane lattice constant in film geometry is trickier than out-of-plane. Measurement. To obtain it, reciprocal space mapping is performed, since the mapping can contain an in-plane axis. The crystallinity of the film is also investigated with a rocking curve, which is an intensity profile near the film peak position. The higher the crystallinity is, the sharper the rocking curve is. X-ray reflectometry (XRR) is also conducted to measure the thickness of the film [3]. For the ultra-thin film, the XRD and XRR experiments are performed using the accelerator light (Pohang Light Source, Korea). Since the signal to noise ratio from the ultra-thin films is too low, a much higher X-ray intensity from the accelerator is required.

The surface morphology of the thin film is characterized by atomic force microscopy (AFM) [4]. The most efficient method to measure the surface topography by AFM is AC-tapping mode. In AC-tapping measurement, a small tip attached to the cantilever is put near the sample surface. The displacement of the tip is measured by detecting the reflection of a laser beam from the tip. During the measurement, the tip oscillates with AC driving frequency. Since the tip is near the surface of the sample, the atomic force between the

sample surface and tip acts as an additional external force. Therefore, the motion of the AFM tip can be described as a damped harmonic oscillator with AC driving force. By detecting the phase and amplitude of the tip oscillation, the distance between the sample and the tip is estimated. Therefore, by scanning a certain area, the surface morphology of the thin film is obtained. Furthermore, advanced analyzes are possible with phase mapping. The advanced AFM technique will be discussed in **Chapter 4** in more detail. In this research, Cypher AFM machine (Asylum Research, USA) is used.

## **2.3 Transport measurement**

The temperature-dependent resistivity of the thin film implies important physical information of the sample [5]. For example, the resistivity-temperature curve determines its metallicity and Fermi liquidity from the density of state near the Fermi level. In addition, the resistivity combined with an external magnetic field (i.e. magnetoresistance and Hall effect) contains information about the spin majority, carrier density, spontaneous magnetization, and even band topology.

To extract the physical parameters of the sample by transport, precise device fabrication is required. Thin film geometry has the advantage that it is easy for device processing. In this research, the Hall bar device is fabricated elaborately using the photolithography and the ion milling method. The electrode for wire connection is deposited using an *e*-beam evaporator. To avoid the contact resistance effect, all the electrode is designed for 4-probe geometry. A Physical Property Measurement System (PPMS; Quantum Designs, USA) is



used for the (magneto-) transport measurement.

## **2.4 Spectroscopic measurement**

The spectroscopic measurement for this research is mainly done by an ellipsometer (J. A. Woollam, USA). The ellipsometry technique is measuring the polarization dependence of reflected light from the sample [6]. The incident light has two perpendicular polarization components. The intensity ratio and rotated angle of reflected polarization components can be converted into the complex dielectric constant of the sample following Maxwell's equation inside the material. In the case of thin film, the reflection occurs at the substrate-film interface and film surface. Therefore, the thickness of the film becomes important to calculate the complex dielectric constant of the film. In this research, the thickness obtained by XRR is used for the calculation. The advantage of this technique is high reliability due to its self-consistent nature from the Kramers-Kronig relation. Furthermore, by varying the energy (wavelength) of the light, we get information about the band structure. For example, if there is a gap at certain energy of the band structure, the imaginary dielectric constant spectrum shows the peak at that energy.

Another spectroscopic technique used in this research is Raman spectroscopy [7]. It measures Raman shift, which comes from the inelastic scattering of light resulting in frequency shift. It is typically used to investigate vibrational phonon modes in a solid. Since each phonon mode has its eigenfrequency and Raman shift value, the Raman shift measurement provides a fingerprint of its structural symmetry.

---

# Chapter 3

## Results and Discussion I: Buffer Layer

*What we observe is not nature itself, but nature exposed to our method of questioning.*

- Werner Heisenberg -

### 3.1 Introduction: BaBiO<sub>3</sub>

BaBiO<sub>3</sub> (BBO) is a charge-density-wave (CDW) insulator [1,2]. It has the characteristic oxygen octahedral distortion, which is called an octahedral breathing distortion (OBD) [3]. Two neighboring BiO<sub>6</sub> octahedra have alternating sizes: one expanding and the other shrinking. This alternating size variation does not break the cubic point symmetry, (*i.e.*,  $A_{1g}$  symmetry) but results in lattice doubling. This structural change is related to a strong hybridization of Bi-6s and O-2p orbitals, which makes the Bi covalency alternate, and forms a CDW. The CDW of BBO opens a 2eV gap near the Fermi surface and makes BBO insulating [1,4,5] [Fig. 3-1].

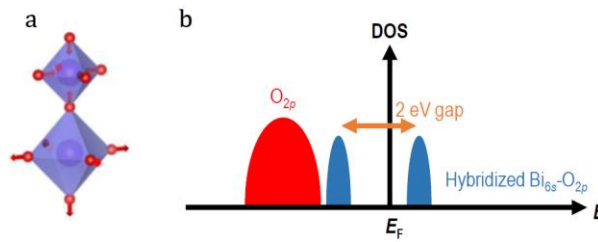


**Fig. 3-1** **a.** Schematic illustration of oxygen octahedral breathing distortion. **b.** Schematic density of state (DOS) diagram of BaBiO<sub>3</sub> due to breathing distortion. The 2eV gap opening occurs at the Fermi level ( $E_F$ ).

The OBD and related CDW can be observed via Raman spectroscopy and optical ellipsometry. Since OBD has  $A_{1g}$  symmetry, it activates the characteristic Raman shift at  $565\text{ cm}^{-1}$  [6]. If there is breaking of OBD, the strong Raman response of  $565\text{ cm}^{-1}$  is suppressed. Regarding the CDW feature, the CDW creates a density of states below and above the Fermi level of its electronic band structure, resulting in a strong optical absorption around  $2\text{eV}$  [4,5]. By measuring the dielectric spectrum with spectroscopic ellipsometry, the formation of CDW can be addressed. For example, in chemically doped bulk BBO, the suppression of OBD and the associated CDW was observed by these two spectroscopic measurements. Furthermore, it is found that the suppression of OBD and CDW can induce a superconducting transition with a high critical temperature of  $34\text{ K}$  [7]. Since this material has characteristic octahedral distortion and associated properties, it would be also intriguing to control its octahedra by interfacial engineering.

However, the interfacial engineering of BBO thin film has intrinsic obstacles. The in-plane lattice constant of BBO is  $4.374\text{ \AA}$ , which is much larger than commercially available perovskite oxide. For example, the widely used  $\text{SrTiO}_3$  (STO) substrate has a lattice constant of  $3.905\text{ \AA}$ . The lattice mismatch between BBO and STO is  $\sim 12\%$ , which makes commensurate growth impossible. With this large lattice mismatch, BBO film grown on STO substrate is always fully relaxed [8], thus the interfacial effect cannot propagate. Therefore, it would be helpful to develop a suitable template for growing large oxides like BBO.

### 3.2 Bilayer buffer template

In order to overcome the large lattice between the STO substrate and the BBO film, proper usage of a buffer layer is required. This buffer layer technique has been used to alleviate large lattice mismatch [9,10]. For example, the growth of high-quality GaN and ZnO on Al<sub>2</sub>O<sub>3</sub> substrates was realized by overcoming a mismatch problem through the usage of buffer layers. Here, we utilize a template composed of two buffer layers: an arbitrating layer and a main-buffer layer [11,12]. The main-buffer layer is used to provide a desired commensurable lattice for the target material (BBO), with a lattice mismatch of less than a few percent. For this purpose, we use BaCeO<sub>3</sub> (BCO,  $a = 8.777 \text{ \AA}$ ,  $b = 6.236 \text{ \AA}$ , and  $c = 6.216 \text{ \AA}$ ; orthorhombic in bulk) because of the small lattice mismatch between BBO and BCO (0.43%), in the pseudo-cubic notation [13]. However, there remains a lattice mismatch between BCO and STO, of 12.4%. To obtain a high-quality BCO layer, it is necessary to insert an arbitrating layer between the BCO main-buffer layer and the STO substrate. We use BaZrO<sub>3</sub> (BZO,  $a = 4.192 \text{ \AA}$ ; cubic in bulk) as the arbitrating material [14]. With the intermediate lattice constant, lying between those of BCO and STO, this BZO layer can arbitrate the large lattice mismatch.

Regarding the growth of a single BCO layer on the STO substrate, the large lattice mismatch of 12.4% degrades the crystalline structure of the BCO layer. As shown in **Fig. 3-2a**, the XRD rocking curve of a 12 nm-thick BCO layer shows a very broad feature, indicative of the mosaicity spread in the crystal structure [15]. The large full width at half-maximum (FWHM) value of the broad feature indicates a huge in-plane inclination [16].

The rocking curve exhibits a small Gaussian component which indicates the existence of a crystallized region with a small volume, but a large mosaicity spread made it unsuitable for use as a buffer template. The AFM image in **Fig. 3-2b** shows a surface with a high roughness value of 0.91 nm. The line profile along the white line in **Fig. 3-2c** does not show any step-and-terrace topography from the substrate.

On the other hand, the growth of a high-quality BCO layer (12 nm) on STO is possible

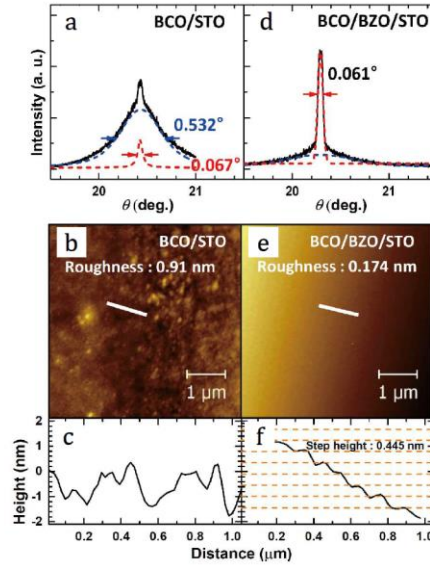


**Fig. 3-2** X-ray diffraction (XRD) rocking curve for (002) diffraction of BaCeO<sub>3</sub> (BCO) layers on **a.** the SrTiO<sub>3</sub> (STO) substrate and **d.** the BaZrO<sub>3</sub> (BZO)-arbitrating layer. Red and blue dashed lines are a Gaussian component and background component of raw data. Arrows indicate full-width at half maximum values of fitting curves. The pseudo-cubic notation was used for indexing all reflections. Atomic force microscopy (AFM) topographic images of the BCO layers on **b.** the STO substrate and **e.** the BZO arbitrating layer. A line profile along the white line in **b** (**e**) was plotted in **c** (**f**). Adapted from H. G. Lee *et al* (2016) [12].

by inserting a BZO arbitrating layer (10 nm). This double-layer structure has a sharp rocking curve for the BCO layer, with a small FWHM value of  $0.061^\circ$  [Fig. 3-2d]. This suggests that the mosaicity problem could be overcome by using a BZO-arbitrating layer. Furthermore, the surface roughness is significantly less, at about 0.174 nm [Fig. 3-2e]. The line profile along the BCO surface shows a step-and-terrace pattern [Fig. 3-2f]. The height of each step is  $\sim 0.44$  nm, within the experimental resolution of AFM. This height value is consistent with the out-of-plane lattice constant of the BCO film measured by XRD.

The reason why the growth of high-quality BCO is possible with the BZO layer is the high density of accommodated misfit dislocations in the BZO arbitrating layer. Fig. 3-3a shows a scanning transmission electron microscope (STEM) image of the BCO/BZO/STO heterostructure. This image reveals well-defined sharp interfaces and epitaxial growth of thin films. Fourier-filtered images of the two red square areas [Figs. 3-3b, c] reveal several edge dislocations near the interfaces; the white circles in Fig. 3-3b indicate edge dislocations near the interface between STO and BZO layers, and Fig. 3-3c shows two dislocations appearing at the BZO/BCO interface and in the BZO layer. This indicates that strain relaxation occurred throughout the high density of misfit dislocations inside the intermediate BZO layer. The relatively little dislocation density within the BCO layer makes BCO/BZO double-layer buffer template an ideal platform for growing commensurate epitaxial films with a large lattice constant.

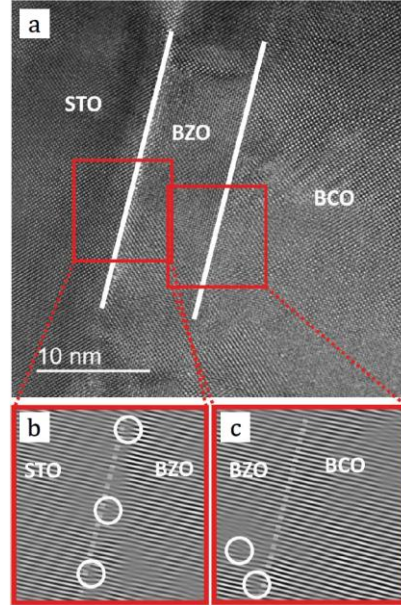


**Fig. 3-3 a.** High-resolution transmission electron microscopy (HRTEM) image of the double-layer buffer structure on the STO substrate. **b.** and **c.** Fourier-filtered images of the red squares in **a**, using the (100) location. The white circles indicate the positions of misfit dislocations, and the white lines indicate the interfaces between layers. Adapted from H. G. Lee *et al* (2016) [12].

The growth of high-quality commensurate epitaxial BBO films becomes possible with the BCO/BZO double-layer buffer template. **Fig. 3-4** shows sample geometry and XRD results of three different BBO structures: BBO/STO, BBO/BCO/STO, and BBO/BCO/BZO/STO. As previously reported, BBO thin films can be grown directly on STO substrates, but only in a fully relaxed state [**Figs. 3-4a-c**]. When only a single BCO buffer layer was used, the quality of both the BCO buffer and the BBO thin film was seriously degraded [**Figs. 3-4d-f**]. This was due to the large mosaicity and associated defects in the BCO layer. On the other hand, the BBO layer on the double-layer buffer

structure received epitaxial strain from the BCO layer. As shown in the reciprocal space map (RSM) of **Fig. 3-4h**, the in-plane peak position of the BBO is aligned with that of the BCO, suggesting that the BBO layer was commensurately grown and fully strained (0.48%) against the BCO layer. The XRD rocking curve in **Fig. 3-4i** shows a high-crystalline structure compared with the single buffered sample.

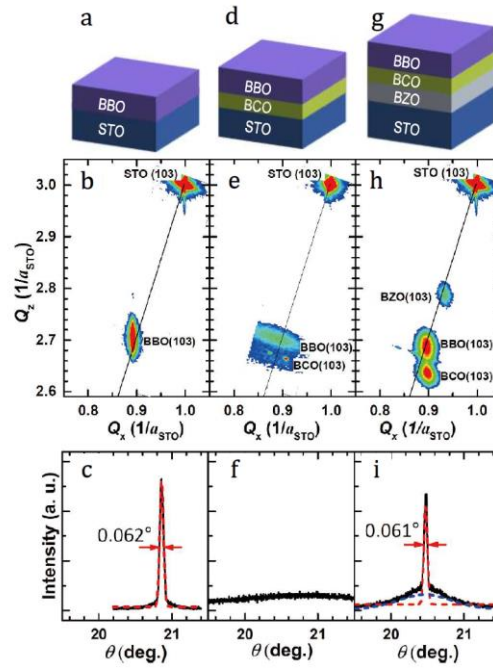


**Fig. 3-4** Schematic sample structures of **a.** BBO/STO, **d.** BBO/BCO/STO, and **g.** BBO/BCO/BZO/STO. **b.**, **e.**, and **h.** Reciprocal space maps (RSMs) around STO (103) diffraction measured from **a.**, **d.**, and **g.**, respectively. The black lines are cubic relaxation lines from STO (103). **c.**, **f.**, and **i.** XRD rocking curves at BBO (002) diffraction from **a.**, **d.**, and **g.**, respectively. Red and blue dashed lines are a Gaussian component and background component of raw data. Arrows indicate full-width at half maximum values of rocking curves. The pseudo-cubic notation was used for indexing all reflections. Adapted from H. G. Lee *et al* (2016) [12].



### 3.3 Anisotropic suppression of breathing distortion

By the insertion of a bilayer buffer template, the interfacial effect on the BBO film can be investigated more precisely. We investigated the structural evolution of OBD by measuring the Raman response as a function of BBO thickness [17], as shown in **Fig. 3-5a**. Raman spectra of BBO were obtained using 633-nm-wavelength laser irradiation ( $\sim 1.96$  eV) to maximize the Raman response via resonance with the strong absorption peak of BBO ( $\sim 2.0$  eV). A strong Raman response at  $565\text{ cm}^{-1}$  and its second harmonic at  $1,130\text{ cm}^{-1}$  were quite evident for the 20-u.c.-thick BBO sample. However, with a decrease in BBO film thickness, the Raman response at  $565\text{ cm}^{-1}$  was gradually suppressed. Below 6 u.c., the Raman signature at  $565\text{ cm}^{-1}$  becomes completely vanished, resulting in Raman spectra similar to that of the BCO/BZO/STO sample. It indicates that the  $A_{1g}$  symmetric phonon mode related to OBD should become suppressed at 6 unit cell (u.c.). Above this critical thickness, the OBD-related  $A_{1g}$  mode becomes recovered in BBO. However, it cannot be explained by the simple strain relaxation, since BBO films on the BCO layer are fully-strained up to 20 u.c.

The evolution of the CDW feature due to the OBD suppression was also investigated in optical conductivity spectra  $\sigma_1(\omega)$ , as shown in **Fig. 3-5b**. As shown by a red line, the 20-u.c.-thick BBO film showed a significant peak at 2.05 eV [4,5]. Interestingly, the peak gradually becomes weakened with a reduction in BBO film thickness. The close relationship between suppression of the  $A_{1g}$  Raman mode and the CDW absorption peak was displayed in **Fig. 3-5c**. Raman intensities at  $565\text{ cm}^{-1}$ , the characteristic Raman shift

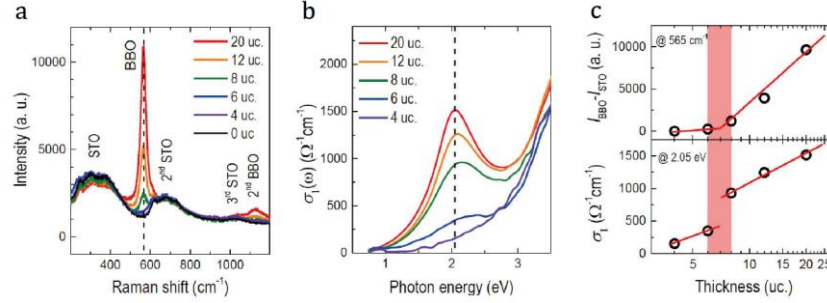


**Fig. 3-5** **a.** Raman responses of fully strained BBO with the variation of film thickness when the sample is exposed to 633-nm laser irradiation. The first and second harmonics at 565 cm<sup>-1</sup> and 1,130 cm<sup>-1</sup> are excited due to the oxygen octahedral breathing phonon modes of BBO. **b.** Optical conductivity spectra of BBO films with variation in film thickness. The absorption maximum at 2.05 eV comes from direct optical transitions across the charge-density-wave gap in BBO. **c.** Summary of the evolution of Raman intensity values at 565 cm<sup>-1</sup> and optical conductivity values at 2.05 eV as a function of BBO film thickness. Both values show discontinuity near 6–8 u.c. as highlighted in red. Solid lines are guides for the eye. Adapted from H. G. Lee *et al* (2018) [17].

for OBD, are plotted as a function of BBO thickness in the upper section. Optical conductivities at 2.05 eV, the characteristic CDW feature, are plotted in the bottom section. These two plots clearly show similar discrete behaviors near 6~8 u.c., as highlighted in the red highlighted region. Above the boundary, bulk-like OBD and associated CDW becomes recovered. However, the Raman response of 6 u.c. the sample was completely suppressed, while  $\sigma_1(\omega)$  peak shows a small trace of spectral weight at 6 u.c. The difference between Raman and  $\sigma_1(\omega)$  response will be discussed later with the concept of anisotropic suppression of OBD.

The mechanism of OBD suppression in ultra-thin BBO film is explained by density

functional theory (DFT) calculation. We used DFT with the projector-augmented wave method, as implemented in the Vienna Ab initio Simulation Package (VASP) code [18,19]. The plane-wave energy cutoff was set at 600 eV, and an  $8 \times 8 \times 1$   $k$ -point mesh was used for a  $\sqrt{2} \times \sqrt{2}$  slab. We determined the magnitude of oxygen displacement in each mode by comparing the atomic positions with those calculated for the  $1 \times 1$  BBO slab, which does not have OBD due to the absence of neighboring octahedra. **Fig. 3-6a** shows how the

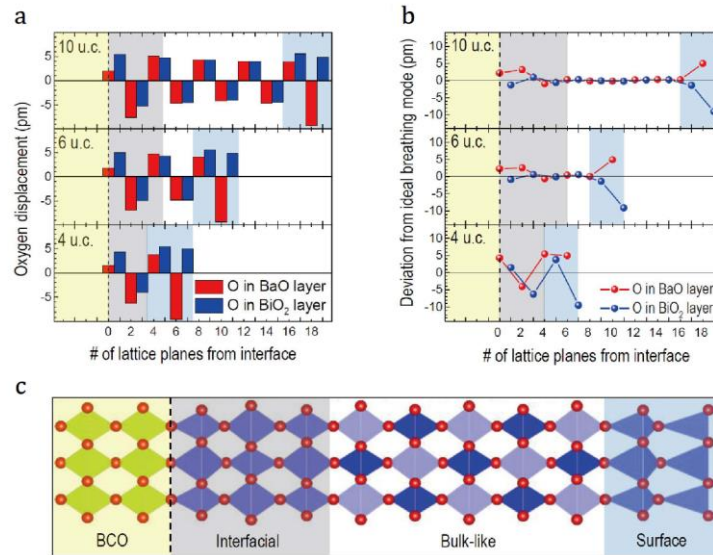


**Fig. 3-6 a.** Calculated oxygen displacement in each unit cell of BBO with different lattice planes. The BCO sublayer is in the yellow background. At the BBO/BCO interface (gray-colored) and the BBO surface (blue-colored), the oxygen up-down mode in BaO slabs is broken while the change in the oxygen expanding-shrinking mode in BiO<sub>2</sub> slabs is negligible. **b.** The oxygen displacement deviation from the ideal breathing mode. The value 0 represents the ideal breathing pattern. **c.** The schematics of 10-u.c.-thick BBO on BCO sublayer. The octahedral structure of BBO with distinct three regions was displayed with an exaggerated scale. Adapted from H. G. Lee *et al* (2018) [17].

calculated magnitudes of oxygen displacement modes will vary in terms of distance from the heterointerface. It might be easier to look at the deviation of the oxygen positions from those of the ideal breathing mode. The magnitudes of oxygen displacement modes are converted into the deviation from ideal OBD (with cubic  $A_{1g}$  symmetry) [**Fig. 3-6b**].

As schematically shown in **Fig. 3-6c**, inside the BBO layer, there are three distinctive regions, which we will call interfacial, bulk-like, and surface regions. For example, let us look at **Figs. 3-6a** and **b** for the 10-u.c.-thick BBO film. At the first 3 u.c. of the interfacial region (gray colored), the oxygen up-down mode in the BaO slab becomes strongly suppressed in the first unit cell, but enlarged in the second unit cell. In the bulk-like region (without any background color), residing at 3–7.5 u.c., oxygen displacement modes are close to those of the ideal OBD, namely alternative oxygen displacements in either the BaO or BiO<sub>2</sub> slab. In the surface region (blue colored), oxygen up-down modes are enlarged and expanding-shrinking modes are inverted in the sign at the top layer resulting in a huge deviation from ideal OBD. Note that the detailed displacement pattern of the oxygen modes at the interfacial and surface regions are significantly different.

This calculation shows that the suppression of OBD in ultra-thin BBO is anisotropic. At the interfacial region, oxygen up-down mode is suppressed at the first unit cell. However, there is no distinguishable change in the oxygen expanding-shrinking mode in the BiO<sub>2</sub> slab at the first unit cell. Our experimental ellipsometry studies are sensitive to in-plane optical absorption. The remained oxygen expanding-shrinking mode can explain incomplete suppression of 2eV peak at 6 u.c., observed in **Fig 3-5c**. In contrast, the Raman

response should be vanished immediately, since anisotropic suppression of OBD breaks  $A_{1g}$  symmetry completely. Note that the shape of octahedra in BBO cannot be arranged in the same geometry as that of non-breathing BCO. As a result, anisotropic distortion should occur in BBO due to different responses in each BaO and BiO<sub>2</sub> layer; thus, a new type of octahedral distortion emerges at the heterointerface, which breaks  $A_{1g}$  symmetry, OBD, and also partially associated CDW.

### **3.4 Conclusion**

By using the proper buffer layer, the fundamental thickness limit of the OBD of BBO is revealed. We established a systematic method to interpret the OBD in terms of oxygen up-down and expanding-shrinking modes. We found that the OBD suppression is anisotropic due to different responses of these two oxygen modes. This suppression occurs at both the heterointerface and the surface. In the previous report using the fully-relaxed BBO on STO substrate [8], the critical thickness of OBD suppression was 11 u.c. On the other hand, with the fully strained interface by using a double-layer buffer template, the critical thickness was decreased to 6 u.c. The 5 u.c. the difference comes from the dead-layer between the STO substrate and the BBO film. Recent follow-up studies show that this interfacial dead layer by grazing incidence XRD and STEM [20–22]. These results indicate that the BCO/BZO double-layer buffer structure is useful for the growth of various other oxide materials of large lattice constant ( $> 4.1 \text{ \AA}$ ). This double-layer buffer template can be applied to avoid large lattice mismatch induced dead layer problem in various perovskite oxides.

---

# Chapter 4

## Results and Discussion II: Surface

*God made the bulk; the surface was invented by the devil.*

- Wolfgang Pauli -

### 4.1 Introduction: SrRuO<sub>3</sub>

#### 4.1.1 Physical properties of SrRuO<sub>3</sub>

SrRuO<sub>3</sub> (SRO) is an itinerant ferromagnetic metal with a Curie temperature ( $T_C$ ) of  $\sim 160$  K [1]. Because of its high electrical conductivity and structural stability among the perovskite oxides, SRO epitaxial film has been widely used as an electrode layer for TMO-based devices [2–4]. Furthermore, a fine balance between  $e$ - $e$  correlation and spin-orbit coupling in SRO gives rise to a variety of novel physical properties, including itinerant ferromagnetism with non-Fermi liquid electrical transport, magnetic monopoles in momentum space, anomalous Hall effect (AHE), strong magnetocrystalline anisotropy, and topological Hall effect [5–9].

In the form of thin film, SRO has huge thickness dependence. The resistivity of SRO film is increasing in the ultra-thin regime, and even shows metal-insulator transition (MIT) at 2–3 u.c. thickness [10–13]. The magnetism of SRO thin film is also highly dependent on the thickness. The  $T_C$  and magnetization are degraded in an ultra-thin regime. AHE of SRO film shows more complex behavior with the thickness [6,14]. The coercive field, anomalous Hall conductivity, even the sign of AHE changes abruptly with the variation of

thickness. This sensitivity is related to its topological band structure [5,6,15], which will be discussed in **Chapter 5** with more details. Note that the sensitive behavior can be an indicator of the film thickness.

#### 4.1.2 Surface termination engineering of SrRuO<sub>3</sub> thin film

(001)-oriented epitaxial  $ABO_3$  perovskite film consists of AO and  $BO_2$  atomic layers alternately stacked along the pseudo-cubic [001] direction. As the film thickness reduces to several nanometers or unit-cells, surface termination (AO or  $BO_2$ ) starts to play a crucial role in determining the physical properties such as ferroelectric stability, spontaneous-

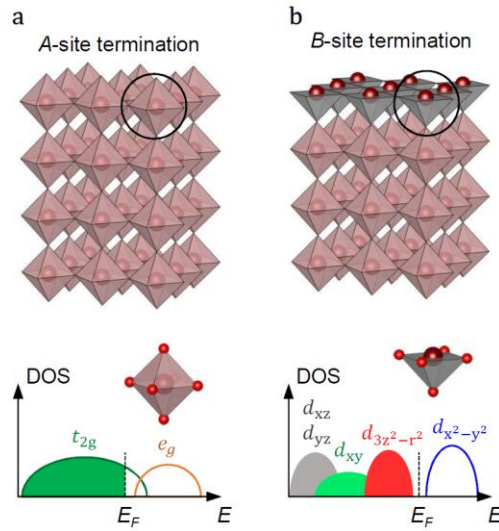


**Fig. 4-1** Schematics of termination engineering. **a.** At AO-terminated film,  $BO_6$  octahedral crystal field split the  $B$  4d band into  $t_{2g}$  and  $e_g$  subbands. The partially-filled  $t_{2g}$  band results in finite density-of-states (DOS) near the Fermi level ( $E_F$ ), signifying robust metallicity. **b.** At the  $BO_2$ -terminated film surface, on the contrary, the loss of apex oxygen breaks the  $BO_6$  octahedral symmetry. It further splits the  $t_{2g}$  and  $e_g$  bands. Adapted from H. G. Lee *et al* (2020) [27].

polarization direction, tunneling conductance, Schottky barrier height, and work function [4,16–21]. Conventionally, this concept of termination conversion is thought to be important in alternating-polar perovskites like  $\text{LaAlO}_3$  and  $\text{LaNiO}_3$  [19,22]. In these materials, the  $\text{AO}$  and  $\text{BO}_2$  layers have opposite charges, thus surface termination determines the built-in polarity of the thin film. However, even if alternating polarity does not exist, there is a possibility that the surface termination affects its functionalities by crystal field splitting. At the  $\text{AO}$ -terminated (001) surface or in bulk, the crystal field from  $\text{BO}_6$  octahedron split  $d$  band into  $t_{2g}$  and  $e_g$  subbands [23]. For metallic systems, one of the subbands should be partially filled (**Fig. 4-1a**). By contrast, at the  $\text{BO}_2$ -terminated (001) surface, the loss of apex oxygen may further split the  $t_{2g}$  and  $e_g$  bands and result in a gap opening (**Fig. 4-1b**).

SRO ultra-thin film can be a proper system to examine the crystal field hypothesis. Due to its high sensitivity, the effect of surface termination conversion can be amplified in its physical properties. However, *in-situ* termination engineering during the SRO film growth is prohibited by the distinct thermodynamic stability between  $\text{SrO}$  and  $\text{RuO}_2$  surface termination [24,25]. The  $\text{RuO}_2$  surface layer is highly volatile at the optimal growth temperature ( $\sim 700^\circ\text{C}$ ). Hence, the as-grown SRO film surface always exhibits a uniform  $\text{SrO}$  termination. Therefore, a novel method should be developed to realize  $\text{RuO}_2$ -terminated SRO films.



## 4.2 Water-leaching technique and surface termination conversion

The water solubility of AO and  $BO_2$  surface layers in many  $ABO_3$  perovskites are distinct, which makes water-leaching an effective method for selectively etching surface atomic layers. Although bulk SRO is resistant to most acid etching processes [1], the water solubility of SrO and  $RuO_2$  atomic layers are distinct at the surface: SrO can react with  $H_2O$  molecular to produce water-soluble  $Sr(OH)_2$ , whereas  $RuO_2$  cannot be dissolved in water [26]. Therefore, the structure change of as-grown SRO surface in water should have a self-limiting nature. Here, we ultrasonicated the as-grown SRO films in deionized water for various time durations ( $t_w$ ) to trigger a surface termination conversion from SrO to  $RuO_2$  [27].

The surface evolutions of SRO films during the water-leaching were observed via atomic force microscopy (AFM). After water-leaching the SRO film for various  $t_w$ , we acquired AFM height [Figs. 4-2a-e] and phase [Figs. 4-2f-j] images simultaneously. In addition to the topography, the surface chemical composition variations can also change sample-tip interaction, thus contributing to the phase contrasts. Therefore, the phase images can be a fingerprint of local surface termination variations [28,29]. In Fig. 4-2a, the height image of the as-grown sample ( $t_w = 0$ ) shows an atomically flat surface with one-unit-cell-high terraces. The corresponding phase image [Fig. 4-2f] shows negligible contrast except for the lines at terrace edges, indicating a uniform surface termination. After water-leaching for various  $t_w$ , the AFM height images [Figs. 4-2b-e] do not show notable changes either. In contrast, the phase images for  $t_w = 10$  and 30 s become highly inhomogeneous [Figs. 4-

**2g,h]**. The local phase difference exceeds  $2^\circ$ , signifying considerable variations in the

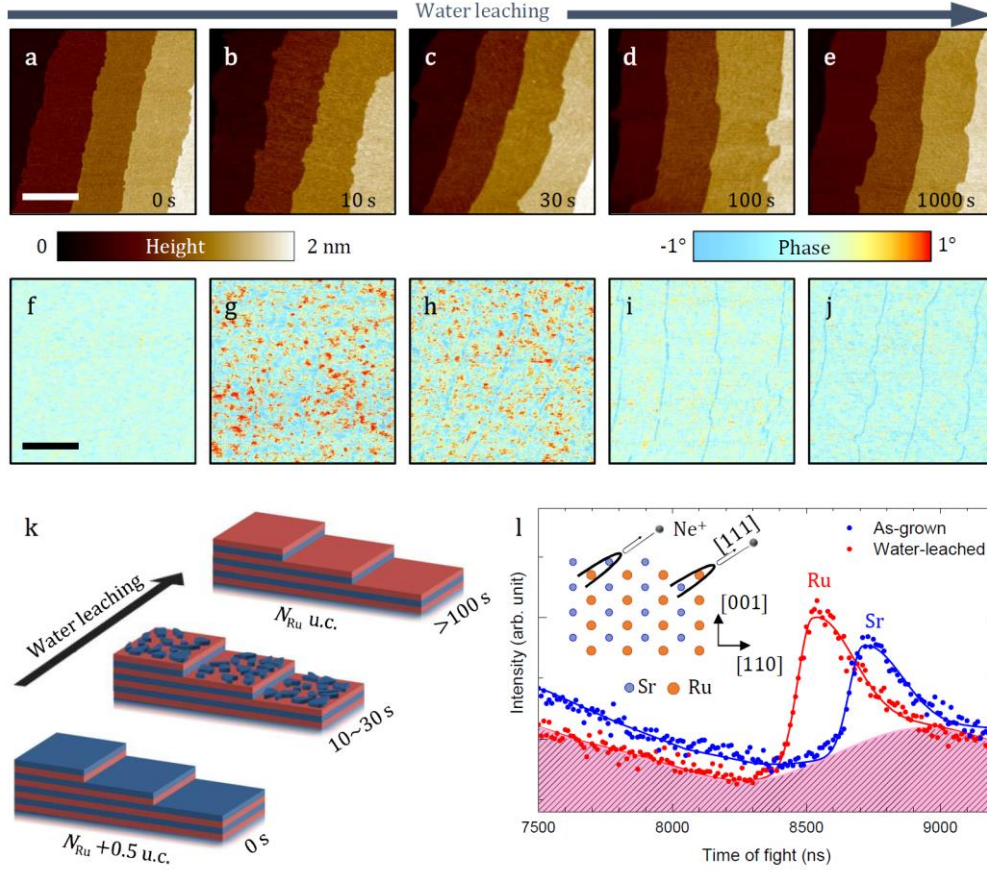


**Fig. 4-2** SRO surface termination conversion triggered by water-leaching. **a-j**. Atomic force microscopy topographic height images (**a-e**), and corresponding phase images (**f-j**) of the SRO thin film acquired after different water-leaching durations ( $t_w$ ). All the scale bars correspond to 300 nm. **k**. Schematics of surface termination evolution during water-leaching. The topmost SrO layer is gradually dissolved during water leaching. **i**. Coaxial impact-collision ion scattering spectroscopy measurements on the as-grown (blue) and water-leached (red) SRO(001) surfaces. The experimental spectra (dotted lines) can be well fitted (solid lines) via two Gaussian peaks. Adapted from H. G. Lee *et al* (2020) [27].

surface chemical composition. By further increasing  $t_w$  up to 100 s, the phase image becomes uniform again [Fig. 4-2i], and it remains stable even after additional water-leaching for  $t_w = 1,000$  s [Fig. 4-2j].

The surface termination conversion was further confirmed by coaxial impact-collision ion scattering spectroscopy (CAICISS) [30,31]. CAICISS is a low-energy ion scattering spectroscopy where the time-of-flight (TOF) of injected ions backscattered by atoms at a crystal surface is measured. The TOF profile is highly dependent on the masses of the surface atoms which cause backscattering. As shown in the schematic inset of Fig.4-2l, when the  $\text{Ne}^+$  ions are injected along the  $[111]$  axis toward the  $\text{SRO}(001)$  surface, because of the atomic shadowing effect, only the topmost atoms can affect the backscattering process. In this case, the TOF profile is extremely sensitive to surface termination. As shown in Fig.4-2l, TOF peaks of the as-grown ( $\sim 8,530$  ns) and water-leached ( $\sim 8,720$  ns) SRO films can be assigned to the backscattering processes from Sr and Ru atoms, respectively. The good Gaussian fitting further demonstrates uniform terminations at both as-grown (SrO) and water-leached ( $\text{RuO}_2$ ) film surfaces. In other words, the  $\text{RuO}_2$ -terminated SRO film has been realized for the first time via the water-leaching method.

### 4.3 Surface metal-insulator transition

Based on the uniformity in surface termination, we can define SRO film thickness ( $t_{\text{SRO}}$ ) with sub-unit-cell accuracy. We denote the number of  $\text{RuO}_2$  layers in the SRO film as  $N_{\text{Ru}}$ . The SrO-terminated SRO films grown on  $\text{TiO}_2$ -terminated  $\text{STO}(001)$  substrate consist of  $N_{\text{Ru}}+1$  SrO layers, while the  $\text{RuO}_2$ -terminated films consist of  $N_{\text{Ru}}$  SrO layers. The surface

termination conversion can strongly affect the longitudinal electrical transport and ferromagnetism of the SRO ultrathin films. Temperature-dependent longitudinal resistivity ( $\rho_{xx}$ - $T$ ) and magnetization ( $M$ - $T$ ) curves are shown in **Figs. 4-3a-d** and **Figs. 4-3e-h**, respectively. For the as-grown sample with  $N_{\text{Ru}} = 6$  ( $t_{\text{SRO}} = 6.5$  u.c., SrO-terminated), the

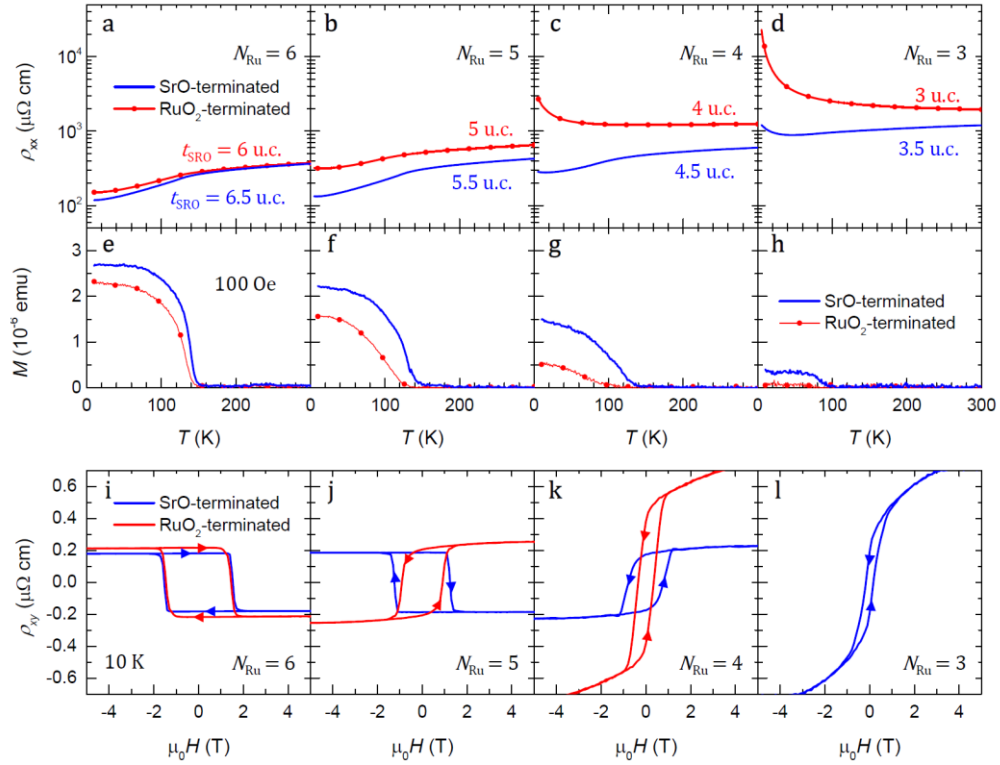


**Fig. 4-3** Electrical transport and magnetic characterizations of SRO ultrathin films. **a-h.** Temperature-dependent longitudinal resistivity (**a-d**) and magnetization (**e-h**) ( $\rho_{xx}$ - $T$  and  $M$ - $T$ ) curves of the SrO- (blue curves) and  $\text{RuO}_2$ - (red curves) terminated SRO films with various  $N_{\text{Ru}}$ . The  $M$ - $T$  curves are measured with an out-of-plane magnetic field ( $H$ ) of 100 Oe. **i-l.**  $H$ -dependent anomalous Hall resistivity ( $\rho_{\text{AHE}} - H$ ) curves measured at 10 K from the SrO- and  $\text{RuO}_2$ -terminated SRO films with various  $N_{\text{Ru}}$ . All of the ordinary Hall components have been subtracted for clarity. The  $H$  scanning directions are indicated by solid arrows. Adapted from H. G. Lee *et al* (2020) [27].

$\rho_{xx}$ - $T$  curve exhibits a bulk-like metallic behavior and a kink near  $T_C \sim 144$  K, where the corresponding  $M$ - $T$  curve also shows a well-defined paramagnetic-ferromagnetic transition. As  $N_{Ru}$  ( $t_{SRO}$ ) decreases,  $\rho_{xx}$  of the as-grown samples increases gradually. The  $\rho_{xx}$ - $T$  curve for the  $N_{Ru} = 3$  case even shows an insulating upturn at  $\sim 47$  K. The  $T_C$  and  $M$  in the ferromagnetic phase also decreases systematically with  $N_{Ru}$ . The observed decays in metallicity and ferromagnetism of the as-grown films are consistent with previous studies [10–13]. Interestingly, after water-leaching, the  $RuO_2$ -terminated samples show a clear increment in  $\rho_{xx}$  and reduction in  $M$ . Such a termination conversion-induced decays in both metallicity and ferromagnetism become more prominent as  $N_{Ru}$  decreases.

Similar to the longitudinal transport, the transverse magnetotransport properties of SRO ultrathin films are also strongly dependent on surface terminations. The  $\rho_{xy}$ - $H$  curves measured from the SrO- and  $RuO$ -terminated SRO films at 10 K are shown in **Figs. 4-3i-l**. The linear OHE components are subtracted from all the curves for clarity. For the as-grown sample (blue curve) with  $N_{Ru} = 6$  ( $t_{SRO} = 6.5$  u.c., SrO-terminated),  $\rho_{xy}$ - $H$  curves exhibit bulk-like AHE with negative  $R_S$ . As  $N_{Ru}$  decreases to 4, the sign of  $R_S$  changes from negative to positive. This sign reversal originates from a Fermi level ( $E_F$ ) shift with respect to the avoided band crossing points, which significantly affects the Berry curvature and thus the intrinsic AHE, which will be discussed in **Chapter 5**. As  $N_{Ru}$  decreases to 3,  $\rho_{xy}$  increases, and the coercive field decreases dramatically, implying further decay in electrical conductivity and ferromagnetism. After water-leaching, the  $R_S$  sign change occurs at  $N_{Ru} = 5$ .

Interestingly, the  $\rho_{xx}$ - $T$ ,  $M$ - $T$ , and  $\rho_{xy}$ - $H$  curves of the  $N_{\text{Ru}} = 3, 4$ , and 5 water-leached samples look surprisingly similar to their as-grown counterparts with  $N_{\text{Ru}} = 2, 3$  and 4 respectively. In other words, the physical properties of the  $N_{\text{Ru}}$  layered Water-leached samples are similar to  $N_{\text{Ru}}-1$  as-grown samples. To clarify the termination conversion-induced intriguing modulations in physical properties, we further investigated the evolutions of sheet resistivity ( $\rho_{\text{sheet}}$ ), sheet carrier density ( $n_{\text{sheet}}$ ),  $M$  (at 10 K), and  $T_c$  with  $t_{\text{SRO}}$ . As previously defined, for SrO-terminated (RuO<sub>2</sub>-terminated) samples, the nominal  $t_{\text{SRO}} = 3.5 \sim 6.5$  (3.0  $\sim$  6.0) u.c. As shown in **Figs. 4-4a-d**,  $t_{\text{SRO}}$ -dependent  $\rho_{\text{sheet}}$ ,  $n_{\text{sheet}}$ ,  $M$ , and  $T_c$  curves consistently exhibit a step-like feature. It is worth noting that both the metallicity and ferromagnetism of SRO are dominated by the RuO<sub>2</sub> atomic planes, which remain structurally intact during the surface termination conversion. Accordingly, the topmost SRO monolayer should not contribute to both electrical transport and ferromagnetism after water-leaching. In other words, as depicted in insets of **Figs. 4-4e, f**, even in an SRO film with robust bulk metallicity ( $N_{\text{Ru}} \geq 5$ ), the RuO<sub>2</sub>-terminated surface should become both insulating and non-ferromagnetic. Moreover, the consistent step-like features in **Figs. 4-4a-d** strongly suggest that the insulating non-ferromagnetic state is strictly confined within the topmost SRO monolayer; namely, the termination conversion triggers a surface MIT in SRO ultrathin films.

The surface MIT is further examined by scanning tunneling spectroscopy (STS) measurements. The differential tunneling conductance versus bias ( $dI/dV$ - $V$ ) curves on the SrO- and RuO<sub>2</sub>-terminated SRO surfaces are shown in **Fig. 4-4e** and **Fig. 4-4f**, respectively. Each curve was obtained by averaging over 14 curves measured on clean and flat regions

at 77 K. The  $dI/dV$  signal is proportional to the local density of states (DOS) at the

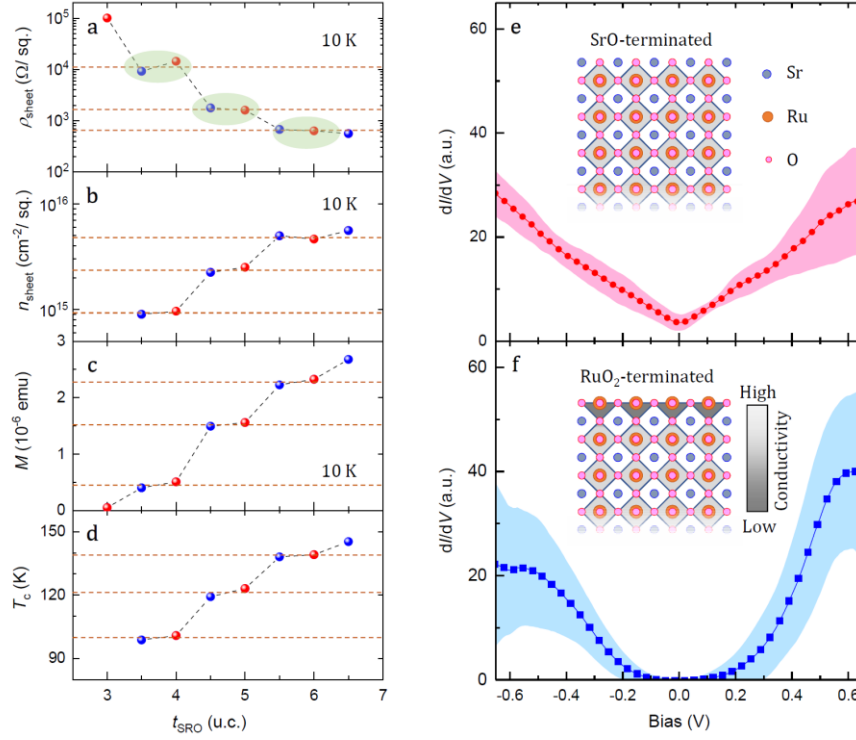


**Fig. 4-4** Evolution of electrical transport and magnetic properties with  $t_{\text{SRO}}$  and surface termination. **a-d.**  $t_{\text{SRO}}$ -dependent sheet resistivity ( $\rho_{\text{sheet}}$ ) (**a**), sheet carrier density ( $n_{\text{sheet}}$ ) (**b**), magnetization (**c**), and Curie temperature ( $T_c$ ) (**d**) of the SRO thin films. The  $\rho_{\text{sheet}}$ ,  $n_{\text{sheet}}$ , and  $M$  values were measured at 10 K. All curves exhibit a step-like feature, signifying that the metallicity and magnetism of RuO<sub>2</sub>-terminated samples consisting of  $N_{\text{Ru}}$  RuO<sub>2</sub> layers are similar to those of SrO-terminated samples consisting of  $N_{\text{Ru}}-1$  RuO<sub>2</sub> layers. **e-f.** Scanning tunneling spectroscopies of the SrO- (**e**) and RuO<sub>2</sub>- (**f**) terminated samples. The solid lines are bias-dependent differential conductance ( $dI/dV$ ) curves averaged from 14 curves measured at flat and clean surface regions. The colored backgrounds indicate the standard deviations. The insets of **e** and **f** are schematic atomic structures of SRO films with SrO- and RuO<sub>2</sub>-terminated surfaces, respectively. The electrical conductivity of the topmost SRO monolayer with RuO<sub>2</sub>-termination decays significantly. Adapted from H. G. Lee *et al* (2020) [27].

surface [18]. The  $dI/dV$ - $V$  curves of the SrO-terminated surface [Fig. 4-4e] exhibit typical metallic characteristics: finite DOS at zero-bias and gradually increased DOS with bias. These features are also consistent with a previous report on as-grown SRO surface [32]. In contrast, the  $dI/dV$ - $V$  curves of the RuO<sub>2</sub>-terminated surfaces [Fig. 4-4f] clearly shows a gap-like feature due to the negligible DOS near zero-bias. The average gap size is  $\sim 0.30$  eV. Note that the STS spectra of both SrO- and RuO<sub>2</sub>-terminated surfaces exhibit considerable spatial variations, which can be ascribed to surface adsorbates arising from the unavoidable *ex-situ* sample transfer procedure and water-leaching processes. In spite of this spatial variation, metallic (insulating) characteristics are consistently observed in all the  $dI/dV$ - $V$  curves from SrO-terminated (RuO<sub>2</sub>-terminated) surfaces. Therefore, the surface MIT by termination conversion in SRO thin film was observed.

Density functional theory calculation [33–35] explains the mechanism of surface MIT. The Ru<sup>4+</sup> cations inside the bulk SRO are under an octahedral crystal field. This crystal field splits Ru 4d orbitals into triple degenerate  $t_{2g}$  ( $d_{xy}$ ,  $d_{yz}$ , and  $d_{xz}$ ) orbitals and double degenerate  $e_g$  ( $d_{x^2-y^2}$  and  $d_{3z^2-r^2}$ ) orbitals. The calculated orbital-resolved DOS profiles projected along with a RuO<sub>2</sub> layer underneath the SrO layers are shown in Fig. 4-5a. Because of the high energy difference between the  $t_{2g}$  and  $e_g$  orbitals, the four Ru 4d electrons occupy  $t_{2g}$  orbitals only: three of them occupy the spin-majority channel and the remaining one occupies the minority channel, leading to a low spin configuration. Similar orbital occupancy can be found in the other RuO<sub>2</sub> layers underneath the surface layer and the ones in SrO-terminated SRO film.



In contrast, the  $\text{Ru}^{4+}$  cations at the  $\text{RuO}_2$ -terminated surface layer are under a unique square pyramidal crystal field. This crystal field with lower symmetry further degenerates the  $t_{2g}$  and  $e_g$  orbitals. The orbital-resolved DOS profiles projected along the  $\text{RuO}_2$  surface

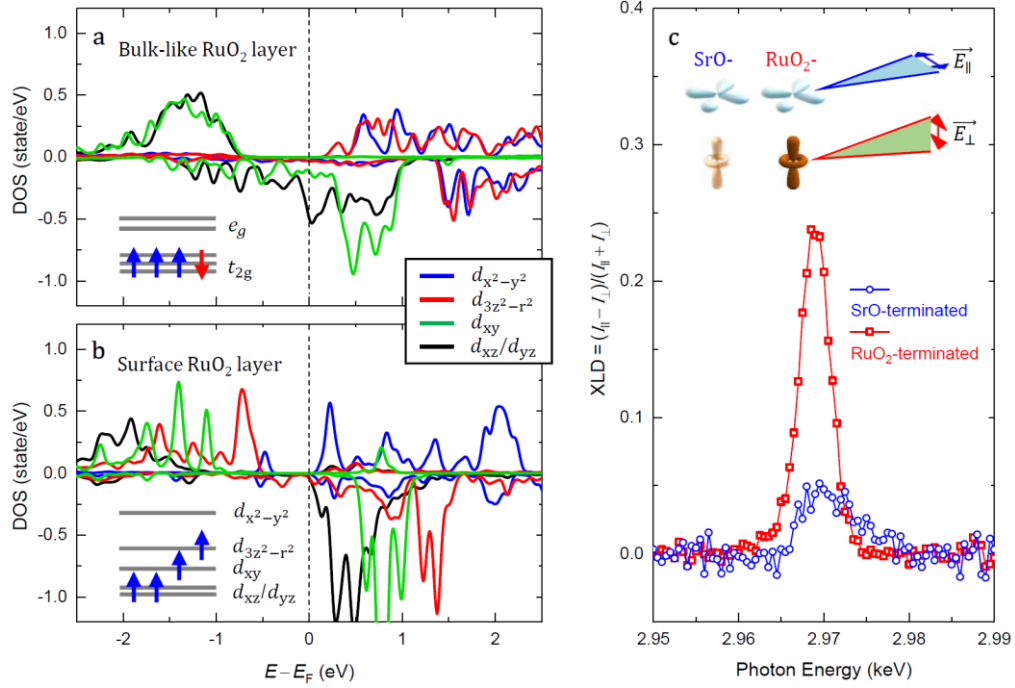


**Fig. 4-5** Electronic structure and 4d orbital occupancy in SRO ultrathin film. **a.** Orbital-resolved DOS projected along with the  $\text{RuO}_2$  layer underneath the SrO layer. **b.** Orbital-resolved DOS projected along with the  $\text{RuO}_2$ -terminated surface layer. The gap size is  $\sim 0.25$  eV. Insets of (a) and (b) illustrate the low-spin and high-spin configurations in the bulk-like and surface  $\text{RuO}_2$  layers, respectively. **c.** X-ray linear dichroism (XLD) at the Ru  $L_2$  edge measured from the SrO- and  $\text{RuO}_2$ -terminated SRO films ( $N_{\text{Ru}} = 5$ ).  $I_{\parallel}$  and  $I_{\perp}$  are X-ray absorption spectroscopy intensities with linear light polarization parallel ( $E_{\parallel}$ ) and perpendicular ( $E_{\perp}$ ) to the (001) surface. The schematic inset shows how the  $d_{x^2-y^2}$  (top) and  $d_{3z^2-r^2}$  (bottom) orbitals couple with the incident linear-polarized X-ray. The light-color (deep-color) indicates the unoccupied (occupied) orbitals. Adapted from H. G. Lee *et al* (2020) [27].

layer are shown in **Fig. 4-5b**. The  $d_{3z^2-r^2}$  orbital states shift downward dramatically below  $E_F$ , thus leading to the gap opening. The gap size is  $\sim 0.25$  eV, close to the one derived from the STS measurement. Moreover, the four Ru 4d electrons occupy three  $t_{2g}$  orbitals as well as one  $e_g$  ( $d_{3z^2-r^2}$ ) orbital in the spin majority channel, leading to a high spin configuration. We also tested several possible magnetic orderings in the RuO<sub>2</sub>-terminated SRO film and found the energetically favorable magnetic ground state is bulk ferromagnetic with surface G-type antiferromagnetic. This spin configuration is  $\sim 60$  meV lower in energy compared to the pure ferromagnetic configuration. Therefore, the surface MIT and non-ferromagnetic transition can be explained by termination dependent orbital occupancy, theoretically.

To experimentally verify the termination-dependent orbital occupancy scenario, X-ray linear dichroism (XLD) measurement was conducted. We performed X-ray absorption spectroscopy (XAS) measurements on the SrO- and RuO<sub>2</sub>-terminated SRO films ( $N_{Ru} = 5$ ) at the Ru  $L_2$ -edge with the linear light polarization perpendicular ( $E_{\perp}$ ) and parallel ( $E_{\parallel}$ ) to the film surface. The corresponding XAS intensities  $I_{\perp}$  and  $I_{\parallel}$  are dominated by the unoccupied  $d_{3z^2-r^2}$  and  $d_{x^2-y^2}$  orbitals, respectively [36,37]. The XLD is calculated as the normalized XAS intensity difference  $(I_{\perp} - I_{\parallel})/(I_{\perp} + I_{\parallel})$ . As shown in **Fig. 4-5c**, the RuO<sub>2</sub>-terminated SRO film shows a positive XLD peak, signifying a preferential electron occupation in the  $d_{3z^2-r^2}$  orbital. By contrast, the SrO-terminated SRO films show a much weaker XLD peak. Since both  $e_g$  orbitals are unoccupied, this weak XLD signal may come from compressive strain induce slight preferential electron occupancies in  $d_{xz}$  and  $d_{yz}$  orbitals. The consistency between DFT and XLD results confirms that the surface termination-dependent orbital occupancy and associated modulations in

electronic/magnetic structures can comprehensively explain the surface MIT in ultra-thin SRO films [38].

#### **4.4 Conclusion**

RuO<sub>2</sub> surface terminated SRO thin film was realized for the first time. An *ex-situ* water-leaching recipe was developed to achieve an effective and uniform surface termination engineering in SRO. As the surface termination converts from SrO to RuO<sub>2</sub>, the topmost SRO monolayer undergoes an MIT while the underneath layers remain metallic. This surface MIT can be fully understood by the surface symmetry breaking-induced changes in 4*d* orbital occupancy and electronic/magnetic structures.

The water-leaching recipe for surface termination engineering can be easily generalized to other TMO-based epitaxial systems. In addition, the water-leaching-induced termination conversion is also technically essential for SRO-related research. The SRO surface termination conversion occurs even with a very short-duration water-leaching (~30 s). Therefore, it could occur during water-solution-based nano-fabrication procedures or even simple storage in a humid atmosphere. An unexpected surface termination conversion of this type could cause considerable changes in the magnetism and electrical transport of SRO ultrathin films. On this basis, we suggest that the differences and non-uniformity of surface termination could be an important factor to cause a large deviation on the previously reported electric/magnetic critical thickness values in SRO ultrathin films [10–13]. Besides, for investigating the electrocatalytic activity of SRO [39], the stability of surface termination in water-based solutions should also be seriously considered.

---

# Chapter 5

## Results and Discussion III: Capping Layer

*An expert is a person who has made all the mistakes  
that can be made in a very narrow field.*

- Niels Bohr -

### 5.1 Introduction: Anomalous Hall effect of SrRuO<sub>3</sub>

#### 5.1.1 ‘Intrinsic’ anomalous Hall effect

When there is a broken time-reversal symmetry, the anomalous Hall effect (AHE) arises [1]. It can be distinguished with the ordinary Hall effect, which is linearly dependent on the external field and inverse of carrier density. Conventionally, it has been explained with a spin-dependent scattering of the itinerant electrons due to the spontaneous magnetization or magnetic impurities inside the materials (*e.g.* ferromagnet). Therefore, the Hall effect can be described as below in the empirical and conventional picture.

$$\rho_{xy} = R_0 H + R_{AHE} M.$$

$H$  and  $M$  are the external field and the magnetization of the sample, respectively.  $R_0$  is the ordinary Hall coefficient inverse proportional to the carrier density.  $R_{AHE}$  is the anomalous Hall coefficient, thus the second term describes AHE as below.

$$\rho_{AHE} = \rho_{xy} - R_0 H = R_{AHE} M.$$

However, the conventional picture cannot explain the AHE in the case of zero-magnetization such as all-in-all-out spin texture and negative AHE. Recently, the AHE is understood in terms of the geometric concepts of Berry curvature in momentum space [1–3]. The free-electron under the electric field does not have any velocity component perpendicular to the electric field. However, with periodic lattice potential, it could have a perpendicular component. In Karplus-Luttinger theory (1954), the electron in solid acquires an additional component to their group velocity as below.

$$\mathbf{v}_{group} = \frac{1}{\hbar} \frac{\partial \mathbf{E}}{\partial \mathbf{K}} + \frac{e}{\hbar} \mathbf{E} \times \mathbf{\Omega}_n .$$

In the second term,  $\mathbf{\Omega}_n$  is the berry curvature which gives additional velocity perpendicular to the electric field  $\mathbf{E}$ , thus it contributes to the Hall effect. With this concept, the sum of  $\mathbf{E} \times \mathbf{\Omega}_n$  over all occupied band gives AHE. In the trivial case, due to their symmetric (trivial) band structure near the Fermi surface, the sum is zero. However, in a ferromagnet with the broken time-reversal symmetry, the sum can be non-zero, thus it has AHE. This phenomenon is called ‘intrinsic AHE’ due to its Berry curvature-related origin.

### 5.1.2 Origin of anomalous Hall effect in SrRuO<sub>3</sub>

The intrinsic Berry curvature-related picture has been adopted to explain the AHE of SrRuO<sub>3</sub> (SRO). As briefly shown in **Chapter 4**, the magnitude and even the sign of AHE are dependent on doping, temperature, and film thickness of SRO [2,4–6]. The sign flipping cannot be explained by conventional  $R_{AHE}M$  picture. Hence the intrinsic  $\mathbf{E} \times \boldsymbol{\Omega}_n$  term should be considered to understand the AHE of SRO. The broken time-reversal symmetry, strong correlation, and spin-orbit coupling of SRO induce non-trivial band crossing points, which give non-trivial Berry curvature. The change of magnetization affects the splitting of the band, thus varies the position of the band crossing points. Therefore, the sum of Berry curvature along the Fermi surface in SRO is closely related to the magnetization and the

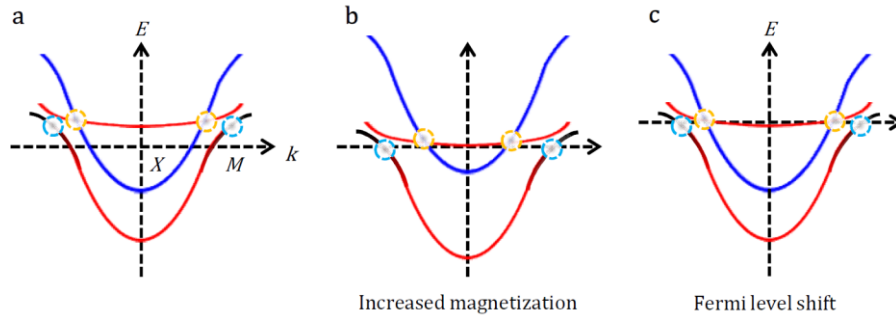


**Fig. 5-1** **a.** Schematic band diagram of the SRO thin film. Different color of the curves denotes spin-majority and minority bands. Each circle is the band crossing points, which gives non-zero Berry curvature. **b.** Band shift from the magnetization changes. The gap between spin-majority and minority bands become larger with increasing magnetization. Positions of crossing points are also shifting. **c.** Band shift with respect to the Fermi level

Fermi level, resulting in modulation of AHE [2,7].

### 5.1.3 Recent controversies related to topological Hall effect

Recently, there have been extensive controversies on SRO ultra-thin films after the discovery of the topological Hall effect (THE) in this material [8]. THE of SRO ultra-thin film is thought to be originated from the magnetic Skyrmion, which is the swirling arrangement of spins in real space [Fig. 5-2a]. This extraordinary spin texture comes from the antisymmetric exchange interaction (Dzialoszyński-Moriya interaction; DMI). The strong spin-orbit coupling and the inversion symmetry breaking are the key factors for the DMI. If we wrap the unit sphere with the individual spin of Skyrmion, the solid angle from the spins can be defined as below.

$$\Omega_s = \oint \mathbf{n} \cdot (\partial_x \mathbf{n} \times \partial_y \mathbf{n}) dx dy .$$

The electron moving near this spin texture should feel the effective magnetic field due to the gauge invariance, which contains the concept of topological charge  $Q$  and vector gauge potential  $\mathbf{A}$ . Therefore, the solid angle from the magnetic Skyrmion contributes Hall effect, *i.e.* THE.

$$\mathbf{B}_z = \nabla \times \mathbf{A} = \frac{\hbar c}{2e} \cdot (\partial_x \mathbf{n} \times \partial_y \mathbf{n})$$

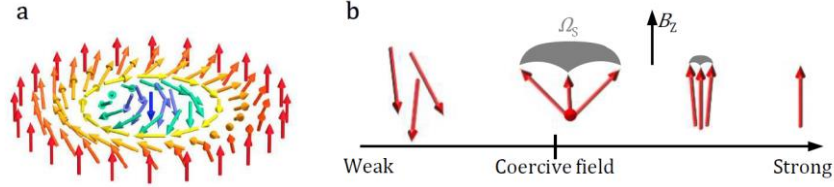


**Fig. 5-2 a.** Schematic illustration of the magnetic Skyrmion (Bloch type). Arrows denote the direction of spins. **b.** Evolution of solid angle with varying the external magnetic field. The solid angle of spin emerges at the sudden magnitude of the field with the Dzialoszynski-Moriya interaction. When the external field keeps increasing, the solid angle is suppressed due to the spin alignment.

THE of material is characterized by the ‘hump’ signal of the Hall resistivity. With the high external field, all spins in the material are aligned resulting in the zero-solid angle of spin texture. Near the zero-external field, all spins are paramagnetically distributed, thus also cannot have a finite solid angle. With the intermediate field, the solid angle of magnetic Skyrmion starts to have a finite value which gives a sudden deviation of Hall resistivity [Fig. 5-2b].

The number of reports regarding the hump signal in SRO ultra-thin films and associated heterostructure is skyrocketing recently. Some studies explain it using the concept of magnetic Skyrmion and related THE [Fig. 5-3a] [8–10]. They claim that the enhancement of the inversion symmetry breaking, or spin-orbit coupling, or both induce DMI to generate Skyrmion texture and result in THE. The others explain the hump signal by using the concept of two-channel AHE [11–19]. As shown in Fig. 5-3b, merging the two AHE curves



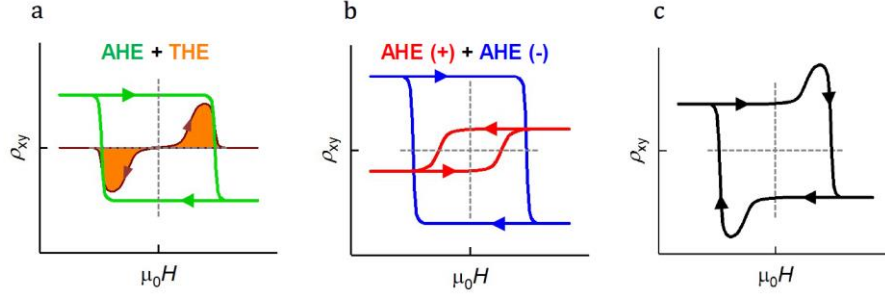


**Fig. 5-3** **a.** The AHE curve of 5 u.c. SRO film (green) and the THE curve from the possible magnetic Skyrmion (orange). **b.** AHE curves which have an opposite sign with each other. The positive (red) AHE comes from the 4 u.c. SRO film while the negative (blue) AHE curve comes from the 5 u.c. SRO film. **c.** The resultant AHE curve with the hump structure comes from either **a** or **b**. Adapted from [L. Wang \*et al\* \(2020\)](#) [19].

with opposite signs and different coercive fields gives a hump structure. However, the existence of two different components of AHE requires inhomogeneity of the SRO ultra-thin film. Therefore, a proper explanation for the inhomogeneity providing opposite Berry curvature is required.

## 5.2 Tunable inhomogeneity induced by the capping layer

Various physical conditions induce inhomogeneity during film growth. Since diverse growth parameters are entangled with each other complicatedly, the systematic control of inhomogeneity in the thin film is still in a haze. One outstanding approach to this topic was done by Wang *et al.* (2020) [19]. In this research, they controlled the thickness of SRO film fractionally using the step-flow growth dynamics of SRO thin film. The one-layer growth

of SRO starts from the step-edge and ends with covering all terrace areas, *i.e.* step-flow growth mode. This growth mode makes fractional thickness possible if we stop the growth before the newly growing layer covers the whole surface. For instance, if we grow the 4 u.c. of SRO and continue the growth but stop before it forms the fifth unit cell, the film has a fractional thickness between 4 and 5 integer unit cells. Therefore, the film has a thickness inhomogeneity of distinguishable 4 and 5 u.c. region. Since each component has a different sign of AHE, the resultant Hall effect shows a hump signal from the inhomogeneity. After this study, plenty of similar two-channel AHE has been reported even with the heterostructured-SRO, despite the lack of the explanation for the origin of inhomogeneity and how it acts to AHE.

In this paper, we addressed the systematic control of inhomogeneity by using the  $\text{LaAlO}_3$  (LAO) capping layer. We grew SRO thin films on the  $\text{SrTiO}_3(001)$ ; STO) substrate using the pulsed laser deposition (PLD) technique [Fig. 5-4a]. The thickness of SRO films is precisely fixed as 5 u.c., using the reflection high-energy electron diffraction (RHEED) to avoid any artifacts from the thickness inhomogeneity. On the 5 u.c.-SRO thin film, the LAO capping layer was deposited [Fig. 5-4c]. We varied the growth pressure for LAO capping layers as a manipulated variable, while all other PLD parameters are controlled. The surface of the film was sharp regardless of the existence of the capping layer [Fig. 5-4b, d]. Note that the growth conditions for the SRO layer are the same for all samples. We

performed transverse magnetotransport of SRO heterostructures with a  $50 \times 50 \mu\text{m}$  Hall bar to obtain  $\rho_{\text{AHE}}-H$  behavior. Intriguingly, the  $\rho_{\text{AHE}}-H$  of SRO films are seriously affected, nonetheless only the growth pressure of the LAO layer is varied. As shown in **Fig. 5-4e-h**,  $\rho_{\text{AHE}}-H$  curves of SRO films were dramatically changed. For comparison,  $\rho_{\text{AHE}}-H$  curves of

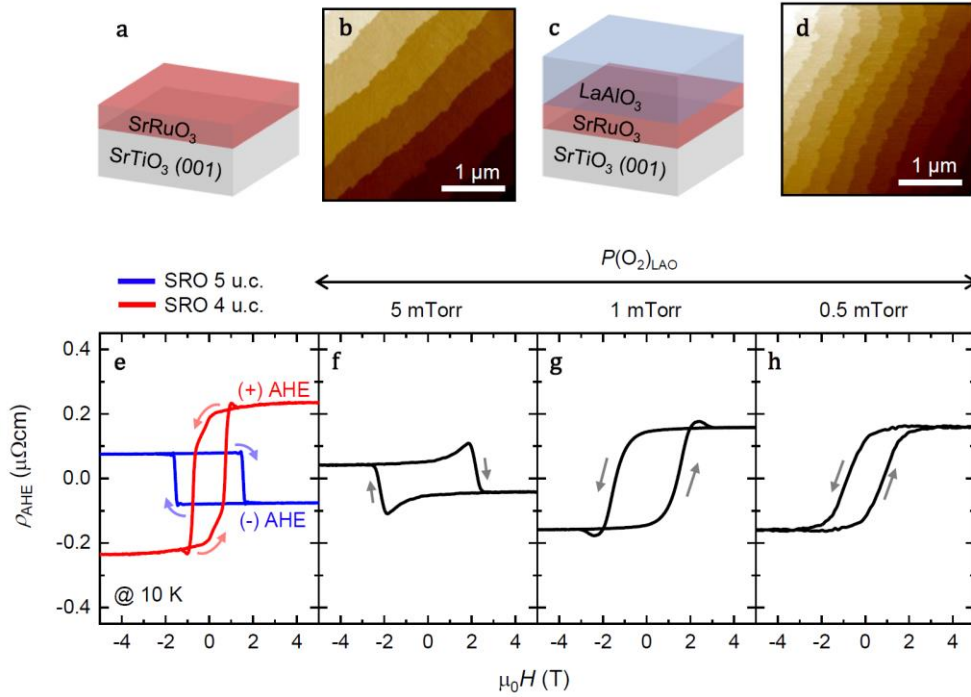


**Fig. 5-4** **a (c).** Schematic sample structure of 5-unit-cell (u.c.)  $\text{SrRuO}_3$  (SRO) films grown on the  $\text{SrTiO}_3(001)$  (STO) substrate without (with) 10 u.c. of  $\text{LaAlO}_3$  (LAO) capping layer. **b (d).** Surface topographic images of **a (c)**, respectively, obtained by atomic force microscope. **e.** Anomalous Hall resistivity-magnetic field ( $\rho_{\text{AHE}}-H$ ) curves of 5 and 4 u.c.-SRO films without capping layer measured at 10K. All the linear terms from the ordinary Hall effect were subtracted. Arrows denote field sweep direction. **f-h.**  $\rho_{\text{AHE}}-H$  curves of LAO capped SRO films. The growth condition and thickness of SRO layers were fixed while the growth pressure of the LAO layer was varied from 5mTorr to 0.5mTorr.

5 and 4 u.c.-SRO films without capping layers are depicted [Fig. 5-4e]. With 5mTorr of growth pressure for the LAO layer ( $P_{\text{LAO}}$ ), the hump structure in the  $\rho_{\text{AHE}}-H$  curve arises [Fig. 5-4f]. With decreasing the  $P_{\text{LAO}}$ , the sign of AHE starts to flip [Fig. 5-4g]. The sign of AHE is totally flipped and the hump structure vanishes with the lowest growth pressure [Fig. 5-4h]. Notably, the hump signal occurs while the sign of AHE is flipping, implying that the origin might be two-channel AHE rather than THE.

In order to further examine the possibility of two-channel AHE, we measured the temperature dependence of magnetization ( $M-T$ ) of each sample. Fig. 5-5 shows  $M-T$  curves and the first derivatives of them. The  $T_C$  of 5 and 4 u.c.-SRO film without LAO capping layer was  $\sim 115$  K and  $\sim 90$  K [Fig. 5-5a, e]. Note that we define the  $T_C$  as onset values, thus they are at the beginning of the peaks in their first derivatives. With the LAO capping layer [Fig. 5-5b-d, f-h], some SRO films show kinks in their  $M-T$  curves and two-peaks in first derivatives. The existence of distinguishable  $T_C$  implies the inhomogeneity of the LAO-capped SRO. At the 5mTorr and 1mTorr of  $P_{\text{LAO}}$ ,  $\sim 90$  K of  $T_C$  emerges while it still shows  $\sim 115$  K  $T_C$  at the same time. By lowering the  $P_{\text{LAO}}$  down to 0.5mTorr, the  $\sim 115$  K of  $T_C$  vanished and  $\sim 90$  K of  $T_C$  only remains. The distinguishable phases can be extracted by fitting the  $M-T$  curves using different  $T_C$ . Below is the empirical  $M-T$  function used for the fitting.

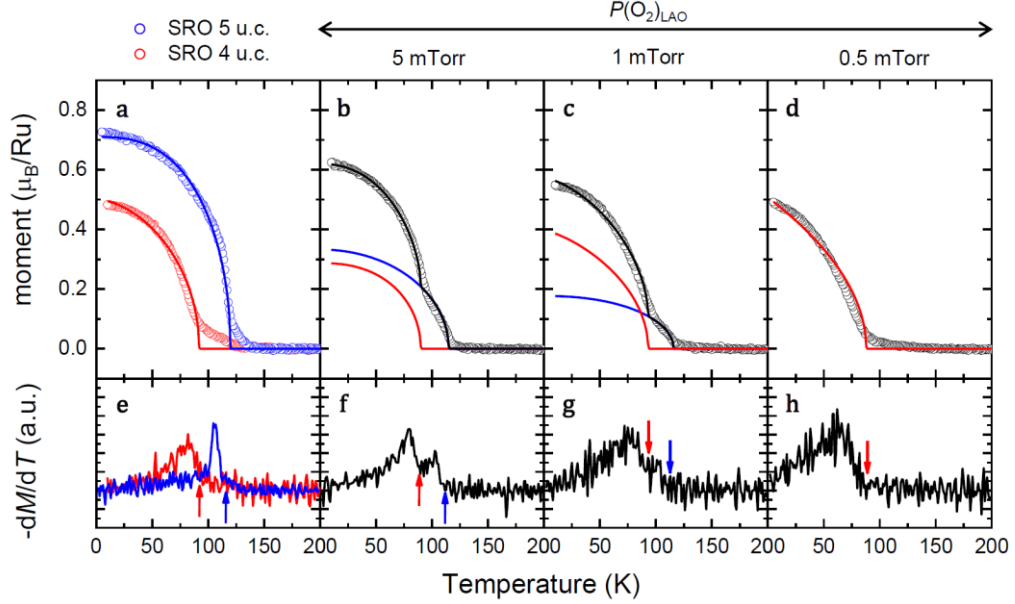


**Fig. 5-5 a.** Magnetization-temperature ( $M$ - $T$ ) curves of 5 and 4 u.c.-SRO films without capping layers. Open circles are experimental data and solid lines are fitting curves. **b-d.**  $M$ - $T$  curves of LAO capped SRO films. The growth condition and thickness of SRO layers were fixed while the growth pressure of the LAO layer was varied from 5mTorr to 0.5mTorr. The blue (red) fitting curve of LAO capped SRO film shows Curie temperature ( $T_C$ ) of  $\sim 115\text{K}$  ( $\sim 90\text{K}$ ), similar to that of 5 (4) u.c.-SRO film without LAO capping layer. **e-h.** first derivatives of a-d. Arrows denote  $T_C$ . Since the  $T_C$  of empirical fitting function is onset value, there are  $\sim 10\text{K}$  of difference between peak position in first derivatives and  $T_C$ .

$$M(T) = M(0) \cdot (1 - (T/T_C)^\alpha)^\beta$$

For convenience, let us call different phases with their  $T_C$ . The contribution of 90K phases is kept increasing with lowering the  $P_{\text{LAO}}$ , while the contribution of 115K phase is decreasing, and completely vanishes at the lowest pressure. Comparing the fitted  $M$ - $T$  curves with Hall curves in **Fig. 5-4e-h**, we found a striking one-to-one matching tendency.

If there is a hump in AHE, there is always the co-existence of 90K and 115K phases. If there is only 115K phase, the AHE shows a negative sign. Similarly, if there is only 90K phase, the AHE shows a positive sign without any hump signal. Intriguingly, the 115K and 90K curves look similar to those of 5 and 4 u.c.-SRO single-layered samples. Therefore, it is a high possibility that the hump signal in these heterostructures comes from the hidden inhomogeneity which gives two-channel AHE, even the thickness of the SRO layer was precisely fixed as 5 u.c.

Based on the hidden inhomogeneity hypothesis, we compared LAO-capped SRO film and SRO film without capping layer. To investigate their behaviors, we fitted  $\rho_{\text{AHE}}-H$  curves

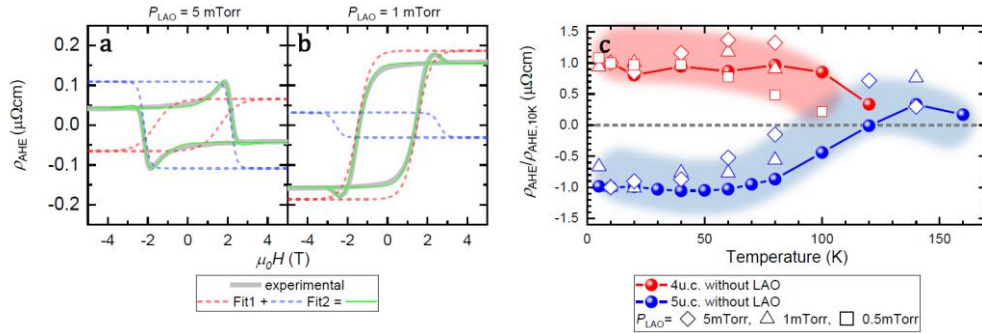


**Fig. 5-6 a, b.** Fitted  $\rho_{\text{AHE}}-H$  curves of LAO capped SRO samples with growth pressure for LAO layer of 5 and 1 mTorr. Gray lines are experimental curves and red and blue curves are negative and positive fitting curves. Green lines are summations of fitting curves. **c.** Temperature dependence of normalized  $\rho_{\text{AHE}}$  values extracted from the fitting. The closed circles come from 4 and 5 u.c. SRO films without the LAO capping layer. The open symbols are LAO capped SRO. The red (blue) denotes the negative (positive) component from the fitting.

with two different empirical curves [Figure 5-6a, b]. The used function was hyperbolic tangent which has amplitude, broadening, and coercive field as fitting parameters. Since we measured  $\rho_{\text{AHE}}-H$  with varying the temperature, we could extract the temperature dependence of each component of  $\rho_{\text{AHE}}$ , saturated at 5T of the external field [Figure 5-6c]. To compare each component with bare 4 and 5 u.c. SRO films, we normalized each component with the value at 10K. At low temperatures, LAO capped SRO samples show both negative and positive  $\rho_{\text{AHE}}$  components. The positive components (red) keep their sign until they vanish near 90K. The negative components (blue) become positive as increasing the temperature and vanish near 115K. Comparing them with bare 4 and 5 u.c. samples, the positive and negative  $\rho_{\text{AHE}}$  components exhibit similar temperature dependence. Therefore, the similarity of AHE variation of LAO-capped SRO film and SRO film without capping layer implies the hidden inhomogeneity of LAO-capped SRO, which induces 4-u.c.-like behavior.

If so, how does the LAO capping layer induce the inhomogeneity into the SRO films? First, the oxygen vacancy ( $V_{\text{O}}$ ) might affect the structure or the polarity of the LAO layer [20–24]. The lower the oxygen partial pressure, the more  $V_{\text{O}}$  might be induced into the LAO capping layer. In order to examine this hypothesis, we performed a control experiment with Ar gas. If the  $V_{\text{O}}$  formation is a crucial factor, the  $\rho_{\text{AHE}}-H$  of a film should be affected by only the oxygen partial pressure, not the total pressure ( $P_{\text{Total}}$ ) from the Ar

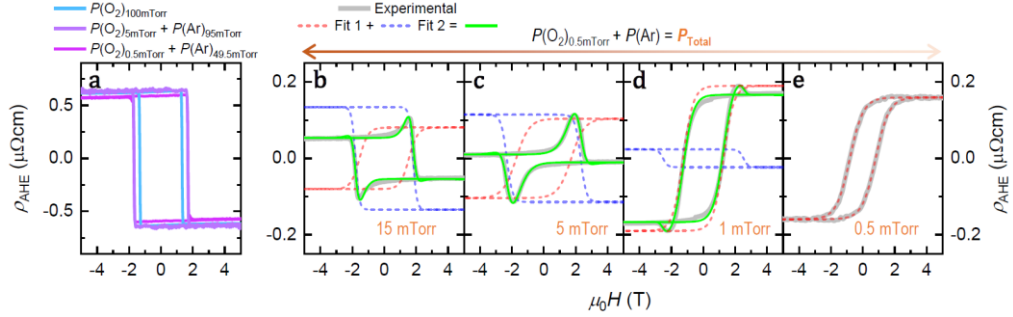


**Fig. 5-7** A control experiment with total pressure variation during the growth of the LAO capping layer. **a.**  $\rho_{\text{AHE}}-H$  curves of LAO/SRO heterostructure grown at relatively high pressure. The total pressures ( $P_{\text{Total}}$ ) are 100 and 50 mTorr, while the partial pressures of Ar and O<sub>2</sub> are varied. **b-e.**  $\rho_{\text{AHE}}-H$  curves with varying the  $P_{\text{Total}}$  from 15 mTorr to 0.5 mTorr. The O<sub>2</sub> partial pressure is fixed as 0.5 mTorr, while Ar partial pressure is only varied. Gray lines are experimental curves and red and blue curves are negative and positive fitting curves. Green lines are summations of fitting curves.

gas. As shown in **Fig. 5-7a**, we capped the LAO layer with the relatively high-pressure condition. Even we changed oxygen partial pressure, the AHE of SRO film is not affected by high-pressure growth conditions. We also varied  $P_{\text{Total}}$  with varying the Ar partial pressure, while O<sub>2</sub> partial pressure is fixed [**Fig. 5-7b-e**]. The experimental  $\rho_{\text{AHE}}-H$  curves are fitted with negative (blue) and positive (red) components. As  $P_{\text{Total}}$  decreases, the negative component is decreasing while the positive component is increasing. In other words, the  $\rho_{\text{AHE}}-H$  of the film only reacts with  $P_{\text{Total}}$ , regardless of oxygen partial pressure. Therefore, the V<sub>O</sub> formation cannot be an explanation, but the kinetic mechanism seems to be crucial for these heterostructures.

When we fabricate the heterostructure, the intermixing of cations in each layer should



be considered [25,26]. Since the growth process of PLD is highly kinetic, the transferred cation can be mixed easily with the underneath layer [Fig. 5-8]. The kinetic energy of transferred cation is inverse proportional to the pressure due to velocity loss from the scattering during the transfer. Therefore, the intermixing should be serious in low-pressure growth conditions [27–29]. With this aspect, the  $M$ - $T$  and AHE dependence of LAO growth pressure can be well explained. Note that the 5 u.c. and 4 u.c. bare SRO film has a  $T_C$  of  $\sim 120$  K and  $\sim 90$  K, with negative and positive signs of AHE, respectively. The intermixing

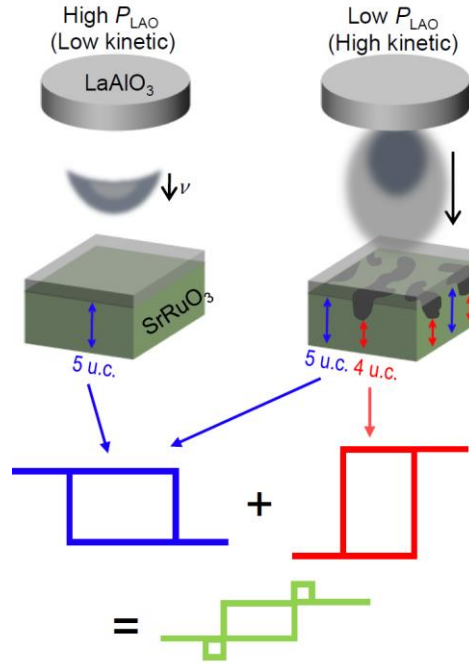


**Fig. 5-8** Schematics of the kinetic process during the growth of the LAO capping layer on the SRO films. At high-pressure conditions, the kinetic energy of evaporated plume is suppressed, while low-pressure conditions degraded SRO films with high kinetic energy. The degraded regions in SRO film exhibit 4 u.c.-like behavior resulting hump signal in the  $\rho_{\text{AHE}}-H$  curve.

of Al cation in LAO into Ru cation in the SRO layer can decrease the effective thickness of SRO film. If this intermixing is not uniform, it could give inhomogeneity of SRO film, thus it would provide distinguishable  $T_C$  and the hump in AHE.

### **5.3 Conclusion**

The systematic control of inhomogeneity and associated AHE in SRO thin films is achieved by using the LAO capping layer. The growth pressure of the LAO capping layer is a crucial parameter for the phase separation, which affects its AHE mixing. The different phases can be distinguished by measuring the temperature-dependent magnetization since each phase has an intrinsic critical temperature of ferromagnetism. The origin of this inhomogeneity is highly likely to be the intermixing from the LAO capping layer due to its total pressure dependence. Further analysis with a scanning transmission electron microscope and magnetic force microscope will clarify the effect of intermixing from the capping layer. Our findings also provide a proper explanation for hump signal in AHE of SRO heterostructure and a caution for the capping layer engineering.

---

# Chapter 6

## Summary and Concluding Remarks

*The present is theirs; the future, for which I really worked, is mine.*

- Nikola Tesla –

In the introduction of this dissertation, we figured the question of “**what is important for the interfacial engineering of perovskite oxides and how to control it**”. Three topics regarding interfacial engineering of perovskite oxides were discussed. The buffer layer, surface, and capping layer are important factors, which give significant property changes in the thin film from the bulk.

The buffer layer technique has been used to accommodate the large lattice mismatch from the substrate and provide a commensurate lattice for strain engineering. However, if the mismatch is too large, the single-layer buffer cannot accommodate misfit dislocations resulting in low crystallinity. To grow perovskite oxide such as  $\text{BaBiO}_3$  ( $a = 4.374 \text{ \AA}$ ), conventional substrates and single buffer layers are improper. With a  $\text{BaZrO}_3/\text{BaCeO}_3$  bilayer buffer template, we could realize fully-commensurate epitaxial  $\text{BaBiO}_3$  film for the first time. Using this system, the fundamental limit of the octahedral breathing distortion of  $\text{BaBiO}_3$  film was revealed as a 6 u.c. due to the anisotropic suppression of oxygen expand-shrinking modes.

Surface termination of the film is also known to be an important parameter in the aspect of the alternating polar nature of some perovskite oxides such as  $\text{LaNiO}_3$ . However, even

without the alternating polar layers, we found that breaking of the octahedral crystal field can be induced from the termination conversion. As a prominent example, we convert the surface termination of  $\text{SrRuO}_3$  films from  $\text{SrO}$  to  $\text{RuO}_2$ . The as-grown  $\text{SrRuO}_3$  films always exhibit  $\text{SrO}$  termination, nevertheless, we overcame this nature with a water-leaching technique. As the surface termination converts from  $\text{SrO}$  to  $\text{RuO}_2$ , the topmost  $\text{RuO}_2$  monolayer becomes insulating while the underneath layers remain metallic. The surface symmetry breaking induces the change of  $4d$  orbital occupancy and results in surface metal-insulator transition.

The capping layer technique is one of the bases for heterostructure engineering. The effect from the capping layer should be considered seriously in not only the aspect of structure and electronic coupling but also the aspect of the source of inhomogeneity. The  $\text{SrRuO}_3/\text{LaAlO}_3$  heterostructure was investigated for the capping layer-induced inhomogeneity. With the high kinetics of the pulsed laser deposition process, the growth pressure of the  $\text{LaAlO}_3$  capping layer affects non-uniform intermixing. This inhomogeneity provides the variation of effective thickness and resulting in the mixing of the two-channel anomalous Hall effect, which mimics the topological Hall effect from the magnetic Skyrmion.

In sum, all these processes during the growth of oxide heterostructure; selection of substrate, commensurate buffer layer, *ex-situ* conditions for surface treatment condition, and growth kinetics of capping layer; should be precisely examined to avoid misunderstanding the measured functionalities of perovskite oxides.

---

# Bibliography

*In Science, it is when we take some interest in the great discoverers and their lives that it becomes endurable, and only when we begin to trace the development of ideas that it becomes fascinating.*

- James Clerk Maxwell -

This thesis is mainly based on “*Double layer Buffer Template to Grow Commensurate Epitaxial BaBiO<sub>3</sub> Thin Films*” by H. G. Lee *et al.*, APL Materials **4**, 126106 (2016)., “*Anisotropic Suppression of Breathing Distortion with Fully-strained BaBiO<sub>3</sub> Heterointerface*” by H. G. Lee *et al.*, APL Materials **6**, 016107 (2018)., and “*Atomic-scale Metal-Insulator Transition in SrRuO<sub>3</sub> Ultrathin Films Triggered by Surface Termination Conversion*” by H. G. Lee *et al.*, Advanced Materials **32**, 1905815 (2020).

## References for Chapter 1

- [1] N. A. Spaldin and R. Ramesh, *Advances in Magnetoelectric Multiferroics*, Nature Materials **18**, 203 (2019).
- [2] A. Ohtomo and H. Y. Hwang, *A High-Mobility Electron Gas at the LaAlO<sub>3</sub>/SrTiO<sub>3</sub> Heterointerface*, Nature **427**, 423 (2004).
- [3] H. Sato and M. Naito, *Increase in the Superconducting Transition Temperature by Anisotropic Strain Effect in (001) La<sub>1.85</sub>Sr<sub>0.15</sub>CuO<sub>4</sub> Thin Films on LaSrAlO<sub>4</sub> Substrates*, Physica C **274**, 221 (1997).
- [4] A. V. Ushakov, S. V. Streltsov, and D. I. Khomskii, *Crystal Field Splitting in Correlated Systems with Negative Charge-Transfer Gap.*, Journal of Physics: Condensed Matter **23**, 445601 (2011).

- [5] J. M. Rondinelli, S. J. May, and J. W. Freeland, *Control of Octahedral Connectivity in Perovskite Oxide Heterostructures: An Emerging Route to Multifunctional Materials Discovery*, MRS Bulletin **37**, 261 (2012).
- [6] J. Zaanen, G. A. Sawatzky, and J. W. Allen, *Band Gaps and Electronic Structure of Transition-Metal Compounds*, Physical Review Letters **55**, 418 (1985).
- [7] K. Foyevtsova and G. A. Sawatzky, *A Band Theory Perspective on Molecular Orbitals in Complex Oxides*, Journal of Modern Physics **10**, 953 (2019).
- [8] J. M. Rondinelli and C. J. Fennie, *Octahedral Rotation-Induced Ferroelectricity in Cation Ordered Perovskites*, Advanced Materials **24**, 1961 (2012).
- [9] J. M. Rondinelli and N. A. Spaldin, *Substrate Coherency Driven Octahedral Rotations in Perovskite Oxide Films*, Physical Review B **82**, 113402 (2010).
- [10] P. V. Balachandran and J. M. Rondinelli, *Interplay of Octahedral Rotations and Breathing Distortions in Charge-Ordering Perovskite Oxides*, Physical Review B **88**, 054101 (2013).
- [11] Y. J. Chang, C. H. Kim, S. H. Phark, Y. S. Kim, J. Yu, and T. W. Noh, *Fundamental Thickness Limit of Itinerant Ferromagnetic SrRuO<sub>3</sub> Thin Films*, Physical Review Letters **103**, 057201 (2009).
- [12] D. G. Schlom, L. Q. Chen, X. Pan, A. Schmehl, and M. A. Zurbuchen, *A Thin Film Approach to Engineering Functionality into Oxides*, Journal of the American Ceramic Society **91**, 2429 (2008).
- [13] D. G. Schlom, L.-Q. Chen, C. J. Fennie, V. Gopalan, D. A. Muller, X. Pan, R. Ramesh, and R. Uecker, *Elastic Strain Engineering of Ferroic Oxides*, MRS Bulletin **39**, 118 (2014).
- [14] P. D. C. King, H. I. Wei, Y. F. Nie, M. Uchida, C. Adamo, S. Zhu, X. He, I. Božović, D. G. Schlom, and K. M. Shen, *Atomic-Scale Control of Competing Electronic Phases in Ultrathin LaNiO<sub>3</sub>*, Nature Nanotechnology **9**, 443 (2014).

## References for Chapter 2

- [1] G. K. Hubler, *Pulsed Laser Deposition*, MRS Bulletin **17**, 26 (1992).
- [2] B. M. Clemens and J. A. Bain, *Stress Determination in Textured Thin Films Using X-Ray Diffraction*, MRS Bulletin **17**, 46 (1992).
- [3] E. Chason, T. M. Mayer, and M. Mayer, *Thin Film and Surface Characterization by Specular X-Ray Reflectivity*, Critical Reviews in Solid State and Materials Sciences **22**, 1 (1997).
- [4] D. Rugar and P. Hansma, *Atomic Force Microscopy*, Physics Today **43**, 23 (1990).
- [5] M. Imada, A. Fujimori, and Y. Tokura, *Metal-Insulator Transitions*, Reviews of Modern Physics **70**, 1039 (1998).
- [6] J. B. Theeten and D. E. Aspnes, *Ellipsometry in Thin Film Analysis*, Annual Review of Material Science **11**, 97 (1981).
- [7] S. P. Mulvaney and C. D. Keating, *Raman Spectroscopy*, Analytical Chemistry **72**, 145 (2000).

## References for Chapter 3

- [1] A. W. Sleight, *Bismuthates:  $BaBiO_3$  and Related Superconducting Phases*, Physica C **514**, 152 (2015).
- [2] K. Foyevtsova, A. Khazraie, I. Elfimov, and G. A. Sawatzky, *Hybridization Effects and Bond Disproportionation in the Bismuth Perovskites*, Physical Review B **91**, 121114 (2015).
- [3] P. V. Balachandran and J. M. Rondinelli, *Interplay of Octahedral Rotations and Breathing Distortions in Charge-Ordering Perovskite Oxides*, Physical Review B **88**, 054101 (2013).

- [4] H. Sato, S. Tajima, H. Takagi, and S. Uchida, *Optical Study of the Metal-Insulator Transition on  $Ba_{1-x}K_xBiO_3$  Thin Films*, Nature **338**, 241 (1989).
- [5] T. Nishio, J. Ahmad, and H. Uwe, *Spectroscopic Observation of Bipolaronic Point Defects in  $Ba_{1-x}K_xBiO_3$* , Physical Review Letters **95**, 176403 (2005).
- [6] S. Tajima, M. Yoshida, N. Koshizuka, H. Sato, and S. Uchida, *Raman-Scattering Study of the Metal-Insulator Transition in  $Ba_{1-x}K_xBiO_3$* , Physical Review B **46**, 1232 (1992).
- [7] A. W. Sleight, J. L. Gillson, and P. E. Bierstedt, *High-Temperature Superconductivity in the  $BaPb_{1-x}Bi_xO_3$  Systems*, Solid State Communications **17**, 27 (1975).
- [8] G. Kim, M. Neumann, M. Kim, M. D. Le, T. D. Kang, and T. W. Noh, *Suppression of Three-Dimensional Charge Density Wave Ordering via Thickness Control*, Physical Review Letters **115**, 226402 (2015).
- [9] H. Amano, N. Sawaki, I. Akasaki, and Y. Toyoda, *Metalorganic Vapor Phase Epitaxial Growth of a High Quality GaN Film Using an AlN Buffer Layer*, Applied Physics Letters **48**, 353 (1986).
- [10] Y. Chen, S. K. Hong, H. J. Ko, V. Kirshner, H. Wenisch, T. Yao, K. Inaba, and Y. Segawa, *Effects of an Extremely Thin Buffer on Heteroepitaxy with Large Lattice Mismatch*, Applied Physics Letters **78**, 3352 (2001).
- [11] K. Terai, M. Lippmaa, P. Ahmet, T. Chikyow, T. Fujii, H. Koinuma, and M. Kawasaki, *In-Plane Lattice Constant Tuning of an Oxide Substrate with  $Ba_{1-x}Sr_xTiO_3$  and  $BaTiO_3$  Buffer Layers*, Applied Physics Letters **80**, 4437 (2002).
- [12] H. G. Lee, Y. Kim, S. Hwang, G. Kim, T. D. Kang, M. Kim, M. Kim, and T. W. Noh, *Double-Layer Buffer Template to Grow Commensurate Epitaxial  $BaBiO_3$  Thin Films*, APL Materials **4**, 126106 (2016).
- [13] K. S. Knight, *Structural Phase Transitions in  $BaCeO_3$* , Solid State Ionics **74**, 109 (1994).



- [14] A. R. Akbarzadeh, I. Kornev, C. Malibert, L. Bellaiche, and J. M. Kiat, *Combined Theoretical and Experimental Study of the Low-Temperature Properties of BaZrO<sub>3</sub>*, Physical Review B **72**, 205104 (2005).
- [15] R. Chierchia, T. Böttcher, H. Heinke, S. Einfeldt, S. Figge, and D. Hommel, *Microstructure of Heteroepitaxial GaN Revealed by X-Ray Diffraction*, Journal of Applied Physics **93**, 8918 (2003).
- [16] P. E. Janolin, A. S. Anokhin, Z. Gui, V. M. Mukhortov, Y. I. Golovko, N. Guiblin, S. Ravy, M. el Marssi, Y. I. Yuzyuk, L. Bellaiche, and B. Dkhil, *Strain Engineering of Perovskite Thin Films Using a Single Substrate*, Journal of Physics: Condensed Matter **26**, 292201 (2014).
- [17] H. G. Lee, R. Kim, J. Kim, M. Kim, T. H. Kim, S. Lee, and T. W. Noh, *Anisotropic Suppression of Octahedral Breathing Distortion with the Fully Strained BaBiO<sub>3</sub>/BaCeO<sub>3</sub> Heterointerface*, APL Materials **6**, 016107 (2018).
- [18] G. Kresse and J. Furthmüller, *Efficiency of Ab-Initio Total Energy Calculations for Metals and Semiconductors Using a Plane-Wave Basis Set*, Computational Materials Science **6**, 15 (1996).
- [19] G. Kresse and J. Furthmüller, *Efficient Iterative Schemes for Ab Initio Total-Energy Calculations Using a Plane-Wave Basis Set*, Physical Review B **54**, 11169 (1996).
- [20] M. Zapf, M. Stübinger, L. Jin, M. Kamp, F. Pfaff, A. Lubk, B. Büchner, M. Sing, and R. Claessen, *Domain Matching Epitaxy of BaBiO<sub>3</sub> on SrTiO<sub>3</sub> with Structurally Modified Interface*, Applied Physics Letters **112**, 141601 (2018).
- [21] J. Kim, J. Mun, B. Kim, H. G. Lee, D. Lee, T. H. Kim, S. Lee, M. Kim, S. H. Chang, and T. W. Noh, *Coherent-Strained Superconducting BaPb<sub>1-x</sub>Bi<sub>x</sub>O<sub>3</sub> Thin Films by Interface Engineering*, Physical Review Materials **3**, 113606 (2019).
- [22] L. Jin, M. Zapf, M. Stübinger, M. Kamp, M. Sing, R. Claessen, and C. L. Jia, *Atomic-Scale Interface Structure in Domain Matching Epitaxial BaBiO<sub>3</sub> Thin Films Grown on SrTiO<sub>3</sub> Substrates*, Physica Status Solidi Letters **14**, 2000054 (2020).

## References for Chapter 4

- [1] G. Koster, L. Klein, W. Siemons, G. Rijnders, J. S. Dodge, C. B. Eom, D. H. A. Blank, and M. R. Beasley, *Structure, Physical Properties, and Applications of SrRuO<sub>3</sub> Thin Films*, *Reviews of Modern Physics* **84**, 253 (2012).
- [2] C. B. Eom, R. J. Cava, R. M. Fleming, J. M. Phillips, R. B. Vandover, J. H. Marshall, J. W. Hsu, J. J. Krajewski, and W. F. Peck, *Single-Crystal Epitaxial Thin Films of the Isotropic Metallic Oxides Sr<sub>1-x</sub>Ca<sub>x</sub>RuO<sub>3</sub>*, *Science* **258**, 1766 (1992).
- [3] L. Wang, R. Kim, Y. Kim, C. H. Kim, S. Hwang, M. R. Cho, Y. J. Shin, S. Das, J. R. Kim, S. v. Kalinin, M. Kim, S. M. Yang, and T. W. Noh, *Electronic-Reconstruction-Enhanced Tunneling Conductance at Terrace Edges of Ultrathin Oxide Films*, *Advanced Materials* **29**, 1702001 (2017).
- [4] Y. J. Shin, Y. Kim, S.-J. Kang, H.-H. Nahm, P. Murugavel, J. R. Kim, M. R. Cho, L. Wang, S. M. Yang, J.-G. Yoon, J.-S. Chung, M. Kim, H. Zhou, S. H. Chang, and T. W. Noh, *Interface Control of Ferroelectricity in an SrRuO<sub>3</sub>/BaTiO<sub>3</sub>/SrRuO<sub>3</sub> Capacitor and Its Critical Thickness*, *Advanced Materials* **29**, 1602795 (2017).
- [5] L. Klein, J. S. Dodge, C. H. Ahn, G. J. Snyder, T. H. Geballe, M. R. Beasley, and A. Kapitulnik, *Anomalous Spin Scattering Effects in the Badly Metallic Itinerant Ferromagnet SrRuO<sub>3</sub>*, *Physical Review Letters* **77**, 2774 (1996).
- [6] Z. Fang, N. Nagaosa, K. S. Takahashi, H. Yamada, M. Kawasaki, and Y. Tokura, *The Anomalous Hall Effect and Magnetic Monopoles in SrRuO<sub>3</sub>*, *Science* **302**, 92 (2003).
- [7] Y. Ohuchi, J. Matsuno, N. Ogawa, Y. Kozuka, M. Uchida, Y. Tokura, and M. Kawasaki, *Electric-Field Control of Anomalous and Topological Hall Effects in Oxide Bilayer Thin Films*, *Nature Communications* **9**, 213 (2018).
- [8] J. Matsuno, N. Ogawa, K. Yasuda, F. Kagawa, W. Koshihara, N. Nagaosa, Y. Tokura, and M. Kawasaki, *Interface-Driven Topological Hall Effect in SrRuO<sub>3</sub>-SrIrO<sub>3</sub> bilayer*, *Science Advances* **2**, 1600304 (2016).

- 
- [9] L. Wang, Q. Feng, Y. Kim, R. Kim, K. H. Lee, S. D. Pollard, Y. J. Shin, H. Zhou, W. Peng, D. Lee, W. Meng, H. Yang, J. H. Han, M. Kim, Q. Lu, and T. W. Noh, *Ferroelectrically Tunable Magnetic Skyrmions in Ultrathin Oxide Heterostructures*, *Nature Materials* **17**, 1087 (2018).
  - [10] J. Xia, W. Siemons, G. Koster, M. R. Beasley, and A. Kapitulnik, *Critical Thickness for Itinerant Ferromagnetism in Ultrathin Films of SrRuO<sub>3</sub>*, *Physical Review B* **79**, 140407 (2009).
  - [11] Y. J. Chang, C. H. Kim, S. H. Phark, Y. S. Kim, J. Yu, and T. W. Noh, *Fundamental Thickness Limit of Itinerant Ferromagnetic SrRuO<sub>3</sub> Thin Films*, *Physical Review Letters* **103**, 057201 (2009).
  - [12] K. Ishigami, K. Yoshimatsu, D. Toyota, M. Takizawa, T. Yoshida, G. Shibata, T. Harano, Y. Takahashi, T. Kadono, V. K. Verma, V. R. Singh, Y. Takeda, T. Okane, Y. Saitoh, H. Yamagami, T. Koide, M. Oshima, H. Kumigashira, and A. Fujimori, *Thickness-Dependent Magnetic Properties and Strain-Induced Orbital Magnetic Moment in SrRuO<sub>3</sub> Thin Films*, *Physical Review B* **92**, 064402 (2015).
  - [13] D. Toyota, I. Ohkubo, H. Kumigashira, M. Oshima, T. Ohnishi, M. Lippmaa, M. Takizawa, A. Fujimori, K. Ono, M. Kawasaki, and H. Koinuma, *Thickness-Dependent Electronic Structure of Ultrathin SrRuO<sub>3</sub> Films Studied by in Situ Photoemission Spectroscopy*, *Applied Physics Letters* **87**, 162508 (2005).
  - [14] Y. Kats, I. Genish, L. Klein, J. W. Reiner, and M. R. Beasley, *Testing the Berry Phase Model for Extraordinary Hall Effect in SrRuO<sub>3</sub>*, *Physical Review B* **70**, 180407 (2004).
  - [15] B. Sohn, E. Lee, W. Kyung, M. Kim, H. Ryu, J. S. Oh, D. Kim, J. K. Jung, B. Kim, M. Han, T. W. Noh, B. Yang, and C. Kim, *Sign-Tunable Anomalous Hall Effect Induced by Symmetry-Protected Nodal Structures in Ferromagnetic Perovskite Oxide Thin Films*, arXiv:1912.04757 (2019).
  - [16] J. Shin, A. Y. Borisevich, V. Meunier, J. Zhou, E. W. Plummer, S. v. Kalinin, and A. P. Baddorf, *Oxygen-Induced Surface Reconstruction of SrRuO<sub>3</sub> and Its Effect on the BaTiO<sub>3</sub> Interface*, *ACS Nano* **4**, 4190 (2010).

- 
- [17] N. B. Aetukuri, M. Drouard, K. P. Roche, A. X. Gray, C. A. Jenkins, H. A. Dürr, M. Cossale, E. Arenholz, A. H. Reid, M. G. Samant, S. S. P. Parkin, L. Gao, R. Kukreja, and H. Ohldag, *Control of the Metal–Insulator Transition in Vanadium Dioxide by Modifying Orbital Occupancy*, *Nature Physics* **9**, 661 (2013).
  - [18] R. G. Moore, J. Zhang, V. B. Nascimento, R. Jin, J. Guo, G. T. Wang, Z. Fang, D. Mandrus, and E. W. Plummer, *A Surface-Tailored, Purely Electronic, Mott Metal-to-Insulator Transition*, *Science* **318**, 615 (2007).
  - [19] D. P. Kumah, A. Malashevich, A. S. Disa, D. A. Arena, F. J. Walker, S. Ismail-Beigi, and C. H. Ahn, *Effect of Surface Termination on the Electronic Properties of  $\text{LaNiO}_3$  Films*, *Physical Review Applied* **2**, 054004 (2014).
  - [20] D. Lee, A. Yoon, S. Y. Jang, J. G. Yoon, J. S. Chung, M. Kim, J. F. Scott, and T. W. Noh, *Giant Flexoelectric Effect in Ferroelectric Epitaxial Thin Films*, *Physical Review Letters* **107**, 057602 (2011).
  - [21] W. S. Choi, C. M. Rouleau, S. S. A. Seo, Z. Luo, H. Zhou, T. T. Fister, J. A. Eastman, P. H. Fuoss, D. D. Fong, J. Z. Tischler, G. Eres, M. F. Chisholm, and H. N. Lee, *Atomic Layer Engineering of Perovskite Oxides for Chemically Sharp Heterointerfaces*, *Advanced Materials* **24**, 6423 (2012).
  - [22] A. Ohtomo and H. Y. Hwang, *A High-Mobility Electron Gas at the  $\text{LaAlO}_3/\text{SrTiO}_3$  Heterointerface*, *Nature* **427**, 423 (2004).
  - [23] T. Kimura and Y. Tokura, *Layered Magnetic Manganites*, *Most* **30**, 451 (n.d.).
  - [24] J. Choi, C. B. Eom, G. Rijnders, H. Rogalla, and D. H. A. Blank, *Growth Mode Transition from Layer by Layer to Step Flow during the Growth of Heteroepitaxial  $\text{SrRuO}_3$  on (001)  $\text{SrTiO}_3$* , *Applied Physics Letters* **79**, 1447 (2001).
  - [25] G. Rijnders, D. H. A. Blank, J. Choi, and C. B. Eom, *Enhanced Surface Diffusion through Termination Conversion during Epitaxial  $\text{SrRuO}_3$  Growth*, *Applied Physics Letters* **84**, 505 (2004).
  - [26] D. R. Lide, *CRC Handbook of Chemistry and Physics* (CRC press, Boca Raton, FL, 2005).

- 
- [27] H. G. Lee, L. Wang, L. Si, X. He, D. G. Porter, J. R. Kim, E. K. Ko, J. Kim, S. M. Park, B. Kim, A. T. S. Wee, A. Bombardi, Z. Zhong, and T. W. Noh, *Atomic-Scale Metal–Insulator Transition in SrRuO<sub>3</sub> Ultrathin Films Triggered by Surface Termination Conversion*, *Advanced Materials* **32**, 1905815 (2020).
  - [28] R. García, R. Magerle, and R. Perez, *Nanoscale Compositional Mapping with Gentle Forces*, *Nature Materials* **6**, 405 (2007).
  - [29] J. R. Kim, J. N. Lee, J. Mun, Y. Kim, Y. J. Shin, B. Kim, S. Das, L. Wang, M. Kim, M. Lippmaa, T. H. Kim, and T. W. Noh, *Experimental Realization of Atomically Flat and AlO<sub>2</sub>-Terminated LaAlO<sub>3</sub> (001) Substrate Surfaces*, *Physical Review Materials* **3**, 023801 (2019).
  - [30] M. Yoshimoto, T. Maeda, K. Shimozono, H. Koinuma, M. Shinohara, O. Ishiyama, and F. Ohtani, *Topmost Surface Analysis of SrTiO<sub>3</sub>(001) by Coaxial Impact-Collision Ion Scattering Spectroscopy*, *Applied Physics Letters* **65**, 3197 (1994).
  - [31] M. Katayama, E. Nomura, N. Kanekama, H. Soejima, and M. Aono, *Coaxial Impact-Collision Ion Scattering Spectroscopy (CAICISS): A Novel Method for Surface Structure Analysis*, *Nuclear Instruments and Methods in Physics Research B* **33**, 857 (1988).
  - [32] I. Asulin, O. Yuli, G. Koren, and O. Millo, *Evidence for Crossed Andreev Reflections in Bilayers of (100) YBa<sub>2</sub>Cu<sub>3</sub>O<sub>7-δ</sub> and the Itinerant Ferromagnet SrRuO<sub>3</sub>*, *Physical Review B* **74**, 009501 (2006).
  - [33] G. Kresse and J. Furthmüller, *Efficiency of Ab-Initio Total Energy Calculations for Metals and Semiconductors Using a Plane-Wave Basis Set*, *Computational Materials Science* **6**, 15 (1996).
  - [34] G. Kresse and J. Furthmüller, *Efficient Iterative Schemes for Ab Initio Total-Energy Calculations Using a Plane-Wave Basis Set*, *Physical Review B* **54**, 11169 (1996).
  - [35] J. P. Perdew, K. Burke, and M. Ernzerhof, *Generalized Gradient Approximation Made Simple*, *Physical Review Letters* **77**, 3865 (1996).

- [36] D. Pesquera, G. Herranz, A. Barla, E. Pellegrin, F. Bondino, E. Magnano, F. Sánchez, and J. Fontcuberta, *Surface Symmetry-Breaking and Strain Effects on Orbital Occupancy in Transition Metal Perovskite Epitaxial Films*, Nature Communications **3**, 1189 (2012).
- [37] S. Agrestini, Z. Hu, C. Y. Kuo, M. W. Haverkort, K. T. Ko, N. Hollmann, Q. Liu, E. Pellegrin, M. Valvidares, J. Herrero-Martin, P. Gargiani, P. Gegenwart, M. Schneider, S. Esser, A. Tanaka, A. C. Komarek, and L. H. Tjeng, *Electronic and Spin States of SrRuO<sub>3</sub> Thin Films: An x-Ray Magnetic Circular Dichroism Study*, Physical Review B **91**, 075127 (2015).
- [38] P. Mahadevan, F. Aryasetiawan, A. Janotti, and T. Sasaki, *Evolution of the Electronic Structure of a Ferromagnetic Metal: Case of SrRuO<sub>3</sub>*, Physical Review B **80**, 035106 (2009).
- [39] S. A. Lee, S. Oh, J. Y. Hwang, M. Choi, C. Youn, J. W. Kim, S. H. Chang, S. Woo, J. S. Bae, S. Park, Y. M. Kim, S. Lee, T. Choi, S. W. Kim, and W. S. Choi, *Enhanced Electrocatalytic Activity via Phase Transitions in Strongly Correlated SrRuO<sub>3</sub> Thin Films*, Energy and Environmental Science **10**, 924 (2017).

## References for Chapter 5

- [1] N. Nagaosa, J. Sinova, S. Onoda, A. H. MacDonald, and N. P. Ong, *Anomalous Hall Effect*, Reviews of Modern Physics **82**, 1539 (2010).
- [2] Z. Fang, N. Nagaosa, K. S. Takahashi, H. Yamada, M. Kawasaki, and Y. Tokura, *The Anomalous Hall Effect and Magnetic Monopoles in SrRuO<sub>3</sub>*, Science **302**, 92 (2003).
- [3] K. S. Takahashi, H. Ishizuka, T. Murata, Q. Y. Wang, Y. Tokura, N. Nagaosa, and M. Kawasaki, *Anomalous Hall Effect Derived from Multiple Weyl Nodes in High-Mobility EuTiO<sub>3</sub> films*, Science Advances **4**, 7880 (2018).
- [4] Y. Kats, I. Genish, L. Klein, J. W. Reiner, and M. R. Beasley, *Testing the Berry Phase Model for Extraordinary Hall Effect in SrRuO<sub>3</sub>*, Physical Review B **70**, 180407 (2004).

- 
- [5] R. Mathieu, A. Asamitsu, K. Takahashi, H. Yamada, M. Kawasaki, Z. Fang, N. Nagaosa, and Y. Tokura, *Anomalous Hall Effect in Ca-Doped SrRuO<sub>3</sub> Films*, Journal of Magnetism and Magnetic Materials **272**, 785 (2004).
  - [6] L. Klein, J. S. Dodge, C. H. Ahn, G. J. Snyder, T. H. Geballe, M. R. Beasley, and A. Kapitulnik, *Anomalous Spin Scattering Effects in the Badly Metallic Itinerant Ferromagnet SrRuO<sub>3</sub>*, Physical Review Letters **77**, 2774 (1996).
  - [7] B. Sohn, E. Lee, W. Kyung, M. Kim, H. Ryu, J. S. Oh, D. Kim, J. K. Jung, B. Kim, M. Han, T. W. Noh, B. Yang, and C. Kim, *Sign-Tunable Anomalous Hall Effect Induced by Symmetry-Protected Nodal Structures in Ferromagnetic Perovskite Oxide Thin Films*, arXiv:1912.04757 (2019).
  - [8] J. Matsuno, N. Ogawa, K. Yasuda, F. Kagawa, W. Koshibae, N. Nagaosa, Y. Tokura, and M. Kawasaki, *Interface-Driven Topological Hall Effect in SrRuO<sub>3</sub>-SrIrO<sub>3</sub> bilayer*, Science Advances **2**, 1600304 (2016).
  - [9] B. Sohn, B. Kim, S. Y. Park, H. Y. Choi, J. Y. Moon, T. Choi, Y. J. Choi, T. W. Noh, H. Zhou, S. H. Chang, J. H. Han, and C. Kim, *Emergence of Robust 2D Skyrmions in SrRuO<sub>3</sub> Ultrathin Film without the Capping Layer*, arXiv:1810.01615 (2018).
  - [10] L. Wang, Q. Feng, Y. Kim, R. Kim, K. H. Lee, S. D. Pollard, Y. J. Shin, H. Zhou, W. Peng, D. Lee, W. Meng, H. Yang, J. H. Han, M. Kim, Q. Lu, and T. W. Noh, *Ferroelectrically Tunable Magnetic Skyrmions in Ultrathin Oxide Heterostructures*, Nature Materials **17**, 1087 (2018).
  - [11] D. Kan, T. Moriyama, K. Kobayashi, and Y. Shimakawa, *Alternative to the Topological Interpretation of the Transverse Resistivity Anomalies in SrRuO<sub>3</sub>*, Physical Review B **98**, 180408 (2018).
  - [12] D. Kan, T. Moriyama, and Y. Shimakawa, *Field-Sweep-Rate and Time Dependence of Transverse Resistivity Anomalies in Ultrathin SrRuO<sub>3</sub> Films*, Physical Review B **101**, 014448 (2020).
  - [13] D. J. Groenendijk, C. Autieri, T. C. van Thiel, W. Brzezicki, N. Gauquelin, P. Barone, K. H. W. van den Bos, S. van Aert, J. Verbeeck, A. Filippetti, S. Picozzi, M. Cuoco, and A. D. Caviglia, *Berry Phase Engineering at Oxide Interfaces*, Physical Review Research **2**, 023404 (2020).

- 
- [14] G. Kimbell, P. M. Sass, B. Woltjes, E. K. Ko, T. W. Noh, W. Wu, and J. W. A. Robinson, *Two-Channel Anomalous Hall Effect in SrRuO<sub>3</sub>*, Physical Review Materials **4**, 54414 (2020).
  - [15] L. Wysocki, L. Yang, F. Gunkel, R. Dittmann, P. H. M. van Loosdrecht, and I. Lindfors-Vrejoiu, *Validity of Magnetotransport Detection of Skyrmions in Epitaxial SrRuO<sub>3</sub> Heterostructures*, Physical Review Materials **4**, 054402 (2020).
  - [16] L. Yang, L. Wysocki, J. Schöpf, L. Jin, A. Kovács, F. Gunkel, R. Dittmann, P. H. M. van Loosdrecht, and I. Lindfors-Vrejoiu, *Origin of the Hump Anomalies in the Hall Resistance Loops of Ultrathin SrRuO<sub>3</sub>/SrIrO<sub>3</sub> Multilayers*, Physical Review Materials **5**, 014403 (2021).
  - [17] L. Miao, N. J. Schreiber, H. P. Nair, B. H. Goodge, S. Jiang, J. P. Ruf, Y. Lee, M. Fu, B. Tsang, Y. Li, C. Zeledon, J. Shan, K. F. Mak, L. F. Kourkoutis, D. G. Schlom, and K. M. Shen, *Strain Relaxation Induced Transverse Resistivity Anomalies in SrRuO<sub>3</sub> Thin Films*, Physical Review B **102**, 64406 (2020).
  - [18] G. Kim, K. Son, Y. E. Suyolcu, L. Miao, N. J. Schreiber, H. P. Nair, D. Putzky, M. Minola, G. Christiani, P. A. van Aken, K. M. Shen, D. G. Schlom, G. Logvenov, and B. Keimer, *Inhomogeneous Ferromagnetism Mimics Signatures of the Topological Hall Effect in SrRuO<sub>3</sub> Films*, Physical Review Materials **4**, 104410 (2020).
  - [19] L. Wang, Q. Feng, H. G. Lee, E. K. Ko, Q. Lu, and T. W. Noh, *Controllable Thickness Inhomogeneity and Berry Curvature Engineering of Anomalous Hall Effect in SrRuO<sub>3</sub> Ultrathin Films*, Nano Letters **20**, 2468 (2020).
  - [20] J. Shin, A. Y. Borisevich, V. Meunier, J. Zhou, E. W. Plummer, S. v. Kalinin, and A. P. Baddorf, *Oxygen-Induced Surface Reconstruction of SrRuO<sub>3</sub> and Its Effect on the BaTiO<sub>3</sub> Interface*, ACS Nano **4**, 4190 (2010).
  - [21] S. H. Chang, Y. J. Chang, S. Y. Jang, D. W. Jeong, C. U. Jung, Y. J. Kim, J. S. Chung, and T. W. Noh, *Thickness-Dependent Structural Phase Transition of Strained SrRuO<sub>3</sub> Ultrathin Films: The Role of Octahedral Tilt*, Physical Review B **84**, 104101 (2011).



- [22] E. K. Ko, J. Mun, H. G. Lee, J. Kim, J. Song, S. H. Chang, T. H. Kim, S. B. Chung, M. Kim, L. Wang, and T. W. Noh, *Oxygen Vacancy Engineering for Highly Tunable Ferromagnetic Properties: A Case of SrRuO<sub>3</sub> Ultrathin Film with a SrTiO<sub>3</sub> Capping Layer*, *Advanced Functional Materials* **30**, 2001486 (2020).
- [23] A. Ohtomo and H. Y. Hwang, *A High-Mobility Electron Gas at the LaAlO<sub>3</sub>/SrTiO<sub>3</sub> Heterointerface*, *Nature* **427**, 423 (2004).
- [24] Y. Liang, Y. Wang, L. Liu, Q. Guo, W. Wang, H. Yang, and J. Guo, *Chemical Intermixing at Oxide Heterointerfaces with Polar Discontinuity*, *Applied Physics Letters* **112**, 231601 (2018).
- [25] H. B. Zhang, R. J. Qi, N. F. Ding, R. Huang, L. Sun, C. G. Duan, C. A. J. Fisher, J. H. Chu, and Y. Ikuhara, *Elemental Intermixing within an Ultrathin SrRuO<sub>3</sub> Electrode Layer in Epitaxial Heterostructure BaTiO<sub>3</sub>/SrRuO<sub>3</sub>/SrTiO<sub>3</sub>*, *AIP Advances* **6**, 015010 (2016).
- [26] P. S. Sankara Rama Krishnan, A. N. Morozovska, E. A. Eliseev, Q. M. Ramasse, D. Kepaptsoglou, W. I. Liang, Y. H. Chu, P. Munroe, and V. Nagarajan, *Misfit Strain Driven Cation Inter-Diffusion across an Epitaxial Multiferroic Thin Film Interface*, *Journal of Applied Physics* **115**, 054103 (2014).
- [27] J. N. Leboeuf, K. R. Chen, J. M. Donato, D. B. Geohegan, C. L. Liu, A. A. Puretzky, and R. F. Wood, *Modeling of Plume Dynamics in Laser Ablation Processes for Thin Film Deposition of Materials*, *Physics of Plasmas* **3**, 2203 (1996).
- [28] S. Lafane, T. Kerdja, S. Abdelli-Messaci, Y. Khereddine, M. Kechouane, and O. Nemraoui, *Correlation of Plume Dynamics and Oxygen Pressure with VO<sub>2</sub> Stoichiometry during Pulsed Laser Deposition*, *Applied Physics A: Materials Science and Processing* **112**, 159 (2013).
- [29] A. Ojeda-G-P, C. W. Schneider, M. Döbeli, T. Lippert, and A. Wokaun, *Plasma Plume Dynamics, Rebound, and Recoating of the Ablation Target in Pulsed Laser Deposition*, *Journal of Applied Physics* **121**, 135306 (2017).

---

# Appendix

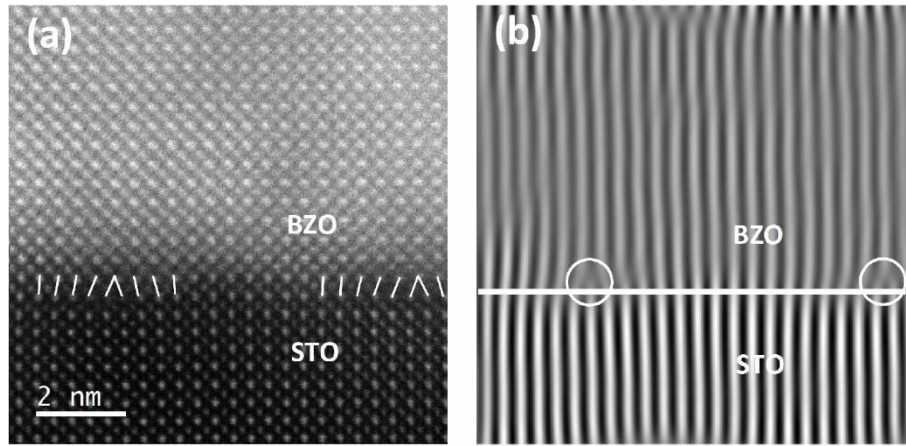
*Scientific progress is measured in units of courage, not intelligence.*

- Paul Dirac -

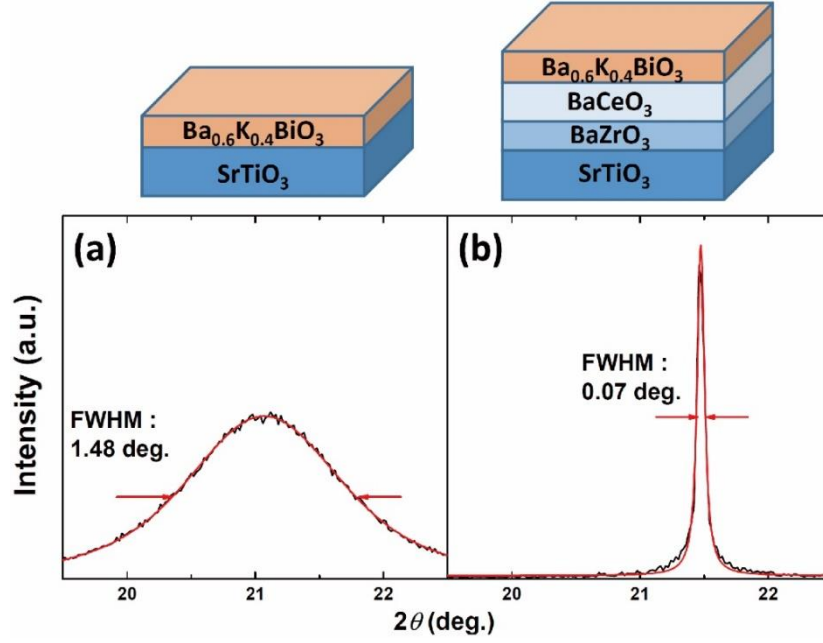
## Appendix A:

### Supplementary information for chapter 3

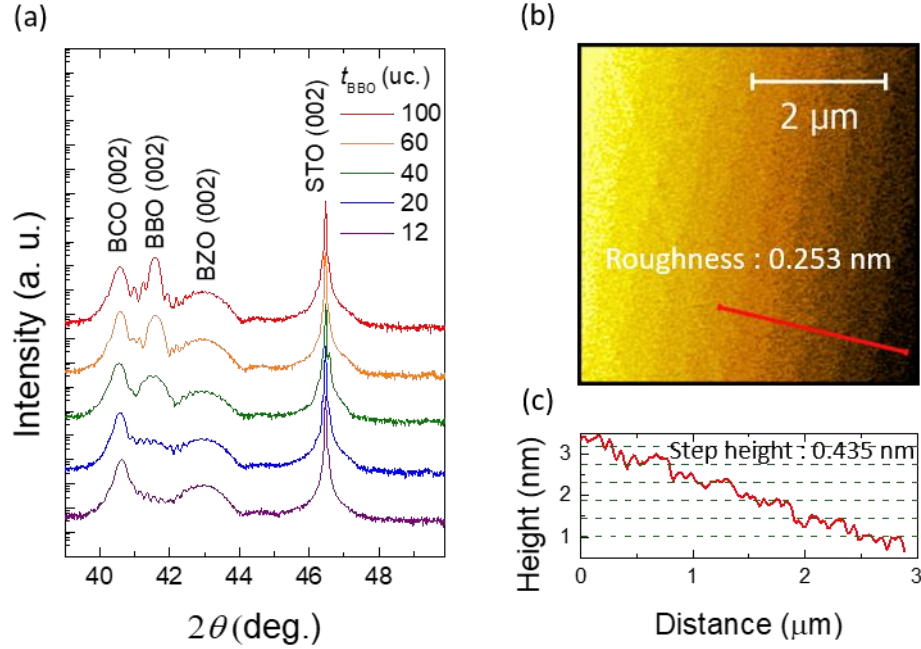
This part is mainly adapted from H. G. Lee *et al* (2016)., and H. G. Lee *et al* (2018).



**Appendix A-1. Microscopic analysis of misfit dislocations near the BaZrO<sub>3</sub>/SrTiO<sub>3</sub> interface.** **a)** Atomic-resolution transmission electron microscopy image of BaZrO<sub>3</sub> first-buffer layer on the SrTiO<sub>3</sub> substrate. **b)** Fourier-filtered images of the (a), using the (100) location. The white circles indicate the positions of misfit dislocations, and the white lines indicate the interfaces between layers. The distance between two dislocations (16 unit cell) is consistent with the lattice mismatch between BaZrO<sub>3</sub> and SrTiO<sub>3</sub> (7.38 %).

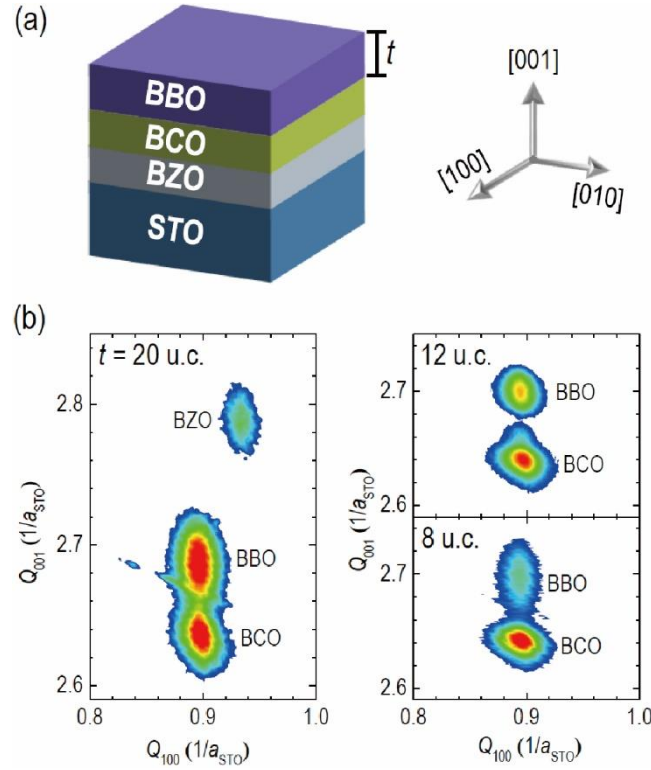


**Appendix A-2. Enhancement of crystallinity by using a bilayer buffer template.** X-ray diffraction rocking curve for (002) diffraction of superconducting  $\text{Ba}_{0.6}\text{K}_{0.4}\text{BiO}_3$  (BKBO) films on **a)** the  $\text{SrTiO}_3$  substrate and **b)** the double-buffer layer template. Red lines are Voight fitted plots of raw data. Arrows indicate full-width at half maximum values of rocking curves. The crystal quality of BKBO film was greatly enhanced by utilizing a double-layer buffer template.



### Appendix A-3. Characterization of the BaBiO<sub>3</sub> films and associated heterostructures.

**a)** X-ray diffraction  $\theta$ - $2\theta$  scans of BaBiO<sub>3</sub> (BBO) on BaCeO<sub>3</sub>/BaZrO<sub>3</sub>/SrTiO<sub>3</sub> (BCO/BZO/STO) (001) template with varying the thickness of BBO layer. The clear thickness fringes of BCO layers imply that BCO buffers have sharp and reliable interfaces with BBO layers. The thickness of the BBO layer is also controllable. **b)** Surface topographic image of BBO film measured by atomic force microscope. Step-and-terraced structure from the substrate exists. The surface roughness of each step is 0.253 nm whose value is smaller than 1 u.c. thickness of BBO which indicates high-quality heterostructure is synthesized. **c)** A line profile along the red line in (b). Averaged step height is consistent with 1 u.c. thickness of BBO.



**Appendix A-4. Fully strained BBO films on the bilayer buffer template.** **a)** Schematic diagram of BBO/BCO heterostructures on a (001)-oriented  $\text{SrTiO}_3$  (STO) substrate. A  $\text{BaZrO}_3$  (BZO) layer is inserted between BCO and STO to compensate for their large lattice mismatch. In this simple structure, we change the thickness  $t$  of BBO from 20 to 4 u.c. **b)** The in-plane strain state of BBO films with different thicknesses (20, 12, and 8 u.c.). Reciprocal space mappings are taken around (103) STO given that this peak is close to (103) BBO, (103) BCO, and (103) BZO. The same  $Q_{100}$  values indicate that all BBO films studied in this work are fully strained irrespective of thickness variation.

## Appendix B:

### Supplementary information for chapter 4

This part is mainly adapted from H. G. Lee *et al* (2020).

#### Nano-compositional imaging of perovskite oxide surface

Nano-compositional variation of the surface can be investigated by various real-space imaging techniques. The two of the well-established techniques are friction force microscopy (FFM) and atomically-resolved scanning tunneling microscopy (STM). In this work, we utilized another method: atomic force microscopy (AFM) phase measurement. Note that obtaining ex-situ atomically-resolved STM images for oxide films is extremely challenging. To verify the validity of the AFM phase image in identifying the surface termination of SrRuO<sub>3</sub>, we choose to compare the FFM and AFM phase images.

The surface of the STO(001) substrate is a proper platform to examine nano-compositional variation. The high-temperature annealing (at 1200 °C for 3 h in ambient) can cause significant segregation of SrO and TiO<sub>2</sub> terminations at the STO(001) surface. As shown in **Appendix B-1a-c**, the AFM height, AFM phase, and FFM images are captured in the same region of the STO surface. Both the AFM phase and FFM images show clear and similar contrasts from the mixed SrO and TiO<sub>2</sub> terminations. Moreover, according to the line profiles [**Appendix B-1d-f**], these contrasts show perfect one-to-one correspondence with those in height images. These results show that AFM phase and FFM images are, at least, equally suited to characterizing surface termination variation. Notably, as the AFM phase image is obtained using the tapping mode, it has a higher spatial

resolution than that of the FFM image (which was obtained using the contact mode). As indicated by the dotted circles in **Appendix B-1b,c**, the phase contrast from the tiny SrO-terminated area is much sharper than the FFM contrast. Therefore, the AFM phase image is better for imaging small features of surface termination variation.

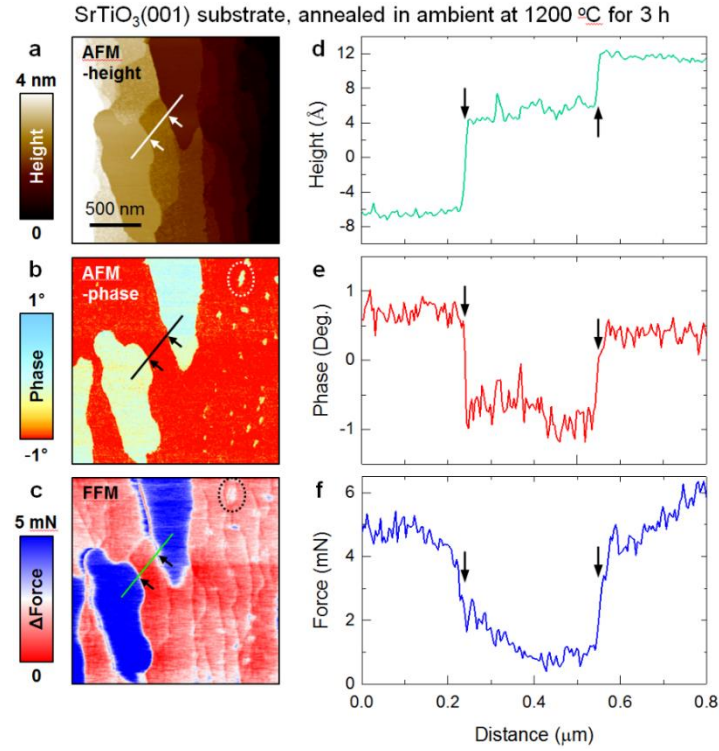
Finally, we explore the correlations between the AFM height and phase images of SRO films during water-leaching. The aforementioned STO substrate shows a good one-to-one correspondence between AFM height and phase images. By contrast, for the water-leached SRO thin films, the changes in AFM height images are much weaker than the AFM phase variations.

We suggest that the inhomogeneous SRO film surface after 10 or 20 s leaching is much more complicated than a simple mixture of SrO and RuO<sub>2</sub> terminations. Because of the highly reactive nature of SrO, the 10 or 20 s-leached surfaces should comprise not only a mixture of two terminations but also a variety of chemical residues [i.e. amorphous SrO<sub>x</sub> and Sr(OH)<sub>2</sub>]. These residues could form nanoscale clusters that can be smaller than the AFM tip radius (~20 nm). As schematically depicted in **Appendix B-2** (top panel), the topographic contribution from these nanoscale residues could be smeared by the AFM tip, resulting in a smaller AFM height signal than that produced by terrace-edges. On the contrary, surface chemical properties of the Sr-based residues and RuO<sub>2</sub>-terminated surface are distinct, which can produce a greater AFM phase signal than a terrace-edge [**Appendix B-2a** (bottom panel)]. Therefore, for the water-leached SRO case, the phase-contrast could be more sensitive to the mixed termination and chemical inhomogeneities.

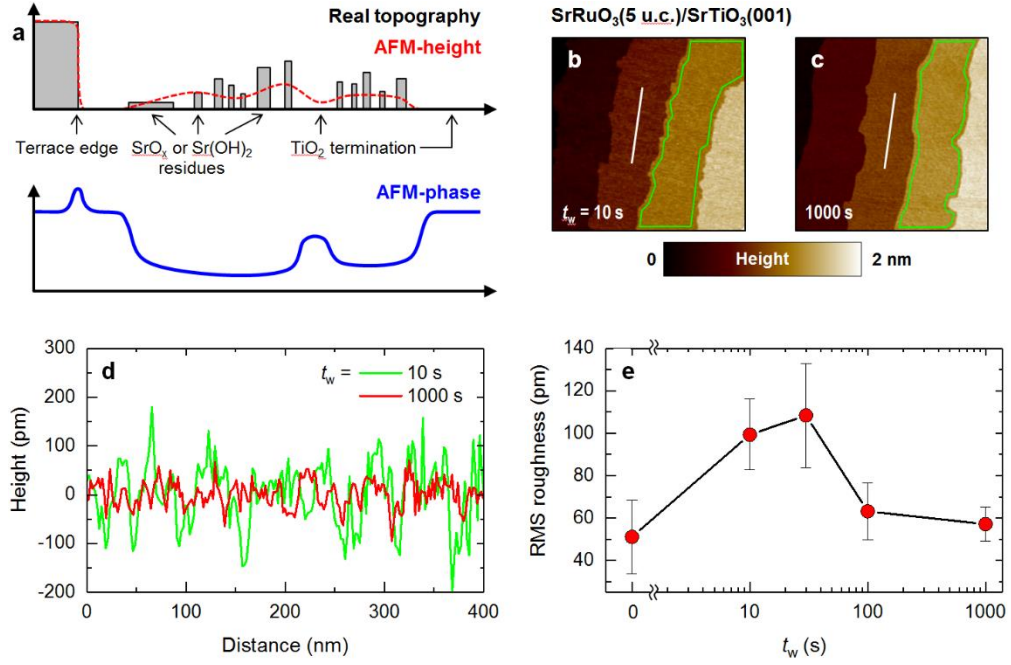
This theory was supported by further analyses of the AFM height images during water-leaching. Although all AFM height images for various  $t_w$  look similar [**Appendix B-2b,c**], the difference can be observed in the line profiles [**Appendix B-2d**]. The AFM height profile of the 10 s-leached sample shows nearly double fluctuations than that of the 1000 s-leached sample, which signifies the effect of the Sr-based residues on AFM height signals. Furthermore, we calculated the root-mean-square (RMS) roughness within each terrace (excluding the roughness contribution from terrace edges, marked by the open green loops in **Appendix B-2b,c**). As shown in **Appendix B-2e**, The surface roughnesses of the 10 and 20 s-leached samples were twice larger than that of the uniformly terminated samples (i.e., samples where  $t_w = 0, 100$ , and 1000 s). This result further confirms that the AFM height and phase images during water-leaching are consistent, while the phase-contrast is more sensitive to the termination conversion process, which can be more clearly identified.

Based on the above results and analyses, we suggest that the AFM phase images are a reliable technique to characterize the spatial variations of surface termination. Because of the higher spatial resolution, it is more suitable to characterize the SRO surface evolution compared to FFM. In the case of nano-scale compositional variation, a small compositional patch may not provide a large contribution to the AFM height image, while the contrast in the AFM phase is clear.





**Appendix B-1. Surface termination analyses on STO(001) substrates.** **a,b)** Atomic force microscopy (AFM, tapping mode) height (a) and phase (b) images (left panel) and line profiles (right panel) measured from the STO(001) substrate. **c)** Friction force microscopy (FFM, contact mode) images measured in the same region as that of the AFM images. The substrate was annealed at 1200 °C for 3 hours, which gives rise to severe step bunching and mixed-surface termination. Both the AFM phase and FFM images show a clear contrast between the SrO and TiO<sub>2</sub> terminated surface. The phase and friction force changes from the line profiles show a clear correlation with the topographic changes. Note that the spatial resolution of the tapping mode-AFM is better than that of contact mode-FFM. As marked by the dashed circles in (b) and (c), the AFM phase image is better for identifying the small features of nano-compositional variation.



### Appendix B-2. Detailed evolutions of AFM height images during water-leaching. a)

Schematic profiles of real topography, AFM height, and phase signal of a 10 s water-leached SRO surface. **b,c)** AFM height images of SRO(5.0 u.c.)/STO(001) film after water-leaching for 10 and 1000 s. **d)** Topographic height profiles derived along the lines marked in (a) and (b). **e)** Water-leaching time ( $t_w$ )-dependent root-mean-square (RMS) surface roughness measured from the AFM height images. The RMS roughness value was averaged over each flat terrace regions (as marked by the green loops) within every single terrace. The error bars represent the standard deviation from different terraces.

### Coaxial impact collision ion scattering spectroscopy

Coaxial impact collision ion scattering spectroscopy (CAICISS) is a low-energy ion scattering spectroscopy. This spectroscopy measures the time-of-flight (TOF) of injected ions backscattered by atoms at a surface along the specific crystallographic direction. Inert gas is typically used as the source of injected ions. The atomic masses of Sr (87.62u) and Ru (101.07u) are close to each other. In order to optimize the resolution of TOF spectroscopy, we choose  $\text{Ne}^+$  (20.18u) instead of the commonly used  $\text{He}^+$  (4.00u) as an injected ion. The change of velocity of Ne after scattering is larger than He due to the following equation.

$$v_s = \left( \frac{m - m_{\text{ion}}}{m + m_{\text{ion}}} \right) \cdot v_i$$

Where  $v_i$  is the initial velocity,  $v_s$  is the velocity of scattered ion,  $m$  ( $m_{\text{ion}}$ ) is the mass of the surface atom (injected ion). In our experimental set-up (**Appendix B-3**), the  $\text{Ne}^+$  ions are accelerated by pulse voltage. The  $\text{Ne}^+$  ions fly until they collide with the sample. Before the collision, they are neutralized to avoid charged scattering. After the collision, they are backscattered and fly back until they reach the detector.

The theoretical value of TOF can be estimated from the length between source and sample surface ( $L_1 = 836$  mm), sample surface and detector ( $L_2 = 395$  mm), initial velocity ( $v_i = 169373$  m/s), scattered velocity ( $v_s$ ), and pulsed delay time ( $\Delta = 100$  ns). The  $\Delta$  is the delay time between accelerating pulse voltage-time and actual  $\text{Ne}^+$  emission time, which is calibrated by using the Si reference sample. The  $v_i$  is determined as follows.

$$v_i = \left( \frac{2eV_{\text{acc}}}{m_{\text{Ne}}} \right)^{\frac{1}{2}}$$

Where  $V_{\text{acc}}$  is the accelerating pulse voltage and  $m_{\text{Ne}}$  is the mass of  $\text{Ne}^+$ . The calculated TOF values ( $t_{\text{total}} = L_1/v_i + L_2/v_s + \Delta$ ) scattered from Sr and Ru are determined as 8,755 and 8,532 ns, respectively. As shown in **Appendix B-4a,b**, the experimental TOF peak positions of the as-grown and water-leached samples are 8736 and 8554 ns, respectively. The experimental and theoretical values are very close to each other within the experimental error, implying both the as-grown and water-leached samples should be nearly singly-terminated.

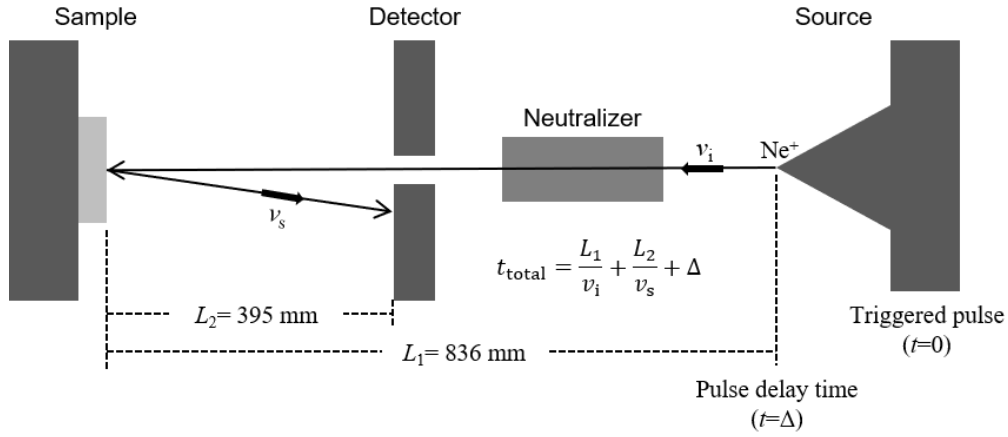
We subtract the background scattering by the polynomial fitting. However, the background intensities near the TOF peak are different in the pre-peak region and peak-tail region due to multiple scattering in the peak-tail region. To avoid artifact in analysis on peak position and shape due to the background subtraction, we patched the two background regions with arc-tangent function [**Appendix B-4a,b**].

After the background subtraction, we fit the peaks with Gaussian functions. The asymmetric peak feature can be fitted with two Gaussian peaks located at experimental TOF peak values [**Appendix B-4c,d**]. The coverage of SrO surface termination can be calculated using the following equation.

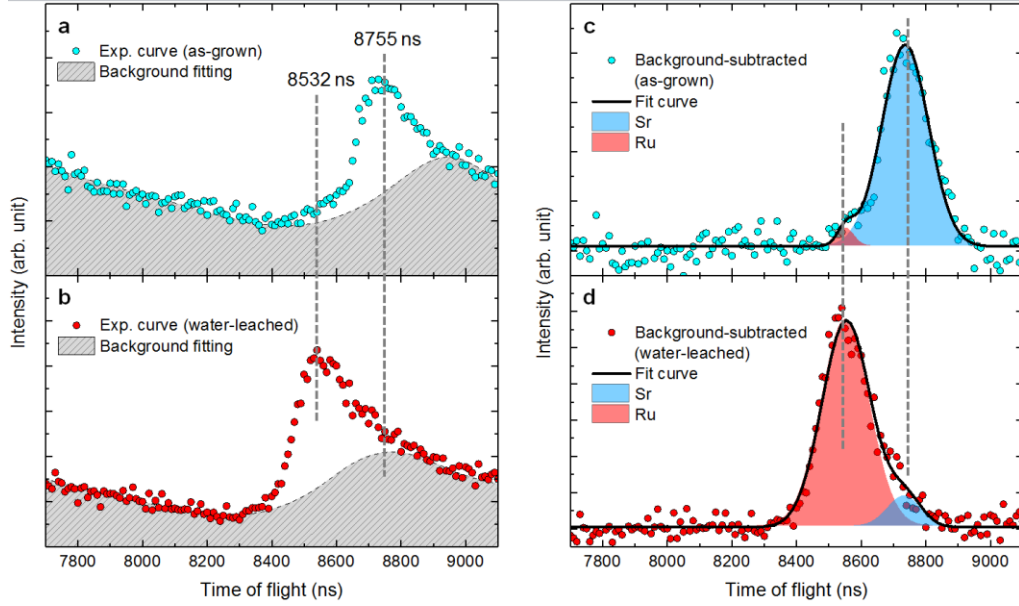
$$\frac{\sigma_{\text{Sr}}}{1 - \sigma_{\text{Sr}}} = \left( \frac{A_{\text{Sr}}/m_{\text{Sr}}}{A_{\text{Sr}}/m_{\text{Sr}} + A_{\text{Ru}}/m_{\text{Ru}}} \right)$$

Where  $A$  is the integrated peak area, and  $m_{\text{Sr}}$  ( $m_{\text{Ru}}$ ) is the mass of Sr (Ru). The error bars were derived from the standard error of Gaussian fitting. The coverage of SrO termination for the as-grown sample is  $96.9 \pm 3.1\%$  and the coverage of  $\text{RuO}_2$  termination for the water-

leached sample is  $89.7 \pm 3.0 \%$ . These results further confirmed that both the as-grown and water-leached SRO films have nearly uniform surface terminations as expected.

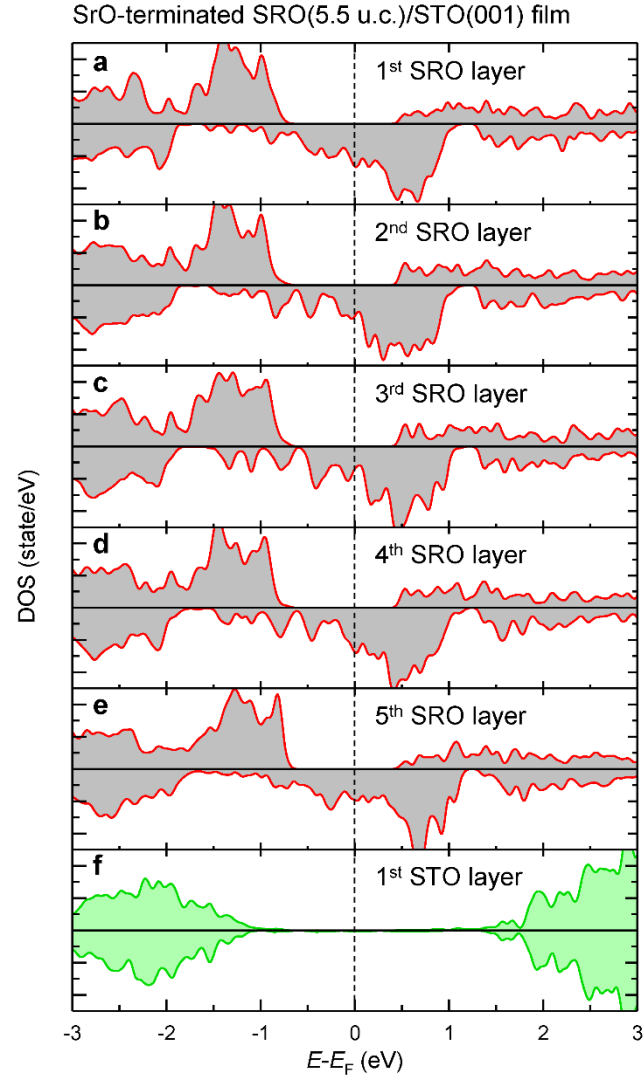


**Appendix B-3. Schematic diagram of the CAICISS experiment.** The  $\text{Ne}^+$  ions are accelerated by triggered pulse voltage at  $t = 0$ . The  $\text{Ne}^+$  ions fly with the initial velocity ( $v_i$ ) until they collide with the sample. Before the collision, they are neutralized to avoid charged scattering. After the collision, they are backscattered with the scattered velocity ( $v_s$ ) and fly back until they reach the detector. The time difference is measured using the triggered pulse time and detecting time. There is a delay time ( $\Delta$ ) of pulsed voltage and actual emission of  $\text{Ne}^+$  ion. The  $\Delta$  is calibrated by using the Si reference sample.

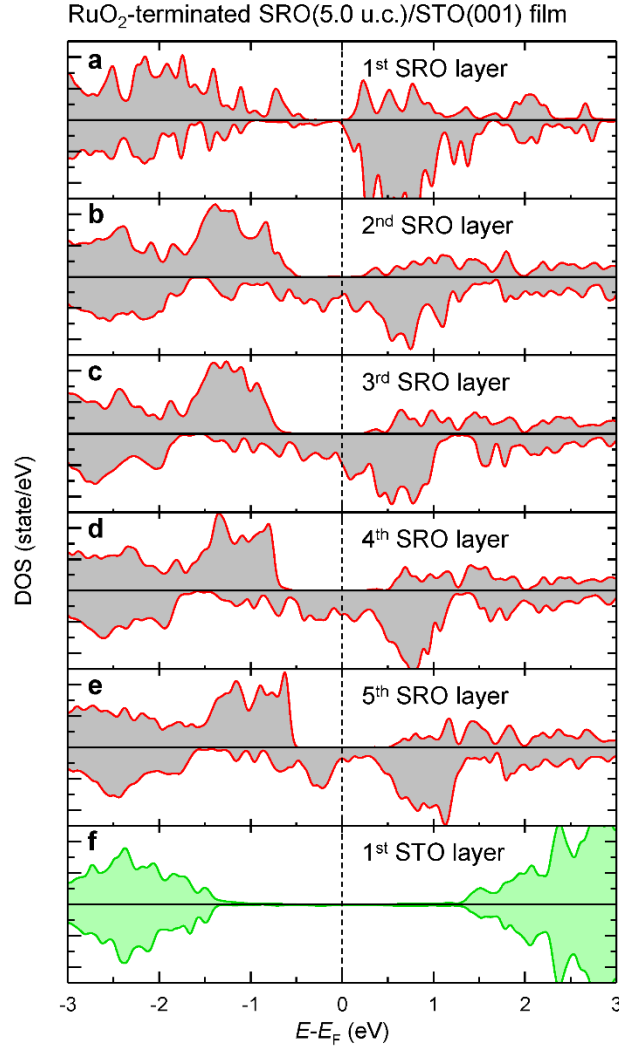


**Appendix B-4. Data processing and analyses of CAICISS-TOF spectra. a,b)** Measured TOF spectra on as-grown (a) and water-leached (b) samples. The background scattering is fitted with the polynomial function. We divide the background into two regions. The pre-peak region is defined at  $< 8300$  ns and the peak-tail region is defined at  $> 8800$  ns. The dashed lines denote the theoretically calculated TOF value for Sr (8,755 ns) and Ru (8,532 ns). **c,d)** Gaussian fits of background-subtracted experimental spectra. The blue (red) peak is the Gaussian fitting of the backscattering from Sr (Ru).

## Density functional theory calculation



**Appendix B-5. Layer-resolved density of states profiles of SrO-terminated SRO/STO(001) film.** a-e) Layer-resolved density of states (DOS) profiles projected along the five  $\text{RuO}_2$  planes in the SrO-terminated  $\text{SrRuO}_3(5.5 \text{ u.c.})/\text{SrTiO}_3(001)$  film. f) DOS profile projected along with the first STO layer in the SrO-terminated  $\text{SrRuO}_3(001)$  film.



**Appendix B-6. Layer-resolved density of states profiles of RuO<sub>2</sub>-terminated SRO/STO(001) film.** **a-e)** Layer-resolved density of states (DOS) profiles projected along each RuO<sub>2</sub> plane in the RuO<sub>2</sub>-terminated SrRuO<sub>3</sub>(5.0 u.c.)/SrTiO<sub>3</sub>(001) film. **f),** DOS profile projected along with the first STO layer in the SrO-terminated SrRuO<sub>3</sub>(001) film.



	FM-LS	FM-HS	FM-AF1	FM-AF2	G-AF	C-AF	A-AF
Energy/Ru	0	-4.8	-81.7	-11.6	-28.3	-79.7	-9.7
Total Moment	20	24	16	12	0	0	4
Surface state	Low-spin Conducting	High-spin Insulating	High-spin Insulating	Low-spin Conducting	High-spin Insulating	High-spin Insulating	Low-spin Conducting
	Surface	Surface	Surface	Surface	Surface	Surface	Surface
	2.0 2.0	4.0 4.0	4.0 -4.0	-2.0 -2.0	4.0 -4.0	4.0 -4.0	2.0 2.0
	2.0 2.0	2.0 2.0	2.0 2.0	2.0 2.0	-2.0 2.0	2.0 -2.0	-2.0 -2.0
	2.0 2.0	2.0 2.0	2.0 2.0	2.0 2.0	2.0 -2.0	2.0 -2.0	2.0 2.0
	2.0 2.0	2.0 2.0	2.0 2.0	2.0 2.0	-2.0 2.0	2.0 -2.0	-2.0 -2.0
	2.0 2.0	2.0 2.0	2.0 2.0	2.0 2.0	2.0 -2.0	2.0 -2.0	2.0 2.0
	STO(001)	STO(001)	STO(001)	STO(001)	STO(001)	STO(001)	STO(001)

**Appendix B-7. Density functional theory calculations of various magnetic configurations in RuO<sub>2</sub>-terminated SrRuO<sub>3</sub>/SrTiO<sub>3</sub>(001) film.** We tested a variety of ferromagnetic (FM) and antiferromagnetic (AF) orderings with high-spin (HS) or low-spin configurations. The bulk-like uniform FM ordering with LS configuration (FM-LS) is selected for the references. Here we only show the calculation results of six energetically lower solutions: uniform FM with HS surface (FM-HS), FM bulk with G-type HS AF surface (FM-AF1), FM bulk with A-type LS AF (FM-AF2), uniform G-type AF with HS surface (G-AF), uniform C-type AF with HS surface (C-AF), and uniform A-type AF with LS surface (A-AF). From this table, we found the FM-AF1 is the most energetically favorable spin configuration for the RuO<sub>2</sub>-terminated SRO/STO(001) films.

---

# Curriculum Vitae

*If a man never contradicts himself,  
the reason must be that he virtually never says anything at all.*

- Erwin Schrödinger -

## Han Gyeol Lee

### **B. S. degree**

Department of Physics Education, Seoul National University (3. 2011 ~ 2. 2015)

*Acquired Secondary School Regular Teacher (Grade II) of Physics from Ministry of  
Education, Republic of Korea*

### **Ph. D degree**

Department of Physics and Astronomy, Seoul National University (3. 2015 ~ 2. 2021)

*Supervised by Prof. Tae Won Noh*

### **Honors and Awards**

Brain Korea Outstanding Thesis Award (2021).

Brain Korea Doctoral Fellowship, (2020).

2019 Korean Physics Society Fall Meeting Oral Presentation Award, (2019).

2018 *APL Materials* Excellence in Research Award, (2018).

Brain Korea Doctoral Scholarship, (2017-2018).

Lecture & Research Scholarship, (2015-2016).

National Scholarship for Science and Engineering, (2013-2014).

### **Military Service**

Professional Research Personnel, Expiration Term of Service (3. 2021).

# List of Publication

- [1] *Double layer Buffer Template to Grow Commensurate Epitaxial BaBiO<sub>3</sub> Thin Films*  
**H. G. Lee**, Y. Kim, S. W. Hwang, G. Kim, T. D. Kang, M. Kim, M. Kim, and T. W. Noh  
APL Materials **4**, 126106 (2016).
- [2] *Anisotropic Suppression of Breathing Distortion with Fully-strained BaBiO<sub>3</sub> Heterointerface*  
**H. G. Lee**, R. Kim, J. Kim, M. Kim, T. H. Kim, S. Lee, and T. W. Noh  
APL Materials **6**, 016107 (2018).
- [3] *Evidence for Absence of Metallic Surface States in BiO<sub>2</sub>-terminated BaBiO<sub>3</sub> Thin Films*  
J. S. Oh, M. Kim, G. Kim, **H. G. Lee**, H. K. Yoo, S. Shin, Y. J. Chang, M. Han, C. Jozwiak, A. Bostwick, E. Rotenberg, H. -D. Kim, and T. W. Noh  
Current Applied Physics **18**, 658 (2018).
- [4] *Coherent-strained Superconducting BaPb<sub>1-x</sub>Bi<sub>x</sub>O<sub>3</sub> Thin Films by Interface Engineering*  
J. Kim, J. Mun, B. Kim, **H. G. Lee**, D. Lee, T. H. Kim, S. Lee, M. Kim, S. H. Chang, and T. W. Noh  
Physical Review Materials **3**, 113606 (2019).
- [5] *Atomic-scale Metal-Insulator Transition in SrRuO<sub>3</sub> Ultrathin Films Triggered by Surface Termination Conversion*  
**H. G. Lee**, L. Wang, L. Si, X. He, D. G. Porter, J. R. Kim, E. K. Ko, J. Kim, S. M. Park, B. Kim, A. T. S. Wee, A. Bombardi, Z. Zhong, and T. W. Noh  
Advanced Materials **32**, 195815 (2020).
- [6] *Controllable Thickness Inhomogeneity and Berry Curvature Engineering of Anomalous Hall Effect in SrRuO<sub>3</sub> Ultrathin Films*  
L. Wang, Q. Feng, **H. G. Lee**, E. K. Ko, Q.-Y. Lu, and T. W. Noh  
Nano Letters **20**, 2468 (2020).

- [7] *Pair Suppression Caused by Mosaic-twist Defects in Superconducting  $\text{Sr}_2\text{RuO}_4$  Thin-films Prepared Using Pulsed Laser Deposition*  
C. P. Garcia, A. D. Bernardo, G. Kimbell, M. Vickers, F. Massabuau, S. Komori, G. Divitini, Y. Yasui, **H. G. Lee**, J. Kim, B. Kim, M. Blamire, A. Vecchione, R. Fitipaldi, Y. Maeno, T. W. Noh, and J. Robinson  
*Communications Materials* **1**, 23 (2020).
- [8] *Colossal Flexoresistance in Dielectrics*  
S. M. Park, B. Wang, T. Paudel, S. Y. Park, S. Das, J. R. Kim, E. K. Ko, **H. G. Lee**, N. Park, L. Tao, D. Suh, E. Y. Tsymlal, L.-Q. Chen, T. W. Noh, and D. Lee  
*Nature Communications* **11**, 2586 (2020).
- [9] *Oxygen Vacancy Engineering for Highly Tunable Ferromagnetic Properties: A Case of  $\text{SrRuO}_3$  Ultrathin Film with a  $\text{SrTiO}_3$  Capping Layer*  
E. K. Ko, J. Mun, **H. G. Lee**, J. Kim, J. Song, S. H. Chang, T. H. Kim, S. B. Chung, M. Kim, L. Wang, and T. W. Noh  
*Advanced Functional Materials* **30**, 2001486 (2020).
- [10] *Stabilizing Hidden Room-Temperature Ferroelectricity via a Metastable Atomic Distortion Pattern*  
J. R. Kim, K.-J. Ko, J. Jang, S. Y. Park, C. J. Roh, J. Bonini, J. Kim, **H. G. Lee**, K. M. Rabe, J. S. Lee, S.-Y. Choi, T. W. Noh, and D. Lee  
*Nature Communications* **11**, 4944 (2020).

---

## 국문 초록 (Korean Abstract)

페로브스카이트 산화물은 강유전성, 자성, 금속-비금속 전이, 초전도와 같은 유용한 성질을 가진다. 이러한 성질은 해당 물질의 독특한 산소 팔면체 구조로부터 기인한다. 산소 팔면체의 크기, 모양, 회전은 중심부의 양이온과 산소간의 상호작용을 결정한다. 이를 조절하는 효과적인 방법 중 하나는 박막 제작을 통한 계면 제어이다. 본 학위 논문에서는 박막의 계면 제어에서 중요한 점이 무엇인지, 그리고 그들을 어떻게 다룰 수 있는지에 대해 논하고자 한다.

첫번째로, 해당 논문에서는  $\text{BaBiO}_3$ 와 같은 격자 상수가 큰 물질의 격자맞춤-에피성장(commensurate epitaxy)을 위한 완충층(buffer layer)에 대해 탐구하였다.  $\text{BaBiO}_3$ 는 breathing 변형이라는 독특한 산소 팔면체 구조로 인해 비금속성을 지니는 물질이다. 기판과 해당 물질 사이의 큰 격자상수 극복을 위해 본 연구에서는  $\text{BaZrO}_3/\text{BaCeO}_3$  로 이루어진 이중 완충층 기법을 사용하였다. 이를 통해 대부분의 격자 빗맞음(misfit dislocation)을  $\text{BaZrO}_3$  층에 상쇄시킬 수 있었고, 최초로  $\text{BaBiO}_3$ 의 격자맞춤-박막성장에 성공하였다. 이를 이용하여 대칭성 깨짐을 통한 breathing 변형의 한계 두께를 명확하게 구할 수 있게 되었다.

두번째로, 해당 논문에서는 박막의 표면층(surface layer)이 물성에 미치는

영향에 대해 탐구하였다. 초박막의 표면층이 표면의 분극에 영향을 미친다는 점은 잘 알려져 있다. 본 연구에서는, 더 나아가 표면의 분극이 크지 않은 경우에도 팔면체 대칭성 깨짐을 통해 표면층이 물성에 큰 영향을 미칠 수 있다는 점을 규명하였다. 이를 위해 본인은 새로운 물-식각 방식을 개발하여  $\text{SrRuO}_3$  물질의 표면층을  $\text{SrO}$ 로부터  $\text{RuO}_2$ 로 변환하는데 성공하였다. 이러한 표면층 변화는 금속-비금속 전이를 유발하였다. 이 점은 산소 팔면체의 표면층의 구조가 결정장(crystal field) 변형을 통한 오비탈 채움과 전자구조에 큰 영향을 미칠 수 있다는 점을 시사한다.

마지막으로, 해당 논문에서는  $\text{LaAlO}_3$  덮음층(capping layer)이  $\text{SrRuO}_3$  박막에 미치는 영향에 대해 연구하였다.  $\text{SrRuO}_3$ 에서 나타나는 비정상 홀 효과는 다양한 물리적 변화에 민감하다는 점이 잘 알려져 있다. 최근에는 해당 물질의 비정상 홀 효과 섞임과 관련해 많은 논의가 진행되어 왔다. 본 연구에서는 이러한 비정상 홀 효과 섞임을 체계적으로 제어하기 위해 덮음층을 이용하였다. 이를 통해 덮음층 형성 과정에서의 큰 운동에너지가  $\text{SrRuO}_3$  박막의 비균질성에 영향을 미치고 비정상 홀 효과 섞임에 기여할 수 있음을 규명하였다.

**주요어:** 페로브스카이트 산화물, 박막, 계면 제어, 완충층, 표면층, 덮음층,  $\text{BaBiO}_3$ ,  $\text{SrRuO}_3$ , 산소 팔면체 변형, 금속-비금속 전이, 비정상 홀 효과

**학번:** 2015-20349

---

## 감사의 글 (Acknowledgements)

*If I have seen further than others,  
it is by standing upon the shoulders of giants.*

- Isaac Newton -

학위 최종 심사를 마치던 날, 건물을 나와 한참 동안을 서성였던 까닭은 지금까지의 수많은 기억이 머릿속을 맴돌았기 때문일 것입니다. 스무 살 무렵만 해도 새로웠던 캠퍼스가 너무나도 익숙해지고, 관악의 열 번째 겨울 공기가 얼굴을 스칠 때, 많은 분과 함께했던 일들이, 그리고 그 속에 있던 어리고 부족한 제가 떠올라 발걸음을 옮기기 어려웠습니다. 돌이켜보면 저는 살가운 아들, 착실한 제자, 씩씩한 후배, 든직한 선배와는 거리가 먼 사람이었던 것 같습니다. 그럼에도 불구하고 학위과정을 무사히 마칠 수 있었던 것은 제가 운이 좋은 사람인 덕분입니다. 그리고 그 운은 부족한 저를 이끌어준 주변의 많은 도움이 모여 이루어진 것이라 생각합니다. 짧은 글로 모든 감사를 대신할 순 없겠지만, 제가 차곡차곡 쌓아온 기억 속의 많은 얼굴들에게 그 마음이 닿기를 바라며 감사의 글을 적어봅니다.

노태원 교수님, 학부생 티를 벗지 못했던 시절부터 저는 연구자의 태도, 학자의 인간관계를 맺어가는 방법, 연구 결과를 남들에게 발표하고 글로 표현하는 방법들을 교수님께 하나하나 배워왔습니다. 당시에는 이해가 되지 않는 가르침도 많았고, 잘 따르지 못했던 것도 있지만, 시간이 지나면서 하나하나 교수님의 가르침이 큰 도움이 되었습니다. 제가 부족해 아직 이해를 못 한 가르침들 역시 조금 더 시간이 흐르고 많은 경험이 쌓이다 보면 언젠가 깨닫게 되는 순간이 올 것이라 믿고 있습니다. 그렇기에 교수님께서 주신 수많은 말씀을 가슴에 품고 살아가겠습니다.

바쁘신 와중 학위심사를 해주시고 많은 조언을 해주신 차국런 교수님, 김창영 교수님, 양범정 교수님께도 감사의 말을 드리고 싶습니다. 또한, 학위심사를 도와주시고 선배 연구자로서 모범적인 태도를 보여주신 장서형

교수님, 때때로 교수님의 가르침이 무섭기도 했지만, 후배를 아끼고 걱정하는 마음에 주신 많은 조언이 있었기에 학문에 대한 초심을 잃지 않을 수 있었습니다. 논문 작업을 도와주신 이신범 교수님, 교수님과 글을 쓰면서 많은 것들을 즐겁게 배울 수 있었습니다. 그리고 주말에도 멀리까지 오셔서 연구를 도와주신 채승철 교수님, 김태현 교수님, 양상모 교수님, 이대수 교수님, 정진석 교수님에게도 많은 가르침을 받을 수 있어 감사했습니다. 또한, 든든하게 TEM 공동연구를 책임져 주신 김미영 교수님께도 감사드립니다.

연구단에서 함께한 많은 박사분에게도 감사를 전하고 싶습니다. 먼저 김민우 박사님, 연구에 대해 아무것도 몰랐던 학생이 박사님을 만난 것은 정말 큰 행운이었습니다. 저의 첫 연구 주제, 데이터 해석, 논문 찾기, 자료 준비, 글쓰기를 박사님과 함께했던 것은 6년간 대학원 생활의 튼튼한 기초가 되었습니다. 24살 무렵, 어렸던 제가 조금 더 성숙한 제자이지 못했던 점만이 아쉬울 뿐입니다. 김봉주 박사님, 여러 국제 학회와 해외 협업 등 저의 많은 경험은 박사님이 없었다면 가질 수 없었을 것입니다. 박사님과 함께였기에 연구 내외적으로 즐거웠던 기억들이 많습니다. Dear Dr. Lingfei, I learned how to survive in this cutthroat academia from you. It was great experience to me that I had a chance to work with you. Dear Dr. Olecksandr, and Dr. Saikat, I appreciate your help when I was 'a literally freshman'. 조명래 박사님, 박병철 박사님, Wei 박사님께도 깊은 감사의 말을 전합니다.

저는 연구실 선배분들에게도 많은 도움을 받았습니다. 벌써 늙은 교수님이 된 창희형, 아직 저의 연구실이 정해지지 않았던 시절, 다른 연구실을 방문해보면 항상 무거운 공기가 가득해 걱정을 많이 했었는데, 이곳을 오니 형 덕분에 다들 친근하고 따뜻한 분위기였던 기억이 납니다. 현주누나, 많이 얘기를 나누진 못했지만, 항상 제 기억 속 첫 방장님으로 감사한 마음 가지고 있습니다. 무서워 보이지만 사실 친근한 영재형, 형의 큰 존재감 덕분에 많은 추억이 생겼던 것 같습니다. 준비하시는 일이 잘 풀려



한국에서도 뵙고 싶습니다. 신입생 시절 옆자리 수빈형, 당시 너무나도 어려워 보이는 (사실 지금 봐도 잘 모르겠는) ARPES 연구를 묵묵하게 해내시는 모습이 대단했습니다. 그 누구보다 후배들을 아끼는 (하지만 티내면 부끄러워하시는) 척척박사 지섭형, 공부하다 모르는 게 있으면 항상 형에게 달려가 물어봤던 기억이 납니다. 혹여나 캘리포니아에서 만나게 된다면 함께 순댓국에 소주 한잔하면 좋을 것 같습니다. 다방면으로 멋진 민철형, 타지에서든 멋지게 연구 생활해나가실 거라 믿습니다. 형의 모범적인 태도를 볼 수 있었기에 저 역시 긴 방장 생활 무탈하게 할 수 있었습니다. 서버에 올려주신 박사졸업 공략집(?)도 정말 큰 도움이 되었습니다. 다정한 옆집 아저씨 같은 우진형, 어려운 연구 주제에도 따뜻한 가슴 잃지 않고 나아가는 모습에서 많은 힘을 얻었습니다. 저는 아재력으로는 동년배 누구에게도 지지 않을 거로 생각했는데 형에게 한 수 배울 수 있어 영광이었습니다. 차분하면서도 내공이 느껴지는 인호형, 많은 것들이 힘에 부치던 순간, 형의 진중한 모습이 큰 도움이 되었습니다. 함께 연구할 기회가 없어 아쉬웠습니다. 인간미와 똑부러짐을 동시에 갖춘 소연누나, 열심히 할 일을 하다가도 점심과 커피타임은 꼭 챙겨주신 덕분에 한숨 돌리며 뒤를 돌아볼 수 있게 되었습니다. 공동연구는 하지 못했지만, 공동장난(?)도 주고받으며 즐거운 연구실 생활 할 수 있었습니다. 연구단 최고의 승부사, 게임이라면 누구에게도 지지 않는 (하지만 스타는 나한테 진) 성민형, 형이 없었다면 (없을 때도 많았지만?) 연구 생활이 많이 심심했을 것 같습니다. 논문 검색하는 것부터 주차하는 법까지 형에게 다방면으로 많은 것들을 배웠습니다. 저의 첫 사수였던 듬직한 기덕형, 처음으로 형에게 PLD를 배우던 날부터 함께 첫 박막을 기르고 측정하던 순간의 기억이 아직도 생생합니다. 형의 매섭지만 디테일한 가르침은 실험하는 사람에게 하나하나 소중한 자산이 되었습니다. 감수성 풍부한 호동형, 같은 팀의 박사님과 선배분들이 연구실을 떠나고, 저년차 학생들만 남아 고생하던 시절이 떠오릅니다. 어디에서든 행복하시면 좋겠습니다. 인턴이자 선배 같았던 동갑내기 지현, 잠깐이었지만 같이 연구할 수 있어 즐거웠습니다.

긴 시간을 동고동락했던 동기들이 없었다면 학위과정을 끝까지 해나가지 못했을 것입니다. 함께한 추억들을 적자면 밤을 새워도 모자랄 정래, 하루가 멀다고 시답잖은 소리만 해대는 저를 그래도 동기라고 하나하나 가르쳐주느라고 생이 많았습니다. 실험실에서 박막을 기르고, 코르시카섬에서 텡스 점수를 확인하고, 교토 강변에서 맥주를 마시고 (온라인에서는 아제로스를 지키고), 모두가 퇴근한 밤 앞이 안 보이게 내리던 눈에 밤을 지새우며 연구실에 갇혀있던 모든 기억이 ‘그땐 그랬지’ 하며 함께 술 한잔 기울일 날이 오면 좋겠습니다. 서로 다른 연구실에 있었지만 언제 친해졌는지도 모르게 정말 친해져 버린 병민, 항상 즐겁게 담소를 나눌 수 있어 좋았습니다. 결혼 축하하고 미국에서도 건승하길 바랍니다. 한국에 있을 얼마 남지 않은 시간 동안 더 자주 상호작용합시다 (김정래 박사도 끼면 3-body problem). 대학원 입학 동기이자 학부 선배인 재석형, 형과 함께 대학원 양자역학 과제들을 끙끙대며 풀던 게 엊그제 같은데, 아니 학부 신입생 새터 버스 옆자리에 앉았던 게 벌써 10년이 흘렀습니다. 얼마 남지 않은 졸업 무탈히 잘 이루시길 바랍니다.

연구실의 후배들 역시 저에게 큰 힘이 되어줬고, 덕분에 많은 것들을 배우기도 했습니다. 열정과 흥이 넘치는 진권, 호동형 졸업 후 지도해줄 박사님도 없이 같은 팀의 선배라곤 1년 차이 밖에 안 나는 (똑같이 아무것도 모르는) 저밖에 없던 시절, 함께 고생하고 부딪혀 가며, 때로는 스스로 헤쳐나가는 모습에 감명받았습니다. 무엇을 하든 잘할 것이라 기대됩니다. 가장 많이 장난을 쳤지만 언제나 아껴 주고 싶은 범주, 기존에 하던 것이 아닌 새로운 분야에 도전하는 일은 어려울 수밖에 없습니다. 초조할 수도 있겠지만 지금처럼 꾸준히 노력하다 보면 곧 좋은 결과가 있을 것으로 생각합니다. 항상 연구실 막내일 것 같던 모습에서 어느새 믿음직스러운 연구자로 성장한 은교, 열심히 하다 보면 지칠 때도 있을 텐데, 티 없이 잘 견디고 있는 것 같습니다. 할 일도 꼼꼼하게 잘하면서 (그 와중에 철없는 선배도 챙기고) 밝은 태도를 잃지 않는 모습에 힘을 얻었습니다. 함께

연구하느라 수고가 많았고 좋은 논문으로 잘 마무리해봅시다. 물리 공부도, 실험도 (물리력도) 꾸준히 단련하는 정근, 어려운 주제를 맡은 와중 도와줄 만한 박사님과 선배도 떠난 상황에서 고생이 많습니다. 한 우물을 끝까지 파서 물을 얻어내는 모습도 멋지지만, 깊은 우물을 파다 지치면 때론 물을 사서 마셔야 다시 계속해서 일할 수 있습니다. 적당한 생수를 잘 찾아 품에 숨겨두면 좋을 것 같습니다. 마찬가지로 연구를 묵묵하게 잘 진행 중인 지환, 항상 늦게까지 실험에 몰두하는 모습이 대견합니다. 연구 생활과 여가 생활의 경계를 좀 더 확실하게 정해둔다면 고된 실험 후 자신을 추스를 여유를 가질 수 있을 것입니다. 자신 있는 모습이 보기 좋은 홍준, 열심히 잘하고 있습니다. 실험과 코스웍, 논문 공부와 작성을 병행하는 것은 힘든 일이겠지만 잘 해낼 수 있을 것입니다. 그리고 제 마지막 후배가 된 민수, 여러 핑계로 잘 챙겨주지 못해 미안합니다. 그럼에도 연구 주제에 대해 고민하고 실험들을 잘해나가고 있어 훌륭합니다. 앞으로 함께 남은 시간 동안 좋은 결과를 얻어 원하는 바를 이룰 수 있길 바랍니다.

연구단의 다른 식구들에게도 감사의 말을 드리고 싶습니다. 진공 장비에 문제가 생길 때마다 챙겨주신 박원구 박사님, 광학분석을 도와주신 강태동 박사님, 첫 독일 출장을 책임져 주신 이인호 선생님, 소모품과 수많은 장비를 관리해주신 김금채 선생님, 송인경 박사님, 장성진 박사님, 권오성 선생님, 이나현 선생님, 조수진 선생님, 신중열 박사님, 박태영 선생님, 클린룸 사용을 지도해주신 배현이 선생님 모두가 곁에서 도와주셨기에 항상 든든한 마음으로 연구에 몰두할 수 있었습니다. 또한, 복잡한 행정업무를 척척 해결해주시는 행정실의 전지현 실장님, 김정란 선생님, 주양희 선생님, 박주영 선생님, 지정은 선생님, 손주희 선생님, 엘리카 선생님, 김서경 선생님, 김민선 선생님, 한나 선생님, 이민희 선생님, 아직은 일하는 것이 어설피기만 한 학생을 도와주셔서 많이 배울 수 있었습니다. 항상 감사한 마음을 가지고 있습니다.

슬픈 일도 즐거운 일도 함께한 우리 자랑스러운 대동인들, 창우, 현석, 승언, 상영, 태욱, 경민, 세현, 형욱, 성현, 석오, 서로 살아가는 큰 힘이 돼주었고

앞으로도 계속 함께했으면 좋겠습니다. 과학교육계열 11 노답(no doubt) 태원, 상범, 창현, 희호, 의준, 현수, 정훈, 도연, 동영, 정안, 오랜 캠퍼스 생활을 버티게 해주는 활력소였고 함께여서 즐거웠습니다. 록 밴드 파문의 재훈형, 민환형, 경훈형, 나영 (철학자의 길 안 까먹음), 서진, 혜승, 민선, 덕분에 잠깐 숨돌리며 다채로운 경험을 가질 수 있었습니다. 화장품 걱정 없이 연구만 하게 도와준 성민, 차가운 동생을 따뜻하게 챙겨준 민준형도 고마웠습니다.

마지막으로 여기 그 누구보다 저를 걱정해주시고 아껴 주시는 부모님, 저는 부모님께 무심하면서도 까탈스러운, 어려운 아들이었던 것 같습니다. 물리 공부를 하겠다고 혼자 서울에 올라온 지 어느덧 10년이 지나고, 철부지 같던 아들은 지금도 여전히 철이 덜 들었고 갈 길이 멀어 보이지만, 그럼에도 사회로의 작은 발걸음을 내디뎌 보고자 합니다. 앞을 보며 걷고 있는 저 자신도 앞으로의 길이 복잡하고 어려운데, 멀리서 전해 듣기만 하는 부모님의 마음은 어떠할지 많은 걱정을 끼쳐드린 것 같아 죄송합니다. 무얼 하든 항상 하시는 말씀처럼 스스로 행복을 느끼며 살아갈 수 있도록 노력하는 아들이 되겠습니다. 그리고 어린 시절 저를 친자식처럼 길러주신 큰부모님, 저는 남들 보다 챙겨야 할 분이 두 배로 계시기에 두 배로 더 성공하고자 합니다. 다들 항상 건강하셨으면 좋겠습니다.

제가 부족한 탓에 미처 떠올리지 못한 분들에게도, 짧은 순간 스쳐 지나갔지만 많은 것들을 받았던 인연들에게도, 감사의 마음이 닿길 바라며...

눈이 소복하게 쌓인 관악의 열 번째 겨울 속에서,

2021년 2월 5일

이 한 결